Mass spectrometric investigations of intermediates from organic reactions using electrospray ionization

Dissertation

Johann Alexander Willms

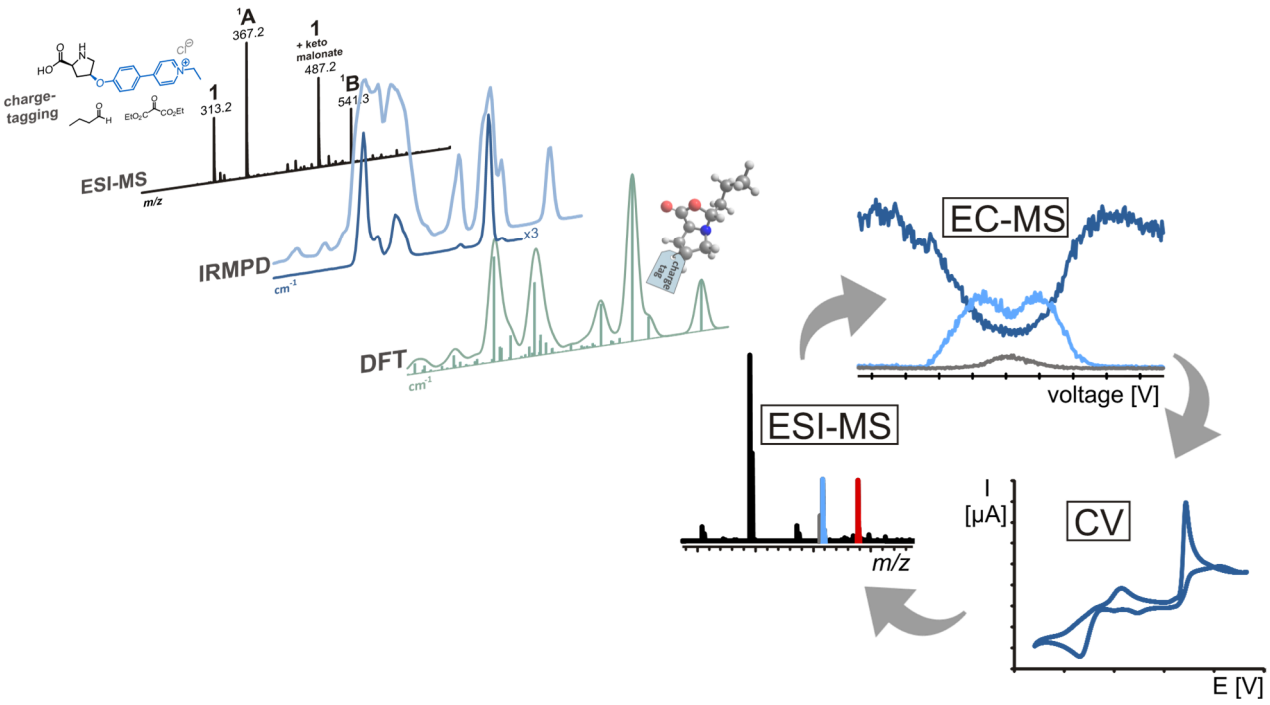

- Bonn 2019 -

Mass spectrometric investigations of intermediates from organic reactions using electrospray ionization

Dissertation

zur Erlangung des Doktorgrades (Dr. rer. nat.) der
Mathematisch-Naturwissenschaftlichen Fakultät
der Rheinischen Friedrich-Wilhelms-Universität Bonn

vorgelegt von

Johann Alexander Willms

aus Köln

- Bonn 2019 -

Angefertigt mit Genehmigung der Mathematisch-Naturwissenschaftlichen Fakultät der Rheinischen Friedrich-Wilhelms-Universität Bonn

1. Gutachter:	PD Dr. Marianne Engeser
2. Gutachter:	Prof. Dr. Arne Lützen
Tag der Promotion:	23.05.2019
Erscheinungsjahr:	2019

Publications

Major parts of this thesis have already been published in international, peer-reviewed journals:

[1] J. A. Willms, R. Beel, M. L. Schmidt, C. Mundt, M. Engeser, "A new charge-tagged proline-based organocatalyst for mechanistic studies using electrospray mass spectrometry", *Beilstein J. Org. Chem.* **2014**, *10,* 2027–2037. DOI: 10.3762/bjoc.10.211.

[2] J. A. Willms, J. Vidic, J. Barthelmes, V. Steinmetz, T. Bredow, P. Maître, M. Engeser, "Probing the gas-phase structure of charge-tagged intermediates of a proline catalyzed aldol reaction – Vibrational spectroscopy distinguishes oxazolidinone from enamine species", *Phys. Chem. Chem. Phys.* **2019**. DOI: 10.1039/c8cp04905j.

[3] J. A. Willms, H. Gleich, M. Schrempp, D. Menche, M. Engeser, "Investigations of the copper-catalyzed oxidative cross-coupling of tetrahydroisoquinolines with diethylzinc by a combination of mass spectrometric and electrochemical methods", *Chem. Eur. J.* **2018**, *24*, 2663–2668. DOI: 10.1002/chem.201704914.

Further publication:

[4] A. Schnell, J. A. Willms, S. Nozinovic, M. Engeser, "Mechanistic studies of an L-proline-catalyzed pyridazine formation involving a Diels-Alder reaction with inverse electron demand", *Beilstein J. Org. Chem.* **2019,** *15,* 30–43. DOI: 10.3762/bjoc.15.3.

Conferences - Talks and Poster:

1. *SFB 624: International Symposium – Templates in Chemistry - Present and Future*, **2013**, Bonn, Germany, Poster: C. Mundt, M. L. Schmidt, J. A. Willms, R. Beel, M. Engeser, "Synthesis of charge-tagged proline-based organocatalysts for mass spectrometric mechanistic studies".

2. *20th IMSC – International Mass Spectrometry Conference*, **2014**, Geneva, Switzerland, Talk: J. A. Willms, "Using a charge-tagged proline-based organocatalyst for mass spectrometric mechanistic studies".

3. *SFB 813: Fall Treat – Graduate Talks on Chemistry @ Spin Centers*, **2015**, Trier, Germany, Talk: J. A. Willms, "Mass spectrometric mechanistic investigation of the copper catalyzed oxidative derivatization of THIQs".

4. *SFB 813: Assessment*, Bonn, **2016**, Poster: Y. Lorenz, C. Mundt, J. A. Willms, M. Engeser, "Open-shell species in the gas phase: Mechanistic insight in catalytic reactions and stepwise one-electron reductions".

5. *ORCHEM – 20th Lecture Conference*, **2016**, Weimar, Germany, Poster: J. A. Willms, C. Mundt, M. Schrempp, K. H. Schuppener, R. Beel, M. L. Schmidt, M. Engeser, "Using mass spectrometry for mechanistic studies on organic reactions".

6. *ESOC – 20th European Symposium on Organic Chemistry*, **2017**, Cologne, Germany, Poster 1: J. A. Willms, H. Gleich, M. Schrempp, D. Menche, M. Engeser, "Mechanistic insight in the copper catalyzed oxidative derivatization of tetrahydroisoquinolines", Poster 2: J. A. Willms, J. Vidic, T. Bredow, P. Maître, M. Engeser, "Characterizing intermediates of a proline-catalyzed aldol reaction with a charge-tagged catalyst and IRMPD mass spectrometry".

7. *SFB 813: International Symposium – Perspectives in Hypovalent Chemistry,* **2017**, Bonn, Germany, Poster 1: J. A. Willms, H. Gleich, M. Schrempp, D. Menche, M. Engeser, "Mechanistic insight in the copper catalyzed oxidative derivatization of tetrahydroisoquinolines", Poster 2: J. A. Willms, J. Vidic, T. Bredow, P. Maître, M. Engeser, "Characterizing intermediates of a proline-catalyzed aldol reaction with a charge-tagged catalyst and IRMPD mass spectrometry".

Zusammenfassung

Im Fokus dieser Arbeit liegen Strategien zur mechanistischen Untersuchung organischer Reaktionen mittels Elektrospray-Massenspektrometrie (ESI-MS). Die Ergebnisse zur massenspektrometrischen Erforschung einer organokatalytischen Aldolreaktion sowie einer oxidativen Kreuzkupplung von Tetrahydroisoquinolin-Derivaten (THIQs) werden präsentiert.

Ein L-Prolin-basierter, ladungsmarkierter Organokatalysator wurde erfolgreich synthetisiert. Die positive Ladung ist an einem 1-Ethyl-pyridinium-4-phenoxy-Substituenten lokalisiert, welcher an die 4-Position des Prolin-Gerüstes bindet. Diese Ladungsmarkierung erwirkt eine deutlich gesteigerte Empfindlichkeit gegenüber der ESI-MS, wodurch die Detektion sowohl des Katalysator-Moleküls selbst als auch aller Katalysator-basierten Spezies einer Reaktionslösung erleichtert werden kann. Mithilfe des markierten Organokatalysators gelang die massenspektrometrische Detektion zweier zuvor postulierter Reaktionsintermediate der direkten inversen Aldolreaktion zwischen Aldehyden und Diethylketomalonat. Ein Versuchsaufbau aus mehreren Mikroreaktoren und Spritzenpumpen ermöglichte die Untersuchung der reagierenden Lösung unmittelbar nach dem Mischen von Substraten und Katalysator. So konnte der zeitliche Verlauf der Reaktion detailliert und bereits ab einer Reaktionszeit von wenigen Sekunden verfolgt werden.

Da die massenspektrometrischen Untersuchungen der genannten Intermediate mittels kollisionsinduzierter Fragmentierung keine sicheren Rückschlüsse auf deren genaue chemische Struktur zulassen, wurden die Ionen in einer weiteren Studie mittels Infrarot-Multiphotonendissoziation (infrared multiple photon dissociation, IRMPD) charakterisiert und identifiziert. Die Intermediat-Ionen wurden am Freie-Elektronen-Laser CLIO (Centre Laser Infrarouge d'Orsay) in einem Ionenfallen-Massenspektrometer im Fokus der intensiven Laserstrahlung isoliert und aus deren wellenlängenabhängiger Fragmentierungseffizienz indirekte Infrarot-Spektren abgeleitet. Die Messungen wurden mit der Unterstützung und Expertise von P. Maître und V. Steinmetz durchgeführt. Zur Interpretation der IRMPD-Spektren wurden Dichtefunktional-theoretische Rechnungen der Schwingungsfrequenzen möglicher Intermediat-Strukturen herangezogen. Aufbauend auf im Zuge dieser Forschungsarbeit

durchgeführten Optimierungen und Sondierungen der Startstrukturen wurden ausführliche Berechnungen durch Zusammenarbeit mit J. Vidic und T. Bredow erhalten. Die Ergebnisse legen nahe, dass es sich bei den massenspektrometrisch isolierten, intermediären Spezies um Oxazolidinon-Derivate handelt.

Die mechanistische Untersuchung der $CuCl_2$-katalysierten oxidativen Kreuzkupplung von THIQs mit Diethylzink mittels ESI-MS ist ein weiteres Forschungsprojekt dieser Arbeit. Das zentrale, positiv geladene Iminium-Intermediat dieser Reaktion wurde sowohl nach Umsetzung mit $CuCl_2$ als auch nach elektrochemischer Oxidation nachgewiesen und mit $ZnEt_2$ zum Kupplungsprodukt umgesetzt. Dies spricht gegen eine Beteiligung jeglicher Kupferspezies während des Kupplungsschrittes. Darüber hinaus wurde eine kurzlebige, intermediäre Aminium-Radikal-Spezies detektiert. Für die elektrochemische Oxidation kam eine kommerzielle Reaktorzelle zum Einsatz, welche auch bei der Aufnahme von spannungsabhängigen Ionenintensitätskurven zur massenspektrometrischen (EC-MS) Untersuchung verschiedener THIQ-Substrate genutzt wurde. Neben den EC-MS-Messungen wurden außerdem Cyclovoltammogramme der einzelnen THIQ-Derivate aufgezeichnet. Die begrenzte Substratbreite der Reaktion konnte dadurch auf das unzureichende Oxidationspotential von $CuCl_2$ zurückgeführt werden. Die Experimente stellen ein gutes Beispiel für die Verknüpfung massenspektrometrischer und cyclovoltammetrischer Methoden mittels EC-MS als geeignete Alternative zu synthetischen Screening-Methoden dar.

Abstract

This thesis focuses on strategies for the mechanistic investigation of organic reactions using electrospray mass spectrometry (ESI-MS). The results of mass spectrometric studies on an organocatalytic aldol reaction as well as an oxidative cross-coupling of tetrahydroisoquinoline derivatives (THIQs) are presented.

An L-proline-based, charge-tagged organocatalyst was successfully synthesized. The positive charge is localized on a 1-ethyl-pyridinium-4-phenoxy substituent which binds to the 4-position of the proline scaffold. A significantly increased sensitivity towards ESI-MS is caused by this charge tag, facilitating the detection of both the catalyst molecule itself and any catalyst-derived species of a reacting solution. Using the labelled organocatalyst, the mass spectrometric detection of two previously postulated reaction intermediates of the direct inverse aldol reaction between aldehydes and diethyl ketomalonate was achieved. A setup consisting of several microreactors and syringe pumps enabled the investigation of the reacting solution immediately after mixing substrates and catalyst. This way, the temporal progression of the reaction could be tracked in detail starting from a reaction time of a few seconds.

Since the mass spectrometric investigation of the above-mentioned intermediates by collision-induced fragmentation does not provide reliable indications on their exact chemical structure, the ions were characterized and identified by infrared multiple photon dissociation (IRMPD) in a further study. The intermediate ions were isolated in an ion trap mass spectrometer in the focus of the intense free-electron laser CLIO (Centre Laser Infrarouge d'Orsay) and indirect infrared spectra were derived from their wavelength-dependent fragmentation efficiency. The measurements were performed with the support and expertise of P. Maître and V. Steinmetz. The IRMPD spectra were interpreted with the aid of density functional theory calculations of vibrational frequencies of possible intermediate structures. Based on optimizations and a preselection of input structures, that were carried out in the course of this thesis, detailed calculations were obtained in collaboration with J. Vidic and T. Bredow. The results suggest that the mass spectrometrically isolated intermediate species exhibit an oxazolidinone structure.

Another research project of this thesis is the mechanistic investigation of the $CuCl_2$-catalyzed oxidative cross-coupling of THIQs with diethylzinc by ESI-MS. A positively charged iminium species, the key intermediate of this reaction, was detected both after conversion with $CuCl_2$ and after electrochemical oxidation and subsequently converted to the coupling product by addition of $ZnEt_2$. These findings are not consistent with the involvement of any copper species during the coupling step. Furthermore, a short-lived intermediary aminium radical species was detected. A commercial reactor cell was used for the electrochemical oxidation and also for the acquisition of voltage-dependent ion intensity curves for mass spectrometric (EC-MS) investigation of various THIQ substrates. In addition to EC-MS measurements, cyclovoltammograms of the different THIQ derivatives were recorded. The limited substrate scope of the reaction could be attributed to the insufficient oxidation potential of $CuCl_2$. The experiments are a good example for the combination of mass spectrometric and cyclovoltammetric methods using EC-MS as a suitable alternative to synthetic screening methods.

Acknowledgements

I would like to thank all the people who supported and accompanied me during the work for this PhD thesis.

My special thanks go to PD Dr. Marianne Engeser for the admission to her research group, her constantly open door and the enthusiastic support she provided on these interesting research topics.

I also thank Prof. Dr. Arne Lützen for being the second referee and for his suggestions and tips on synthetic issues during the weekly group seminars.

I would like to thank Prof. Dr. Thomas Bredow and Prof. Dr. Dr. Jochen Sautermeister for their kind acceptance of being the third and fourth member of the commission.

Moreover, I am grateful to Philippe Maître and Vincent Steinmetz for all their professional support, an exciting stay in Orsay and long days of measurements at CLIO.
I thank Jandro Vidic and Tobit Esch for their helpful and competent support in the field of computer chemistry.

My thanks go to Hermann Gleich, Michael Schrempp and Tongtong Wang for a friendly and interesting cooperation on the functionalization of THIQs.

In particular I thank all members of the Engeser group for a pleasant working atmosphere, lots of fun, great workdays and conference nights and much more. Above all, I would like to mention Christian Mundt, Melanie Krause, Anne Schnell, Yvonne Lorenz, Stefanie Becker and Martin Schmidt.

I owe first analytical experiences in quality control, which opened work-related doors for me during and after the research for my PhD thesis, to Ulrike Kopp.

I thank my bachelor students Anne Schnell, Kim Schuppener and Janosch Barthelmes for their eager contributions to our collaborative research.

My gratitude also goes to the entire Lützen group as well as the Esser group for a great laboratory neighborhood, assistance and donations of chemicals. I am especially grateful to Christoph Klein for long conversations during various running sessions.

Furthermore, I thank the staff of the department of mass spectrometry for their technical support and the temporal coordination of their routine measurements with my MS experiments. For the measurement of numerous NMR samples, my thanks go to the staff of the NMR department.

For his professional and unique linguistic assistance I thank Dominik Blatt and for his smart IT support I thank Peter Schramm.

I thank my whole clique of long-standing fellow students Andreas Lülsdorf, Bettina Kröner, Pia Schmidt (to name but a few) for their support, restful distraction and great lunchtimes in the cafeteria.

For support, affection, forbearance and much more I thank my whole family and my lovely girlfriend Kim Neumeister.

Thank you!

Table of contents

PART I

Basic principles of the experimental methods

1 Fundamentals

1.1 Electrospray ionization mass spectrometry

Electrospray ionization (ESI) has become one of the most frequently employed ionization techniques in the field of mass spectrometry. This technology involves the application of high voltage to a liquid sample at ambient pressure, thereby producing charged droplets which can be channeled into the high vacuum of a mass spectrometer. The principle has been developed in the course of several years and it needed the work of numerous scientists before its enormous potential could be exploited.[5,6] The development was fundamentally encouraged by the research of *Dole*[7] and *Fenn*,[8–11] the latter was honored by a Nobel Prize in 2002.[12]

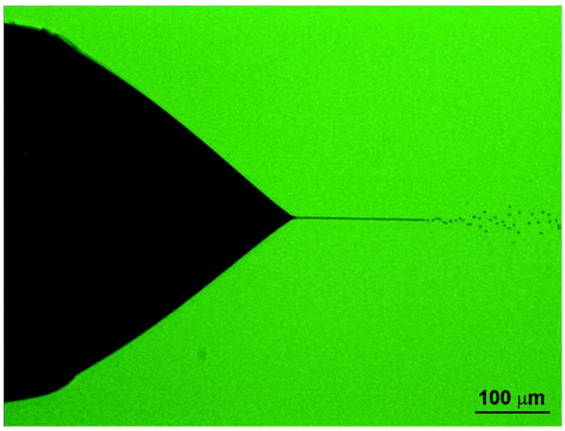

Figure 1.1 – Microphotograph of a typical meniscus shape and jet disintegration during the electrospray event in steady cone-jet mode for most sufficient ion production. (Reproduced in part from Ref [13] with permission. © 2007 American Chemical Society.)

ESI enables a direct transfer of analyte solutions into a mass spectrometer under comparatively soft conditions. It is suitable for the analysis of a variety of compound classes in an extremely broad range of molecular weight. Monoatomic ions, small polar molecules, soluble inorganic compounds and also polymers and proteins can be

analyzed *via* ESI-MS. Furthermore, either positively charged analytes or negative ions can be transferred into the gas phase, depending on the type of voltage applied.[5,6] Depending on the chemical structure of electrosprayed compounds, the ESI process often yields intact ions (e.g. M^+, M^{2+}, X^-, $[M–H]^-$) or ionic adducts (e.g. $[M+H]^+$, $[M+Na]^+$, $[M+Cl]^-$), which can be singly or multiply charged.

Since reacting solutions containing all components of a chemical reaction can be directly ionized, ESI is perfectly suited to support mass spectrometric investigations of reaction mechanisms.[14]

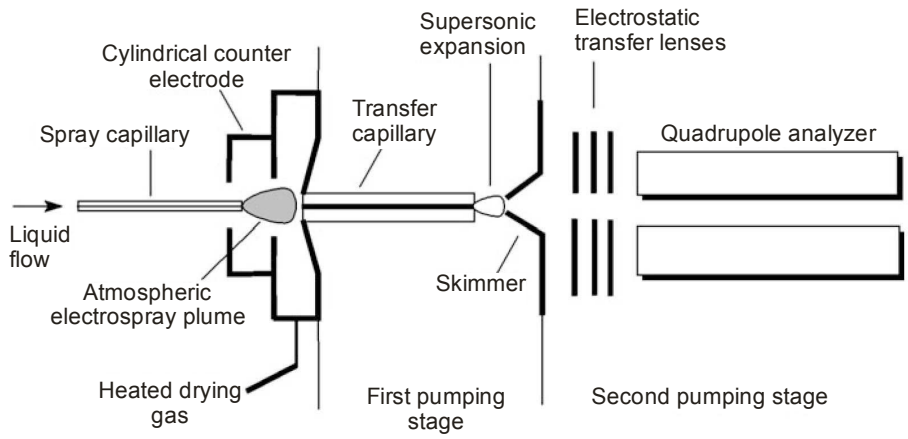

Figure 1.2 – Setup of an early ESI interface by *Fenn* et al.[11] (Reproduced from Ref [5] with permission. © Springer International Publishing AG 2017.)

A schematic setup of a typical ESI interface is shown in Figure 1.2. It consists of a thin conductive spray capillary and a cylindrical counter electrode. Under ambient pressure an electric field of 3 – 6 kV is applied between capillary and counter electrode. The analyte solution is passed through and gets exposed to the high voltage at the tip of the conductive capillary. The resulting electrospray is nebulized by one or more heated inert gas streams and a small part of the material reaches, driven by the electric field, the inlet of a transfer capillary. This capillary leads into the first pumping stage were the gas expands due to the reduced pressure. A small portion subsequently passes the nozzle of a cone-shaped electrode, the skimmer, and enters the high vacuum. Thereupon, the resulting ions are focused into the mass analyzing unit by multipoles and ion optics.[5,11,15] This continuous analyte flow from ambient pressure into high vacuum requires high-performance differential pumping.[5] Modern ESI interfaces often differ from this early setup but are still based on the same assembly.

The mechanism of ion formation during the ESI process can be summarized as follows: The application of high voltage to the infused analyte solution generates an electrically charged spray, whose droplets gradually decompose during a repeated disintegration of charged micro-droplets until completely desolvated ions are emitted. This course of events takes place within less than one millisecond.[5]

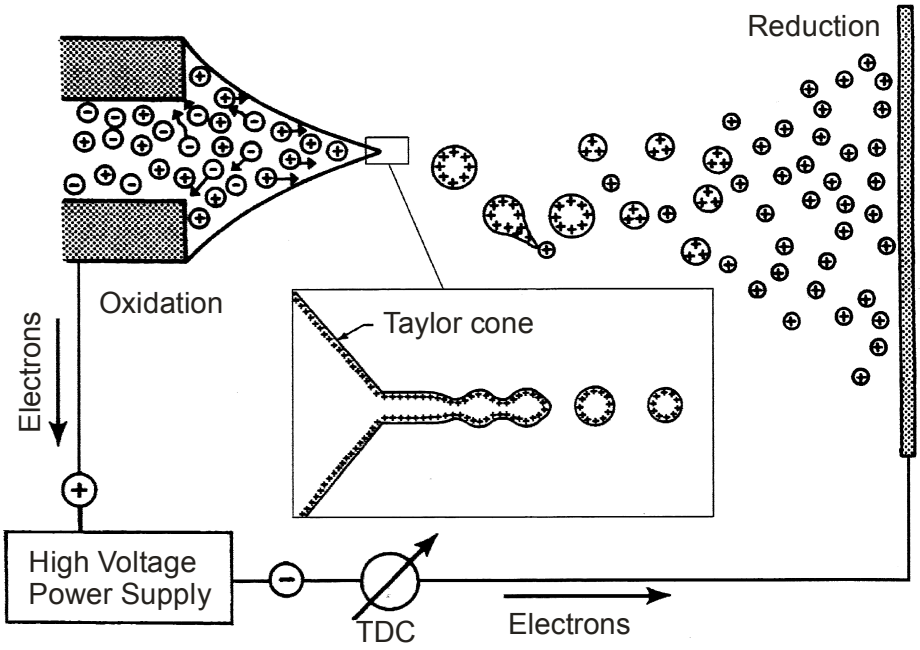

Figure 1.3 – Schematic of the ESI process; magnification of the formation of liquid droplets out of the Taylor cone is framed.[16] (Reproduced from Ref [5] with permission. © Springer International Publishing AG 2017.)

The phenomenon of releasing desolvated ions starts with the formation of a so called Taylor cone[17] at the end of the spray capillary (Figure 1.3). Even traces of an electrolyte in the leaking analyte solution cause sufficient conductivity resulting in a charge separation between surface and inner part of the meniscus due to the electric field. At a critical field strength, the meniscus changes into a cone shape. As the field strength increases, the surface tension is overcompensated by electrostatic forces, whereupon a fine beam of highly charged droplets is emitted in the direction of the counter electrode (Figure 1.1). Solvent molecules evaporate from these droplets, which is accelerated by above mentioned heated inert gas streams. As a result, the charge density at the droplet surface increases continuously until the so called Coulomb instability is reached, which is given by the Rayleigh equation:[6,18,19]

$$Q_{Ry} = 8\pi(\varepsilon_0 \gamma R^3)^{1/2}$$

Q_{Ry} is the excess charge on a droplet with a spherical radius R, surface tension γ and an electric permittivity ε_0. At $Q \geq Q_{Ry}$ tiny microdroplets, the offspring droplets, are released from the parent droplet. After this "uneven fission" the offspring droplets carry off about 1–2 % of the mass, but 10–18 % of the charge of their precursor drop.[20]

The mechanism of the final step, formation of isolated gas-phase ions out of these microdroplets, has been described by two different models. According to the "charged residue" model[7] complete desolvation of the ions takes place by successive loss of all solvent molecules from tiny droplets at the end of a fission cascade. The "ion evaporation" model[21] describes a direct evaporation of single ions from the microdroplet surface. Affirmations to both theories have been found. The charged residue process rather applies to large molecules and ion evaporation is more likely to occur when small molecules are involved.[22]

How effectively a given analyte can be transferred into the gas phase *via* ESI depends on numerous instrumental and chemical parameters.[23] A fundamental requirement is a stable electrospray, which is only produced if the formed Taylor cone keeps a continuous shape.[24] In this context, the applied capillary voltage and the flow rates of both analyte solution and nebulizing gas are decisive.[25] It is not surprising that the ESI response is also influenced by structural properties of the analyte itself and its concentration in the electrosprayed solution.[23] Neutral analytes need to react with ions by adduct formation or undergo electrochemical transformations into detectable species, while ionic substances are directly caught by the applied voltage. The surface activity of a substance is very decisive in this context. The higher the concentration of analyte molecules on the droplet surface, the higher is their concentration in the fissioning microdroplets and the more efficient is the release of individual ions.[23] For enhanced detection, functional groups that form ionic adducts more easily, can be incorporated in substances of interest.[26] Nonpolar residues increase the concentration on the droplet surface.[27] Another very effective strategy to increase the ESI response of a given analyte is charge-tagging. This method implies the introduction of charged substituents, charge tags, into the target compounds and has been successfully applied in the studies presented in Chapters 2 and 3.[28–31]

1.2 Infrared multiple photon dissociation spectroscopy of trapped ions

Trapped gaseous ions can be heated and forced to dissociate upon the absorption of multiple photons.[32] This infrared multiple photon dissociation (IRMPD) can be utilized to provide structural information on charged molecules by interpretation of their fragmentation mass spectra.[33–36]

While the low density of a trapped ion cloud impedes ordinary IR spectroscopy, IRMPD-MS can be used to derive vibrational spectra from the photon-induced fragmentation yield plotted against the respective photon energy. To this end, an intense laser beam is focused in the ion trap of a tandem mass spectrometer, e.g. a Fourier transform ion cyclotron resonance (FT-ICR)[37] or a quadrupole ion trap (QIT)[38] mass spectrometer. Commonly a highly intense and tunable laser beam from a free electron laser (FEL)[39–41] is used. During the experiment ions of interest are isolated by mass selection and stored in the ion trap of the mass spectrometer. The ion cloud is incrementally irradiated with light of a set laser wavelength while MS spectra are continuously recorded in order to follow the resulting, wavelength-dependent fragmentation. This procedure is carried out stepwise over wavelength values in the IR-range. Data processing is done by plotting the IRMPD efficiency, i.e. the fragmentation yield, against the respective laser wavelength (cf. Chapter 3).

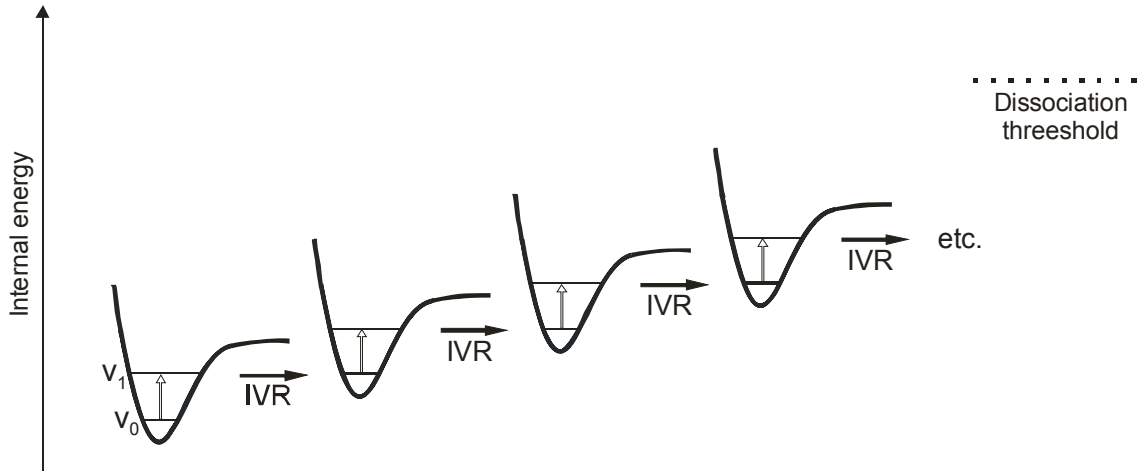

Figure 1.4 – Schematic representation of the IRMPD mechanism (Adopted from Ref. [36])

The non-coherent IRMPD process can be described as slow heating. Energy gets pumped into the polyatomic ion by intermolecular vibrational redistribution (IVR).[42] The successive absorption of numerous photons only occurs at infrared active vibrational modes of the ion. Statistical redistribution of the photon energy over all vibrational degrees of freedom leads to a relaxation of the resonant vibrational mode, which allows various consecutive excitations. This process repeats until the dissociation threshold is exceeded and fragmentation occurs.[33–36]

Usually experimental data is interpreted by careful comparison with computed IR spectra obtained by theoretical chemistry calculations. Computations at the density-functional theory (DFT) level are used in most cases and the best agreement of experimental and theoretical spectra is observed when lowest energy structures are considered.[34,35] Due to the harmonic approximation in most calculations of infrared absorption spectra, the resulting frequencies are generally blue-shifted compared to the experimental ones. Calculative inaccuracies can be mitigated by scaling the theoretical harmonic spectra with corrective factors.[43,44]

1.3 Electrochemistry/Mass spectrometry

The combination of electrochemical techniques with mass spectrometric analyses (EC-MS) is an excellent approach for the examination of redox processes.[45–47] It allows the investigation of transient species shortly after their electrochemical formation. The basic principle has been known for almost half a century and at least since the first reports[48,49] on the coupling of electrochemistry with ESI-MS the number and diversity of publications and instrumentations in that promising field have grown continually. The opportunity to combine the technique with liquid chromatography is an additional advantage. Hitherto, the research activities predominantly focus on the mimicry of potential drug metabolisms.[45–47]

The experimental setups used for EC-MS investigations of redoxactive species often consist of commercially available EC-flow-through cells containing a three electrode arrangement.[50] But also in-source electrochemical manipulation by functional electrospray emitters is an established strategy.[51] Figure 1.5 shows a schematic draw of an amphoteric thin-layer cell, a cell-type which was also used for the EC-MS study

presented in Chapter 4. The flow cell consists of a working electrode, an auxiliary electrode and a reference electrode.

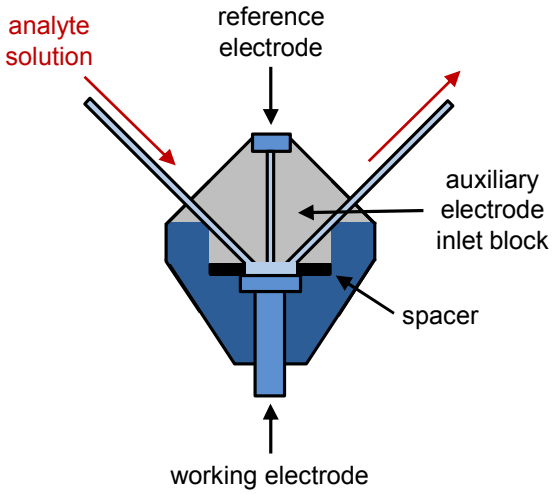

Figure 1.5 – Schematic drawing of an amphoteric thin-layer cell based on Ref. [50].

Voltage is applied between working and auxiliary electrode, also described as counter electrode, while analyte solutions are passed over the working electrode. Oxidative or reductive processes cause a current flow between the two electrodes. The reference electrode determines the cell potential for readjustment, since it is affected by the current flow and polarization effects.[46,50] For sufficient electrochemical conversion, this thin-layer cell arrangement requires comparatively low analyte flow rates in the range of ~500 µL/h, which is a detriment in some cases. However, the possibility of the implementation of different working electrode materials, such as platinum or glassy carbon, increases the range of applications.[50]

With electrochemical flow-through cells redox processes can be traced very descriptively by recording voltage dependent mass spectra, sometimes referred to as mass voltammograms.[52–54] The analyte solution is continuously passed through the EC cell while varying the applied voltage. Simultaneously a serious of mass spectra is recorded to follow changes in the signal intensities of the species of interest. The applied voltage is plotted against the detected ion intensity to feature the conversion as a function of the cell potential (cf. Figure 4.2 B)).

PART II

Detection and investigation of charge-tagged organocatalytic intermediates

Preamble of Part II

Organocatalysis can be defined as the acceleration of chemical reactions by the addition of substoichiometric amounts of metal-free, organic compounds.[55] Although the concept of using purely organic molecules for catalytic purposes had been known more than a century, its breakthrough occurred only two decades ago.[56] Since then, enantioselective organocatalytic reactions have become fully established in the field of asymmetric catalysis. In this respect, organocatalysis can now be regarded as a complementary field to metal- as well as enzyme-catalytic reaction types.[55,57] The range of reported stereoselective organocatalytic reactions has grown considerably and various organocatalysts have been designed in order to achieve higher selectivity and increased yields.[58] Concerning the reaction mechanisms, the diversity of organocatalytic reactions is based on different activation modes, such as enamine, iminium or SOMO activation.[56] L-proline could be referred to as the "organocatalyst of the first hour".[59–61] As the only natural amino acid with a secondary amine residue, this inexpensive compound exhibits a higher pK_a value as well as increased nucleophilicity compared to primary amino acids.[55] L-proline reacts more rapidly than other amines with carbonyl compounds to form iminium ions and enamines.[62]

In 2006, *Marquez* and *Metzger* presented their results on the ESI-MS analysis of proline-catalyzed aldol reactions using microreactors.[63] By investigating the reactions of acetone with different benzaldehydes they succeeded in detecting all intermediates of the still mostly accepted catalytic cycle for enamine catalysis.[64,65] Without any manipulation of their ESI response, some of these intermediary species were detected in excellent abundances. One weakness of a mere electrospraying of unmodified reactants from a given reaction can be the complexity of the resulting MS spectrum (cf. Figure 2.5 a)). Interpretation of the MS data may therefore require singling out specific mass-to-charge ratios (*m/z*) of postulated intermediates while unforeseen reaction paths are concealed by the chemical noise.

One research project of the group of PD Dr. Marianne Engeser is the circumvention of this problem by synthetically charge-tagging proline-based organocatalysts for ESI-MS studies.[4,66–70] The compounds all carry a 1-ethyl-pyridinium-4-phenoxy substituent,

which introduces a stabilized charge into the catalyst molecule. As a result, both the proline derivatives themselves as well as adducts and intermediates formed during a catalytic cycle exhibit an extremely increased ESI response factor.

In the diploma thesis preceding this doctoral thesis, first results have already been achieved in the course of an ESI-MS investigation of the inverse aldol reaction between different aldehydes and diethyl ketomalonate using a charge-tagged proline catalyst. Intermediary species of the reaction were detected in excellent intensities.[71] The subsequent research activities aimed to improve the synthetic route to the catalyst molecule and the synthesis of sufficient quantities thereof. Great efforts were also spent to conduct a gapless ESI-MS monitoring of the progress of the aldol reaction. The results are presented in Chapter 2.

Since collision induced fragmentation experiments did not provide a definite structural identification of the mentioned intermediates, the ions were examined in an IRMPD study. After data processing by determining the fragmentation efficiencies of every single IRMPD-MS spectrum, a thorough comparison with theoretical frequencies of DFT calculations of putative intermediate structures had to be carried out. The results are shown in Chapter 3.

2 A new charge-tagged proline-based organocatalyst for mechanistic studies using electrospray mass spectrometry

The results of this Chapter have been published in:
J. A. Willms, R. Beel, M. L. Schmidt, C. Mundt, M. Engeser, *Beilstein J. Org. Chem.* **2014**, *10,* 2027–2037.

Guest Editor: S. Höger

Own contributions to the manuscript

- Synthesis of all compounds, that were not commercially purchased
- Measurement, processing and interpretation of all MS experiments
- Writing of the manuscript

2.1 Abstract

A new 4-hydroxy-L-proline derivative with a charged 1-ethyl-pyridinium-4-phenoxy substituent has been synthesized with the aim of facilitating mechanistic studies of proline catalyzed reactions by Electrospray ionization (ESI) mass spectrometry. The charged residue ensures a strongly enhanced ESI response compared to neutral unmodified proline. The connection by a rigid linker fixes the position of the charge tag far away from the catalytic centre in order to avoid unwanted interactions. The use of a charged catalyst leads to significantly enhanced ESI signal abundances for every catalyst-derived species which are the ones of highest interest present in a reacting solution. The new charged proline catalyst has been tested in the direct asymmetric inverse aldol reaction between aldehydes and diethyl ketomalonate. Two intermediates in accordance with the List-Houk-mechanism for enamine catalysis have been detected and characterized by gas-phase fragmentation. In addition, their temporal evolution has been followed using a microreactor continuous-flow technique.

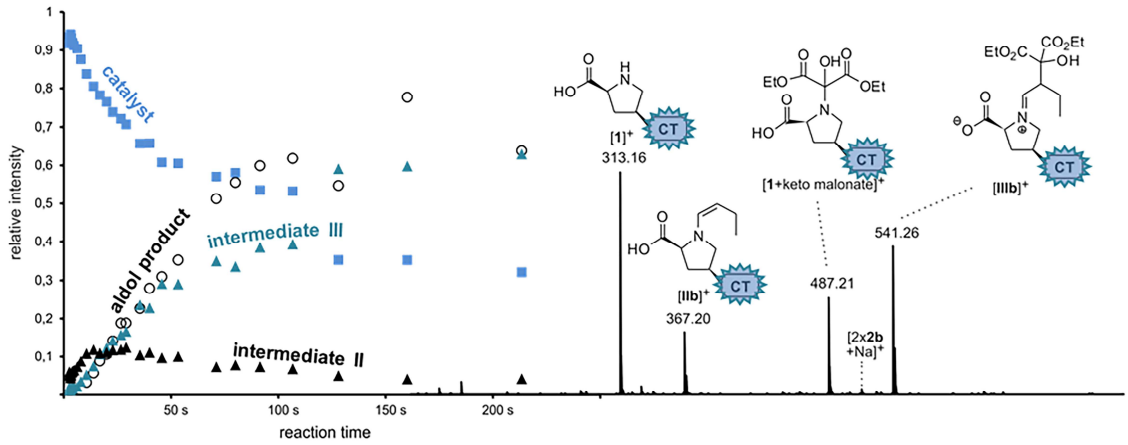

Figure 2.1 – Graphical Abstract of: J. A. Willms, R. Beel, M. L. Schmidt, C. Mundt, M. Engeser, *Beilstein J. Org. Chem.* **2014**, *10,* 2027–2037 (Ref. [1]).

2.2 Introduction

Electrospray ionization (ESI) mass spectrometry[72] has not only developed into a standard characterization method for an extremely broad variety of substances[6], but has also been recognized as a valuable tool for studying reaction mechanisms by transferring species of a reacting solution directly into the gas phase of a mass spectrometer[14,28,73–75]. The technique allows glimpses into the reacting solution as a function of time[29] and beyond that a characterization of transient intermediates by tandem mass-spectrometry. ESI mass-spectrometric mechanistic studies have been reported for a broad range of reaction types ranging from transition-metal catalyzed polymerization[73,30] and coupling reactions[29,76–83] to purely organic Diels-Alder reactions[84,85] to cite only a few representative examples.

However, the detection of transient reactive species is often hindered by their very low concentration. A reacting solution of a catalytic transformation typically contains quite a number of different species. Side products, off-cycle resting states, reagent degradation products and impurities of various origins may be present in much higher concentration than the interesting reactive intermediates. Thus, ESI spectra of reacting solutions can be frustratingly complicated and the transient species of interest might be superposed with a large number of more intense background signals.[63] In quantification using ESI, the detection limit has been lowered significantly by selected ion monitoring in MS/MS mode.[6] Similarly, transient reactive species have been successfully extracted from the chemical noise by collision induced dissociation (CID) MS/MS.[63] However, it is not possible to identify unknown or unexpected species by this strategy.

As a major drawback of ESI mass spectrometry in general, the signal intensity does not directly parallel the concentration, but the so called ESI response, i.e. the ionization probability during the ESI-process.[6,23] Hence it happens that the reaction intermediates of interest are concealed by easily ionizable other compounds present in the reacting solution. A convenient approach to solve this problem is the use of covalently attached charge-tags.[29–31,73,78,86] Charge-tagging the catalyst selectively enhances the signal abundances of all catalyst-derived species in a reacting solution and thus facilitates the identification of low-concentrated transient catalytic species. As a complementary

approach, charge-tagged substrates have been used to easily identify ("fish for") efficient catalysts.[73,30]

Since the year 2000, enantioselective catalysis based on small organic metal-free molecules has become an enormously growing research topic.[55,56,87–91] A large variety of organocatalyzed reactions with high efficiency and selectivity are nowadays known so that organocatalysis complements current catalytic fields such as organometallic or enzymatic catalysis as an independent subdomain.[55,87–91] Parallel to the enormous growth of organocatalytic applications in synthesis, mechanistic studies on organocatalytic reactions[64,65,92–97] using ESI mass spectrometry[63,98–108] have been reported. The pioneering studies of *List* and *Barbas*[61] revealed that the amino acid L-proline is an effective catalyst for a great variety of organic reactions, such as the direct asymmetric aldol reaction, one of the most important C-C bond-forming reactions in organic synthesis.[109] The currently accepted mechanism suggests a central enamine intermediate which forms a Zimmerman-Traxler-like transition state with the acceptor substrate.[64,65] The activity and enantioselectivity achieved by proline in many cases is thought to be due to a templating effect of the OH group directing the aldehyde in a preferred position *via* hydrogen bonding.[87,88] It is still controversial whether oxazolidinone formation plays a pivotal role in the catalytic cycle or just serves as an rate limiting parasitic off-cycle equilibrium.[92,94,96,110]

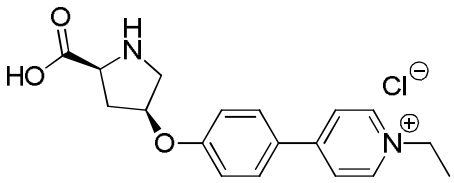

Figure 2.2 – The new charge-tagged proline-derived catalyst **1**.

Thus, we aimed to synthesize a charge-tagged L-proline-based organocatalyst for mechanistic studies by ESI-MS. Few proline derivatives carrying a covalently fixed charge have been reported by now.[102,111] They consist of an imidazolium salt attached to hydroxyproline *via* an ester group at the end of a flexible alkyl spacer. Interestingly, such charge tags can cause an enhancement of the catalytic performance through electrosteric activation,[111] but backfolding can also alter and disturb the catalytic process and induce the formation of side products.[102] In order to fix the charge far

away from the catalytic center and thus leave the original catalytic activity of L-proline preferably undisturbed, we chose a stiff 1-ethyl-pyridinium unit as charge-carrier separated from the catalytic center by a rigid phenyl linker (Figure 2.2).

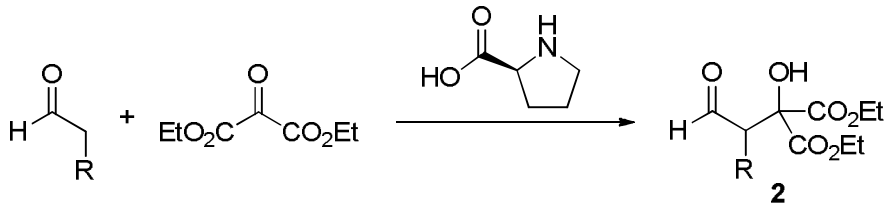

Scheme 2.1 – Inverse aldol reaction with aldehyde donors according to *Jørgensen*.[112] We studied the reaction for R = Ph (labelled **a** throughout this manuscript) and for R = Et (**b**).

We then tested the applicability of **1** for ESI-MS mechanistic studies on the first "inverse" crossed aldol reaction (Scheme 2.1) published in 2002 by *Jørgensen* and coworkers[112] in which the aldehyde acts as the donor in contrast to the "normal" crossed aldol mechanism. It represents an interesting version of a typical proline-catalyzed reaction for which to the best of our knowledge mechanistic studies have not been reported so far.

2.3 Results and discussion

2.3.1 Synthesis

Formation of the charge-carrying unit was accomplished starting from commercially available 4-bromophenol using a strategy reported by *Diemer* et al.[113] Protection of the hydroxy-group to yield **3**[114] was followed by Suzuki cross-coupling with commercial pyridine-4-boronic acid leading to **4**. Subsequent deprotection led to 4-(pyridine-4-yl)phenol **5** (Scheme 2.2).[113]

The preparation of the charge-tagged catalyst **1** starting from doubly-protected hydroxy-proline **6**[115] is depicted in Scheme 2.3.

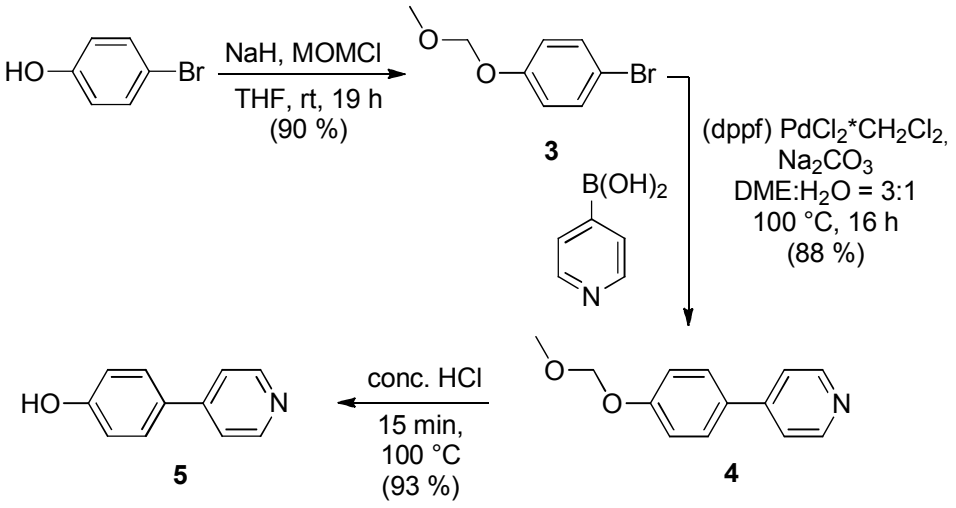

Scheme 2.2 – Synthesis of 4-(pyridin-4-yl)phenol **5.**

To introduce a suitable leaving group for the following step of the synthesis, **6** was mesylated to give the derivative **7**[116] for which crystals suitable for X-ray analysis have been obtained (Figure 2.3).

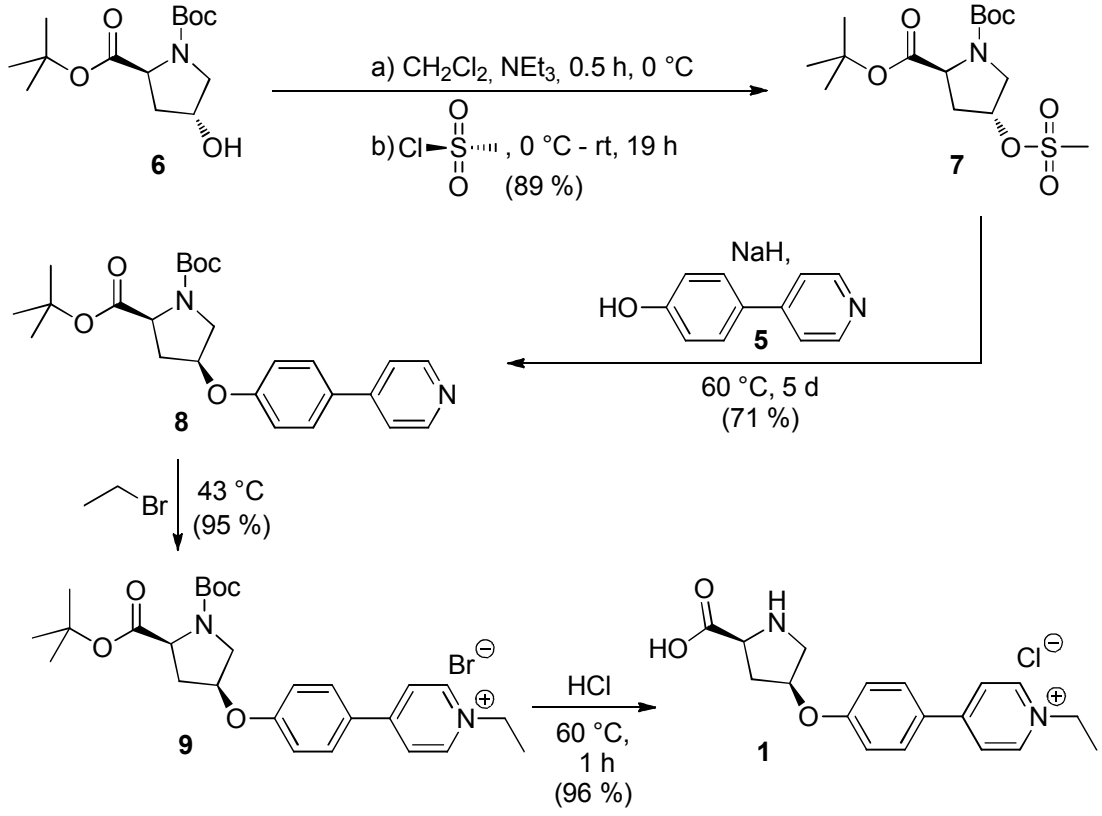

Scheme 2.3 – Synthesis of the charge-tagged proline catalyst **1**.

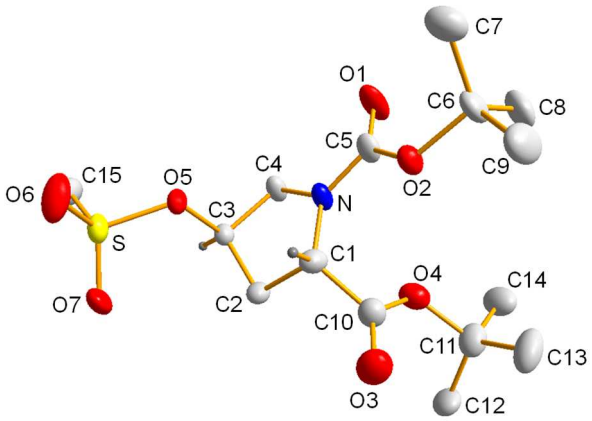

Figure 2.3 – Molecular structure of **7** in the solid state.

A S_N2 reaction with **5**[113] led to **8**. We abandoned our initial shorter synthetic route based on a Mitsunobu reaction leading from **6** directly to the *trans*-substituted diastereomer of **8** due to severe purification difficulties. **8** could be charge-tagged to **9** using ethyl bromide. Finally, the free catalyst **1** was obtained by acidic deprotection.[117]

2.3.2 Mechanism of the *Jørgensen* inversed aldol reaction

According to the mechanistic model for enamine catalysis from *List* and *Houk*,[64,65,97] the aldol reaction from *Jørgensen* should proceed *via* the catalytic cycle shown in Scheme 2.4.

We began our experiments with a test whether the charge tag does not disturb the catalysis. Indeed, **1** can achieve the formation of aldol products **2a** and **2b**, respectively, under the reaction conditions given in the literature.[112] Performed in simultaneous parallel reaction batches, **1** provides just about the same yields as unmodified proline and byproducts were not observed. Further, it is important to note that the substrates do not show any reaction when no catalyst, be it charge-tagged or not, is present in the solution.

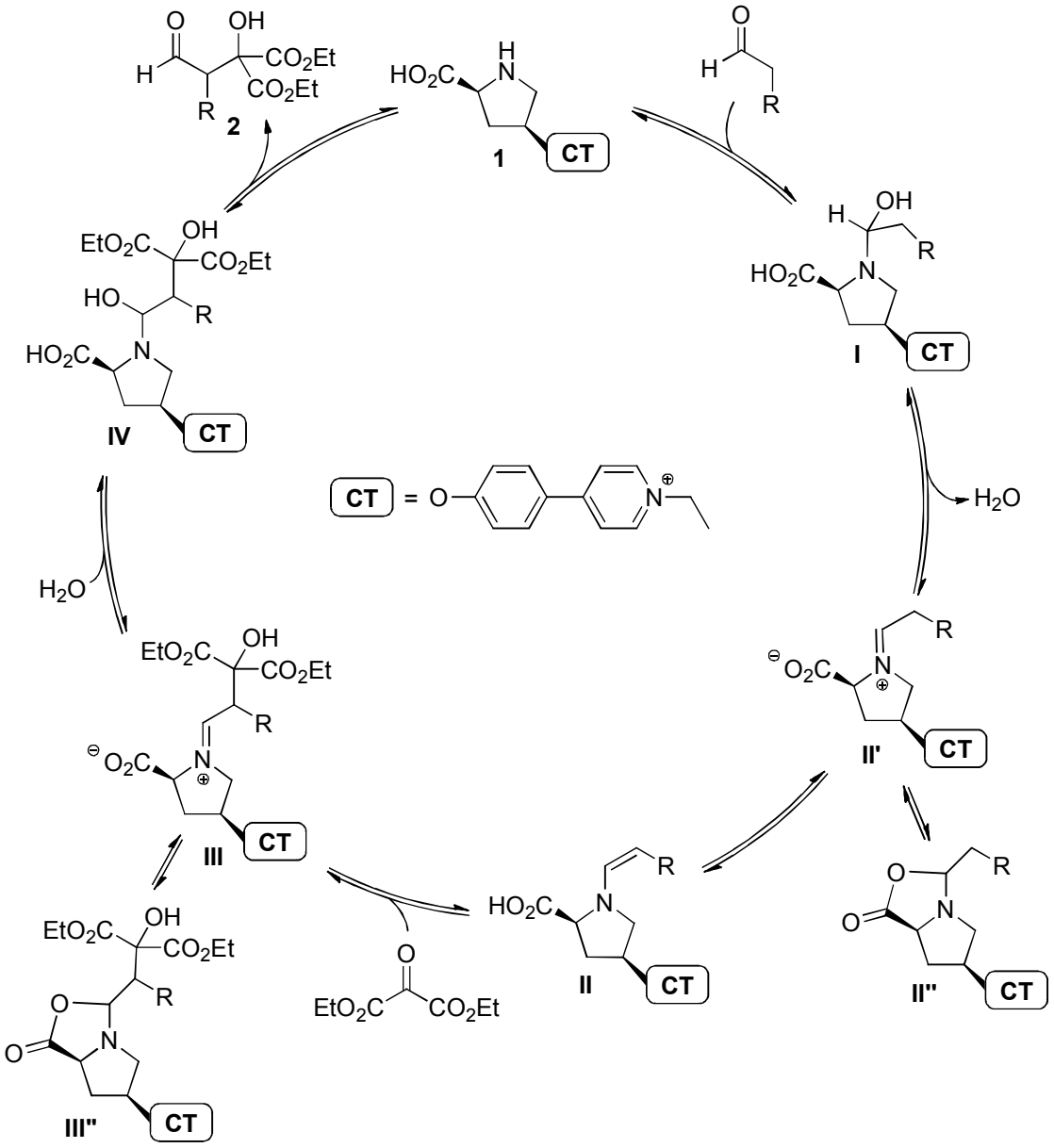

Scheme 2.4 – Proposed catalytic cycle[64,65] for the aldol reaction with aldehyde donors[112]; CT = charge tag, **a**: R = Ph, **b**: R = Et.

The easiest way of ESI reaction monitoring - mixing the reagents and measuring ESI spectra after various time intervals - is restricted to reaction times longer than approximately one minute and therefore not appropriate for fast conversions like aldol reactions. We thus decided to use a more complicated experimental setup of two mixing tees connected on-line to the mass spectrometer (Figure 2.4) to detect individual intermediates of both reactions by ESI-MS.

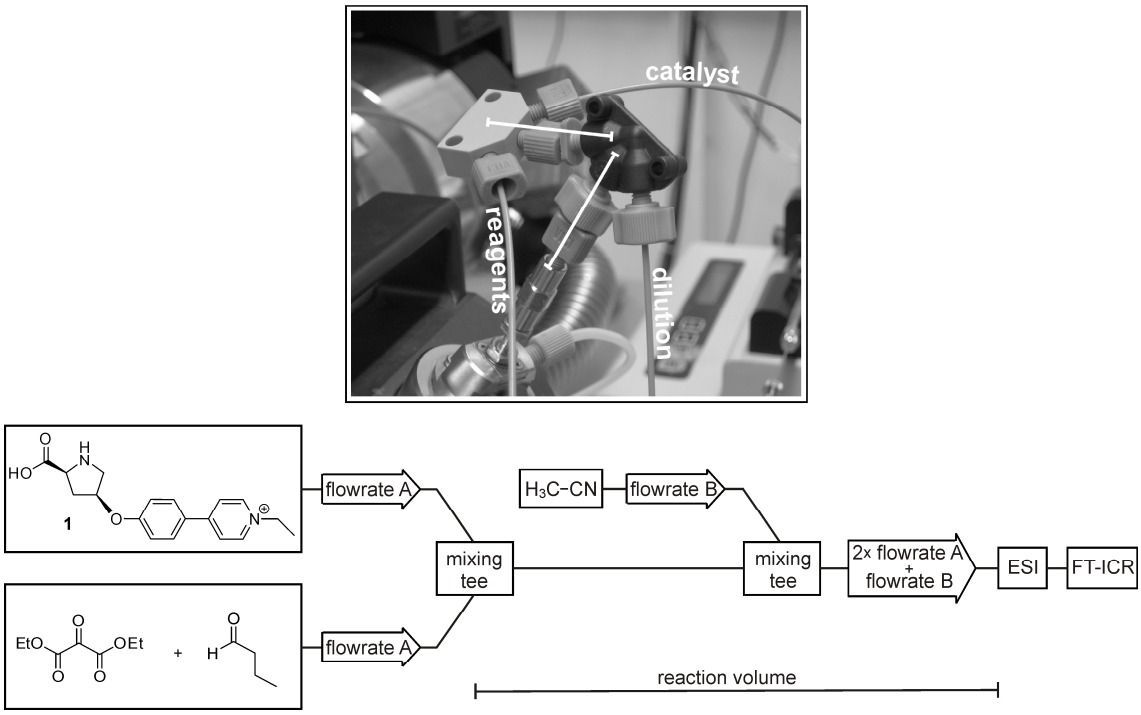

Figure 2.4 – Experimental setup for continuous-flow ESI-MS experiments using two mixing tee microreactors directly coupled to the ESI needle.

These so-called *continuous-flow* experiments[63,74] allow the sampling of reaction times down to seconds. Solutions of the reagents are mixed in the first microreactor and diluted to concentrations suitable for ESI-MS in the second microreactor. The reaction time between the mixing event and the electrospray is determined by the flow rates and capillary lengths. Mass spectra of a solution of diethyl ketomalonate, butyraldehyde and unmodified L-proline or **1**, respectively, are depicted in Figure 2.4.

The mass spectra shown in Figure 2.5 do not exhibit abundant signals for the reactants, even though these are present in the solution in excess to all other species, a fact that is due to the poor ESI response of ketoesters and even more so of aldehydes. In the case of the proline-catalyzed solution (Figure 2.5a), the catalyst is not visible either, because of an instrumental discrimination of low masses unfortunately unavoidable with our instrument. Instead, two expected intermediates of the catalytic cycle indeed are observed in reasonable abundances (Figure 2.5a): The signal at *m/z* 170.12 corresponds to $[\mathbf{IIb}_{untagged}+H]^+$ and the one at *m/z* 344.17 is assigned to $[\mathbf{IIIb}_{untagged}+H]^+$. In contrast, signals for the remaining two intermediates $\mathbf{Ib}_{untagged}$ and $\mathbf{IVb}_{untagged}$ have not been

found, which probably is due to their very low concentration in the reaction equilibria as well as to their facile fragmentation during ESI. Note that the group of *Metzger* has successfully achieved the detection of a similar intermediate for the aldol reaction between acetone and selected benzaldehydes using rather unusual and presumably extremely soft ESI conditions, and their results indeed confirm its facile fragmentation.[63]

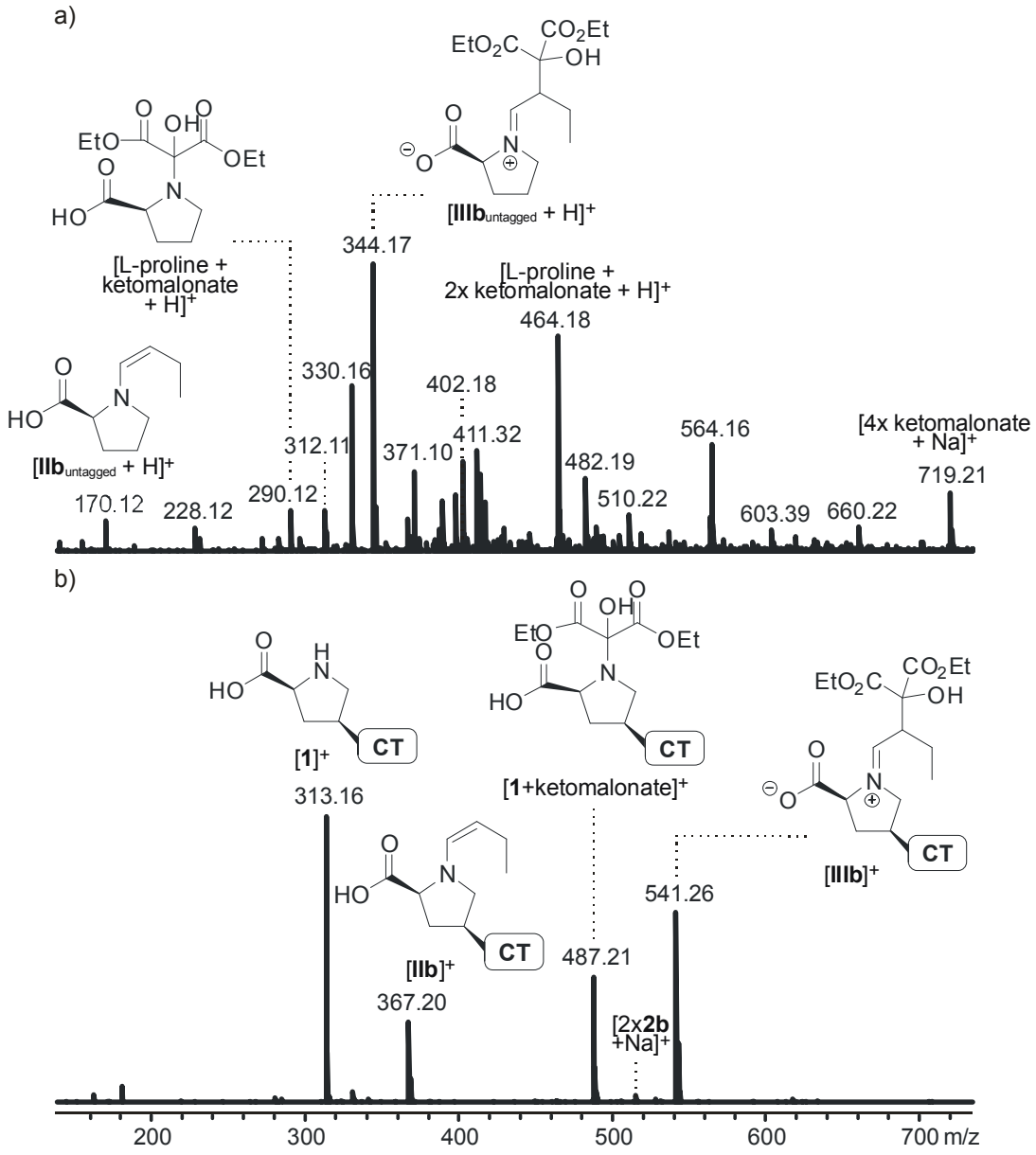

Figure 2.5 – ESI mass spectra of acetonitrile solutions of diethyl ketomalonate and butyraldehyde (a) with unmodified L-proline (b) or with the charge-tagged catalyst 1 recorded with the continuous-flow setup shown in Figure 2.4.

Interestingly, the signal at *m/z* 290.12 can be assigned to a further transient species of the reaction – it corresponds to a protonated adduct of proline with diethyl ketomalonate. This adduct might simply be a non-covalently bound aggregate, i.e. a typical ESI phenomenon,[6] but with regard of the rather low concentrations used here and of the observation of the analogous species in the proton-free charge-tagged case (see below), we prefer its assignment to a hemiaminal species formed in analogy to intermediate **I** by interaction of the proline nitrogen with the keto group of the ketomalonate (structure depicted in Figure 2.5a). In this special case, elimination of water is not possible due to the lack of adjacent hydrogen atoms. Its formation thus represents an off-cycle equilibrium dead-end in the course of the intended inverse aldol reaction.

In light of the relatively high abundances observed for the reaction intermediates catalyzed by uncharged L-proline, the implementation of a charge tag might have been considered unneccessary. However, the effect of using the charge-tagged catalyst **1** is impressive (Figure 2.5b). The obvious reduction of spectral complexity and chemical noise due to the strongly enhanced ESI response of **1** and all its derivatives underlines the great benefits of the charge-tagging strategy. In addition to the catalyst **1** at *m/z* 313.16, the three transient species discussed above are found almost exclusively and in very high abundances, i.e. the enamine [**IIb**]$^+$ at *m/z* 367.20, the iminium [**IIIb**]$^+$ at *m/z* 541.26 and the side-product [**1**+ketomalonate]$^+$ at *m/z* 487.21. Please note that the abundance of the latter varies significantly between different reaction runs, in contrast to the signals of the other intermediates whose appearances are highly reproducible. Very similar findings are observed when phenylacetaldehyde instead of butyraldehyde is used. In particular, intermediates [**IIa**]$^+$ and [**IIIa**]$^+$ have been detected in high abundances. Again, we unfortunately have not been successful in finding suitable electrospray conditions to detect the fragile intermediates [**Ia**]$^+$/[**Ib**]$^+$ and [**IVa**]$^+$/[**IVb**]$^+$. More importantly however, additional species that are not present in the unlabelled reference system have not been observed. There are no indications for an interference of the charge tag with the catalysis, in contrast to the findings with the flexible imidazolium-labelled proline derivatives reported previously.[102]

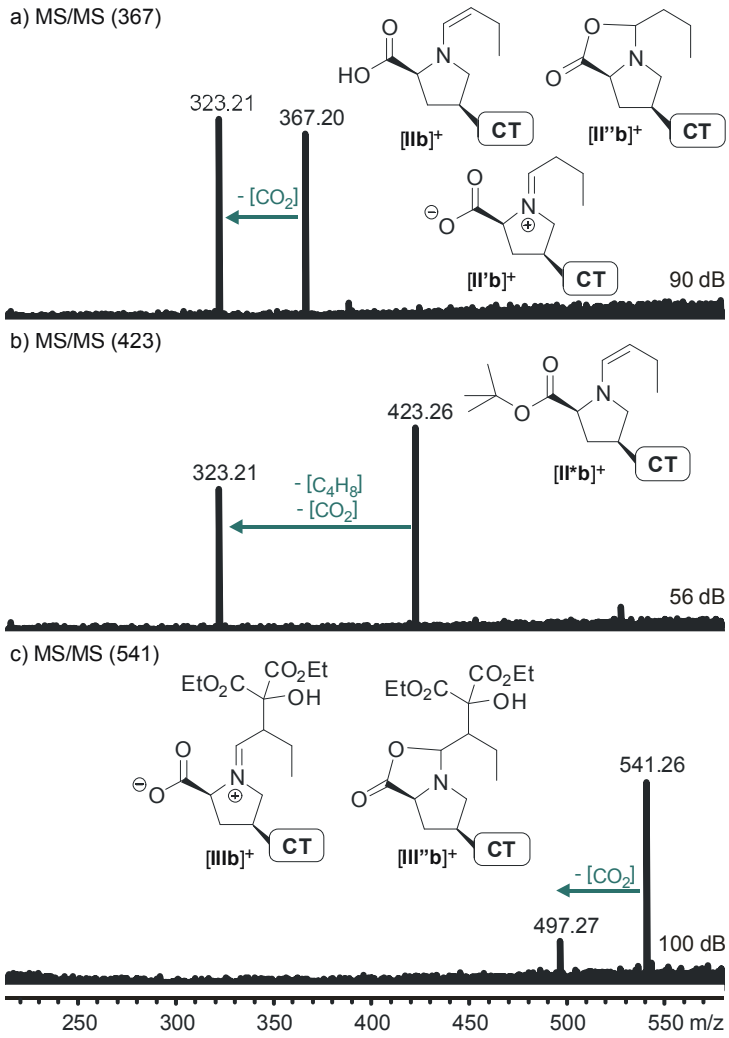

Figure 2.6 – ESI(+) CID MS/MS spectra of mass-selected intermediates a) [**IIb**]$^+$, b) the butyl ester derivative [**II*b**]$^+$, c) [**IIIb**]$^+$.

The mere detection of ions at *m/z* 415.20 (R = Ph) and 367.20 (R = Et), respectively, is not a proof for the presence of reactive enamines [**IIa**]$^+$/[**IIb**]$^+$ since the isomeric zwitterionic iminiums [**II'a**]$^+$/[**II'b**]$^+$ and oxazolidinones [**II''a**]$^+$/[**II''b**]$^+$ (Scheme 2.4) have the same elemental composition. Using one of the most important mass spectrometric means for structure elucidation, collision induced dissociation (CID) experiments have been performed. The results for R = Et are shown in Figure 2.6.

All four mass-selected ions [**IIa**]$^+$/[**IIb**]$^+$ and [**IIIa**]$^+$/[**IIIb**]$^+$ show a very strong propensity to expel CO_2 which even happens during the ESI process *via* in-source fragmentation when slightly harsher ionization conditions are used. This fragmentation is in perfect accordance with the zwitterionic iminium structures **II'** and **III** and can

also be rationalized for the oxazolidinone alternative **II''**, whereas it requires an additional hydrogen shift from the enamine structure **II**. On the other hand, the comparison with the fragmentation of the structurally related ion $[\mathbf{II^*b}]^+$ (Figure 2.6b)) is instructive. It doubtlessly possesses an enamine structure since it can neither form a zwitterionic iminium ion nor undergo lactonization to oxazolidinone **II''b** because of its *tert*-butyl blocked carboxylic acid function. The fragmentation of $[\mathbf{II^*b}]^+$ exclusively consists of a loss of $[C_5,H_8,O]$ which should correspond to a concerted or very fast stepwise elimination of *iso*-butene and CO_2 leading to the same product ion at *m/z* 323.21 than the expulsion of CO_2 from *m/z* 367.20. Interpreting the *iso*-butene loss as a closed-shell McLafferty-type rearrangement leads to the postulation of a (very short-lived undetected) intermediate enamine $[\mathbf{IIb}]^+$ which then obviously is able to undergo a facile CO_2 elimination. Thus, the fragmentation spectra unfortunately do not allow a clear discrimination of the three possible structures **II**, **II'**, and **II''**.

Marquez and *Metzger* mass-selected a signal corresponding to the protonated enamine from acetone and untagged L-proline and observed the elimination of CH_2O_2 (formic acid) instead of CO_2 as main fragmentation during CID.[63] The protonation during the ESI process presumably occurs at the nitrogen atom which enables a direct 1,2-elimination of formic acid. In our case, the respective charge-tagged species are detected in their original form without additional proton which explains the differing fragmentation route.

To monitor the temporal evolution of intermediates during the aldol reaction with the continuous-flow setup, series of ESI spectra at different reaction time stages have been recorded by varying the flow rate of the analyte solutions or by changing the length of the capillary connecting both mixing tees. A resulting graph of the normalized relative intensities vs. calculated reaction time is provided in Figure 2.7.

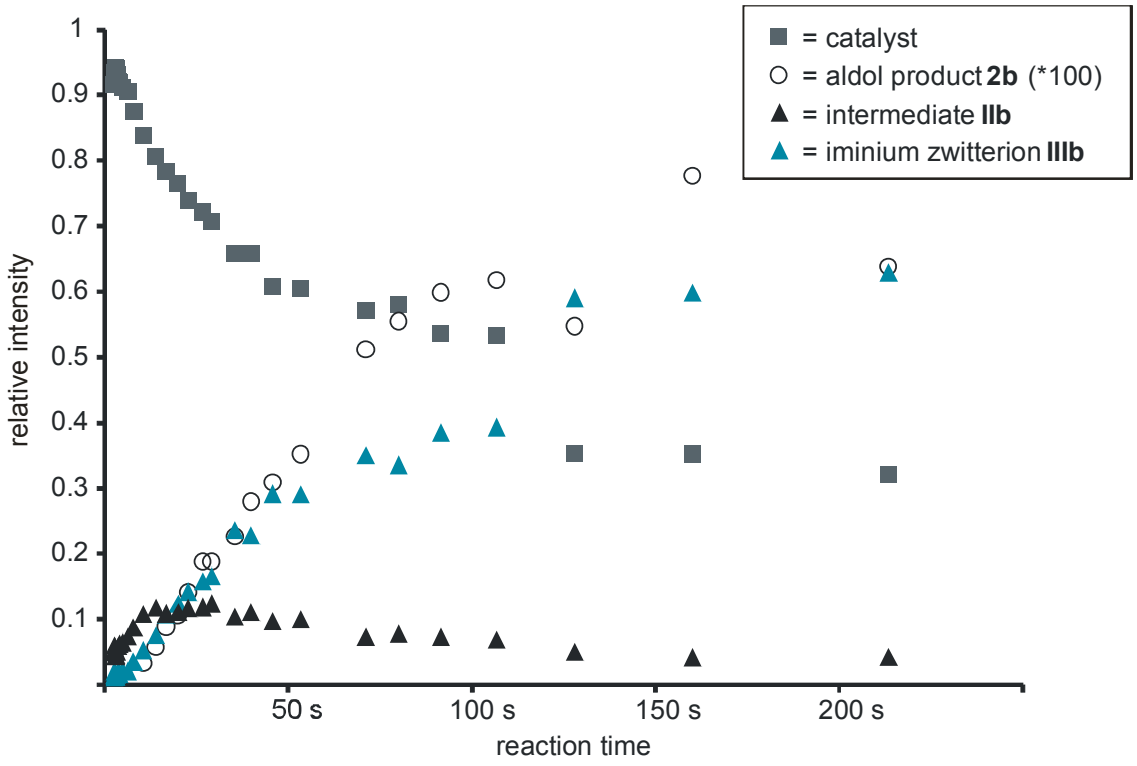

Figure 2.7 – Normalized relative intensities of ESI spectra recorded for the inverse aldol reaction of butyraldehyde, diethyl ketomalonate and charge-tagged catalyst **1** at different time stages using the continuous-flow setup with two microreactors shown in Figure 2.4.

The graph displays a rise of the concentration of **IIb** during the first seconds of the reaction accompanied by a decrease of **1**. Subsequently, an increase of **IIIb** occurs indicating that **IIIb** is formed out of **IIb** which is consistent with the mechanism in Scheme 4. The gradual increase of the final aldol product **2b** is visible as well; an enlargement of a factor of 100 has been used in the presentation of Figure 2.7 due to its much lower ESI response. Overall, these experiments reflect a very reasonable qualitative picture of the reaction behaviour and show that the use of catalyst **1** is suitable for the examination of L-proline catalyzed reactions *via* ESI-MS. However, we refrain from a quantitative kinetic modeling of the data to extract rate constants[29] because we encountered certain limitations of the method. Most importantly, we could not obtain an exact reproducibility of reaction times, probably because of quasi-unavoidable variations in the actual (dead) volumes of the setup *inter alia* due to varying minor capillary blockings. Moreover, we face a slight increase of signal abundances with measuring time (not reaction time) because analytes gradually accumulate in the system the longer their solutions are passed through. The extent of

this effect depends on the height of the flow rate which necessarily has to be changed when observing a reaction process with the continuous-flow method. Nevertheless, we would like to emphasize that the quality of the experiments surely suffices to depict the "chronological trend" of the reaction process.

2.4 Conclusion

We present the synthesis of the charge-tagged L-proline derived catalyst **1** in which a rigid phenylpyridine linker fixes the charge tag far away from the catalytically active centre in order to avoid unwanted interactions. In a comparative continuous-flow electrospray mass spectrometric study, the new charged catalyst **1** and neutral L-proline have been used to investigate the proline-catalyzed inverse crossed aldol reaction of aldehydes with diethyl ketomalonate. Two key intermediates of the List-Houk mechanism for enamine catalysis in addition to a transient off-cycle species could be observed experimentally. The use of **1** further allows facile access to a qualitative picture of the temporal evolution of catalyst-containing intermediates. We plan to use the new proline catalyst with a non-interfering charge-label presented here as a tool to study the templating role of the hydroxyl group in L-proline-catalyzed reactions in the gas-phase in the near future.

2.5 Experimental

2.5.1 Synthesis

Reactions under inert gas atmosphere were performed under argon using standard Schlenk techniques and oven-dried glassware prior to use. Thin layer chromatography was performed on aluminum TLC plates silica gel 60 F_{254} from Merck. Detection was carried out under UV light (254 and 366 nm). Products were purified by column chromatography on silica gel 60 (40 – 63 μm) from Merck. The ^{1}H and ^{13}C NMR spectra were recorded on a Bruker Avance 300 spectrometer, at 300.1 and 75.5 MHz, or a Bruker AM 400, at 400.1 MHz and 100.6 MHz, at 293 K respectively. The ^{1}H NMR

chemical shifts are reported on the δ scale (ppm) relative to residual non-deuterated solvent as the internal standard. The ^{13}C NMR chemical shifts are reported on the δ scale (ppm) relative to deuterated solvent as the internal standard. Signals were assigned on the basis of ^{1}H, ^{13}C, HMQC, and HMBC NMR experiments. Most solvents were dried, distilled, and stored under argon according to standard procedures. 4-Bromophenol, 4-pyridinylboronic acid, *trans*-*N*-(*tert*-butoxycarbonyl)-4-hydroxy-L-proline, L-proline, diethyl ketomalonate, phenylacetaldehyde and butyraldehyde were used as received from commercial sources.

4-Bromophenol methoxy methyl ether (3):[114] *p*-Bromophenol (3.00 g, 17.2 mmol) was dried under reduced pressure and dissolved in dry THF (160 mL) under inert gas atmosphere. NaH (1.32 g, 52.0 mmol) was added and the mixture was stirred at r.t. for 0.5 h. Methoxy methoxy chloride (2.08 mL, 26.0 mmol) was added dropwise and the resulting suspension was stirred for 19 h. The reaction was quenched by addition of a MeOH/H_2O mixture (1:1, 150 mL) and the aqueous phase was extracted with CH_2Cl_2 (4x 50 mL). The combined organic extracts were dried with $MgSO_4$ and the solvents were removed *in vacuo*. The crude product was purified by column chromatography on silica gel using cyclohexane/ethyl acetate (10:1) as eluent (R_f = 0.61). Compound **3** was obtained as colorless oil (3.38 g, 90 %). The spectroscopic data confirm the reported ones.[114]

4-[4-(Methoxymethoxy)phenyl]pyridine (4):[113] 4-Bromophenol methoxy methyl ether **3** (1.5 g, 6.9 mmol), 4-pyridinylboronic acid (1.02 g, 7.5 mmol), [1,1'-bis(diphenylphosphino)ferrocene]-palladium(II)dichloride dichloromethane complex (0.22 g, 0.28 mmol) and Na_2CO_3 (8.78 g, 82.4 mmol) were suspended in a H_2O/1,2-dimethoxyethane mixture (1:3, 75 mL), heated to 100 °C und stirred for 16 h. The resulting mixture was filtered and the filtrate was mixed with H_2O (75 mL) and CH_2Cl_2 (75 mL) for phase separation. The aqueous phase was extracted with CH_2Cl_2 (2x 75 mL), the combined organic extracts were dried with $MgSO_4$ and the solvents were removed *in vacuo*. The crude product was purified by column chromatography on silica gel using ethyl acetate with 5 % triethylamine as eluent (R_f = 0.50). Compound **4** was obtained as white solid (1.31 g, 88 %). The spectroscopic data confirm the reported ones.[113]

4-(Pyridine-4'-yl)phenol (5)[113] and **(2*S*,4*R*)-*tert*-Butyl-*N*-*tert*-butyloxycarbonyl-4-hydroxyprolinate (6)**[115] were prepared according to literature protocols.

(2S,4R)-*tert*-Butyl-*N*-*tert*-butoxycarbonyl-4-oxymethanesulfonylprolinate (7) was prepared according to a known procedure[116] which was slightly modified: (2*S*, 4*R*)-*tert*-butyl-*N*-*tert*-butyloxycarbonyl-4-hydroxyprolinate **6** (3.14 g, 10.9 mmol) was dissolved in CH_2Cl_2 (55 mL) and cooled to 0 °C. Triethylamine (3.01 mL, 21.5 mmol) was added and the mixture was stirred for 0.5 h. Methanesulfonyl chloride (1.33 mL, 17.1 mmol) was added dropwise over 10 min and the resulting solution was stirred overnight without further cooling. The reaction was quenched by addition of a saturated solution of $NaHCO_3$ (70 mL) and the aqueous phase was extracted with CH_2Cl_2 (2x 50 mL). The combined organic extracts were dried with $MgSO_4$ and the solvents were removed *in vacuo*. The crude product was purified by column chromatography on silica gel using cyclohexane/ethyl acetate (2:3) as eluent ($R_f = 0.61$). Compound **7** was obtained as colorless solid (3.55 g, 89 %). Crystals suitable for X-ray analysis have been obtained by slow diffusion of cyclohexane into a Et_2O solution of **7**. ^{1}H-NMR (400 MHz, CD_3OD): δ 5.26 (s, 1H, $CH_2C\mathbf{H}CH_2$), 4.30-4.23 (m, 1H, $CH_2C\mathbf{H}N$), 3.83-3.76 (m, 1H, $NC\mathbf{H_2}CH$), 3.70-3.63 (m, 1H, $NC\mathbf{H_2}CH$), 3.14 (s, 3H, S-$C\mathbf{H_3}$), 2.67-2.56 (m, 1H, $CHC\mathbf{H_2}CH$), 2.28-2.19 (m, 1H, $CHC\mathbf{H_2}CH$), 1.50-1.44 (m, 18H, $C(C\mathbf{H_3})_3$) ppm; ^{1}H-NMR (400 MHz, CD_3OD, 333 K): δ 5.26 (s, 1H, $CH_2C\mathbf{H}CH_2$), 4.30-4.26 (m, 1H, $CH_2C\mathbf{H}N$), 3.83-3.74 (m, 1H, $NC\mathbf{H_2}CH$), 3.72-3.63 (m, 1H, $NC\mathbf{H_2}CH$), 3.12 (s, 3H, S-$C\mathbf{H_3}$), 2.67-2.54 (m, 1H, $CHC\mathbf{H_2}CH$), 2.30-2.20 (m, 1H, $CHC\mathbf{H_2}CH$), 1.48 (s, 9H, $C(C\mathbf{H_3})_3$), 1.46 (s, 9H, $C(C\mathbf{H_3})_3$) ppm; ^{13}C-NMR (100 MHz, CD_3OD): δ 173.0/172.9 (**C**=O), 155.6 (**C**=O), 83.1 ($\mathbf{C}(CH_3)_3$), 82.1/81.9 ($\mathbf{C}(CH_3)_3$), 80.6/79.9 ($CH_2\mathbf{C}HCH_2$), 59.5/59.4 ($CH_2C\mathbf{H}N$), 54.1/53.7 ($N\mathbf{C}H_2CH$), 38.3 (S-$\mathbf{C}H_3$), 37.3 ($CH\mathbf{C}H_2CH$), 28.6 ($C(\mathbf{C}H_3)_3$), 28.3/28.2 ($C(\mathbf{C}H_3)_3$) ppm; ^{13}C-NMR (125 MHz, CD_3OD, 333 K): δ 172.9 (**C**=O), 155.6 (**C**=O), 83.1 ($\mathbf{C}(CH_3)_3$), 82.1 ($\mathbf{C}(CH_3)_3$), 80.5/79.8 ($CH_2\mathbf{C}HCH_2$), 59.5 ($CH_2\mathbf{C}HN$), 53.9/53.5 ($N\mathbf{C}H_2CH$), 38.5 (S-$\mathbf{C}H_3$), 38.3/37.3 ($CH\mathbf{C}H_2CH$), 28.7 ($C(\mathbf{C}H_3)_3$), 28.3 ($C(\mathbf{C}H_3)_3$) ppm; HRMS-ESI (*m*/*z*): $[M+Na]^+$ calcd for $[C_{15}H_{27}NNaO_7S]^+$, 388.1406; found, 388.1398. The NMR data are consistent with the reported ones measured in $CDCl_3$.[116,118]

(2S,4S)-*tert*-Butyl-*N*-*tert*-butoxycarbonyl-4-(4-(pyridine-4-yl)phenoxy)prolinate (8): 4-(Pyridine-4'-yl)phenol **5** (0.63 g, 3.7 mmol) and NaH (0.14 g, 5.5 mmol) were dissolved in dry DMSO (100 mL) under inert gas atmosphere. The suspension was

heated to 60 °C and stirred for 1.5 h. (2*S*,4*R*)-*tert*-Butyl-*N*-*tert*-butoxycarbonyl-4-oxymethanesulfonylprolinate **7** (1.33 g, 3.7 mmol) was added and the mixture was stirred for 5 d at 60 °C. The reaction progress was controlled by thin layer chromatography. The reaction was quenched by addition of H_2O (100 mL) and the aqueous phase was extracted with CH_2Cl_2 (2x 80 mL) and with Et_2O (2x 80 mL). The combined organic extracts were dried with Na_2SO_4 and the solvents were removed *in vacuo*. Remaining DMSO was removed by distillation. The crude product was purified by column chromatography on silica gel using cyclohexane/ethyl acetate (1:3) with 5 % triethylamine as eluent (R_f = 0.50). Compound **8** was obtained as colorless solid (1.14 g, 71 %). ^{1}H-NMR (300 MHz, CD_3OD): δ 8.55-8.45 (m, 2H, $\mathbf{H}_{o\text{-}py}$), 7.72 (d, 2H, $\mathbf{H}_{m\text{-}ph}$, ^3J = 8.8 Hz), 7.67 (d, 2H, $\mathbf{H}_{m\text{-}py}$, ^3J = 6.1 Hz), 7.06/7.00 (d, 2H, $\mathbf{H}_{o\text{-}ph}$, ^3J = 8.8 Hz), 5.06 (s, 1H, $CH_2C\mathbf{H}CH_2$), 4.41-4.26 (m, 1H, $CH_2C\mathbf{H}N$), 3.86-3.72 (m, 1H, $NC\mathbf{H_2}CH$), 3.72-3.57 (m, 1H, $NC\mathbf{H_2}CH$), 2.67-2.49 (m, 1H, $CHC\mathbf{H_2}CH$), 2.47-2.37 (m, 1H, $CHC\mathbf{H_2}CH$), 1.51-1.40 (m, 18H, $C(C\mathbf{H_3})_3$) ppm; ^{13}C-NMR (75 MHz, CD_3OD): δ 172.5/172.5 (**C**=O), 159.7/159.5 (**C**=O), 156.0 ($\mathbf{C}_{ph}$–O), 150.4 ($\mathbf{C}_{o\text{-}py}$–H), 150.1 ($\mathbf{C}_{p\text{-}py}$–C), 131.7/131.4 ($\mathbf{C}_{p\text{-}ph}$–C), 129.6/129.4 ($\mathbf{C}_{m\text{-}ph}$–H), 122.5 ($\mathbf{C}_{m\text{-}py}$–H), 117.3/117.2/117.2 ($\mathbf{C}_{o\text{-}ph}$–H), 82.9/82.7/82.6 ($\mathbf{C}(CH_3)_3$), 81.9/81.6 ($\mathbf{C}(CH_3)_3$), 77.2/76.2 ($CH_2\mathbf{C}HCH_2$), 60.1/59.8 ($CH_2\mathbf{C}HN$), 53.6/53.2 ($N\mathbf{C}H_2CH$), 37.1/36.4 ($CH\mathbf{C}H_2CH$), 28.7/28.6 ($C(\mathbf{C}H_3)_3$), 28.4 ($C(\mathbf{C}H_3)_3$) ppm; HRMS-ESI (*m*/*z*): $[M+H]^+$ calcd for $[C_{25}H_{33}N_2O_5]^+$, 441.2389; found, 441.2390.

4-(4-((3*S*,5*S*)-1,5-Bis(*tert*-butoxycarbonyl)pyrrolidine-3-yloxy)phenyl)-1-ethyl-pyridiniumbromide (9): (2*S*,4*S*)-*tert*-Butyl-*N*-*tert*-butoxycarbonyl-4-(4-(pyridine-4-yl)phenoxy)prolinate **8** (0.22 g, 0.5 mmol) was dissolved in bromoethane (13.0 mL, 174.2 mmol), heated to 43 °C and stirred for 5 d. Bromoethane was removed *in vacuo*. Compound **9** was obtained as yellowish-brown solid (0.26 g, 95 %). ^{1}H-NMR (400 MHz, CD_3OD): δ 8.89 (d, 2H, $\mathbf{H}_{o\text{-}py}$, ^3J = 6.8 Hz), 8.35 (d, 2H, $\mathbf{H}_{m\text{-}py}$, ^3J = 6.8 Hz), 8.08/7.99 (m, 2H, $\mathbf{H}_{m\text{-}ph}$), 7.18/7.11 (d, 2H, $\mathbf{H}_{o\text{-}ph}$, ^3J = 8.9 Hz), 5.19-5.13 (m, 1H, $CH_2C\mathbf{H}CH_2$), 4.63 (q, 2H, $C\mathbf{H_2}CH_3$, ^3J = 7.4 Hz), 4.43-4.36 (m, 1H, $CH_2C\mathbf{H}N$), 3.89-3.73 (m, 1H, $NC\mathbf{H_2}CH$), 3.71-3.58 (m, 1H, $NC\mathbf{H_2}CH$), 2.71-2.55 (m, 1H, $CHC\mathbf{H_2}CH$), 2.47-2.40 (m, 1H, $CHC\mathbf{H_2}CH$), 1.67 (t, 3H, $CH_2C\mathbf{H_3}$, ^3J = 7.4 Hz), 1.52-1.42 (m, 18H, $C(C\mathbf{H_3})_3$) ppm; ^{13}C-NMR (100 MHz, CD_3OD): δ 172.5/172.4 (**C**=O), 162.0 ($\mathbf{C}_{ph}$–O), 157.0 ($\mathbf{C}_{p\text{-}py}$–C), 155.9 (**C**=O), 145.2 ($\mathbf{C}_{o\text{-}py}$–H), 131.2/131.1 ($\mathbf{C}_{m\text{-}ph}$-H), 127.5 ($\mathbf{C}_{p\text{-}ph}$-C), 125.0 ($\mathbf{C}_{m\text{-}py}$–H), 117.8/117.7 ($\mathbf{C}_{o\text{-}ph}$–H), 82.7/82.6 ($\mathbf{C}(CH_3)_3$), 81.6 ($\mathbf{C}(CH_3)_3$),

77.6/76.6 (CH_2**C**HCH_2), 60.0/59.8 (CH_2**C**HN), 57.2 (**C**H_2CH_3), 53.6/53.2 (N**C**H_2CH), 37.1/36.3 (CH**C**H_2CH), 28.7/28.6 (C(**C**$H_3)_3$), 28.3 (C(**C**$H_3)_3$), 16.7 (CH_2**C**H_3) ppm; HRMS-ESI (*m*/*z*): $[M]^+$ calcd for $[C_{27}H_{37}N_2O_5]^+$, 469.2697; found, 469.2692.

4-(4-((3*S*,5*S*)-5-Carboxypyrrolidin-3-yloxy)phenyl)-1-ethylpyridiniumbromid (1) was prepared analogous to a known procedure[117] and obtained as beige-brown solid (96 %). ^{1}H-NMR (400 MHz, CD_3OD): δ 8.92 (d, 2H, $H_{o\text{-}py}$, ^3J = 6.4 Hz), 8.37 (d, 2H, $H_{m\text{-}py}$, ^3J = 6.4 Hz), 8.06 (d, 2H, $H_{m\text{-}ph}$, ^3J = 8.6 Hz), 7.27/7.20 (d, 2H, $H_{o\text{-}ph}$, ^3J = 8.6 Hz), 5.42 (s, 1H, CH_2C**H**CH_2), 4.73-4.58 (m, 3H, C**H**$_2$$CH_3$ and CH_2C**H**N), 3.82-3.62 (m, 2H, NC**H**$_2$CH), 2.85-2.73 (m, 1H, CHC**H**$_2$CH), 2.71-2.63 (m, 1H, CHC**H**$_2$CH), 1.67 (t, 3H, CH_2C**H**$_3$, ^3J = 7.3 Hz) ppm; ^{13}C-NMR (100 MHz, CD_3OD): δ 171.0 (**C**=O), 160.9 ($\mathbf{C}_{ph}$–O), 156.9 ($\mathbf{C}_{p\text{-}py}$–C), 145.4 ($\mathbf{C}_{o\text{-}py}$–H), 131.0 ($\mathbf{C}_{m\text{-}ph}$-H), 128.5 ($\mathbf{C}_{p\text{-}ph}$-C), 125.2 ($\mathbf{C}_{m\text{-}py}$–H), 118.0 ($\mathbf{C}_{o\text{-}ph}$–H), 77.3/76.7 (CH_2**C**HCH_2), 59.8 (CH_2**C**HN), 57.4 (**C**H_2CH_3), 52.7 (N**C**H_2CH), 35.7 (CH**C**H_2CH), 16.7 (CH_2**C**H_3) ppm; HRMS-ESI (*m*/*z*): $[M]^+$ calcd for $[C_{18}H_{21}N_2O_3]^+$, 313.1547; found, 313.1563.

Diethyl 2-hydroxy-2-(2-oxo-1-phenylethyl)malonate (2a) was prepared according to the reported procedure[112] and obtained as orange oil. The synthesis was carried out twice, once using L-proline (82 %), once using **1** as catalyst (79 %).

Diethyl 2-hydroxy-2-(1-oxobutan-2-yl)malonate (2b) was prepared according to the reported procedure[112] and obtained as orange oil (using L-proline: 83 %, using **1:** 80 %).

Crystal structure determination: X-ray crystallographic analysis of **7** was performed on a Nonius KappaCCD diffractometer using graphite monochromated Mo-Kα radiation (λ = 0.71073 Å). Intensities were measured by fine-slicing φ- and ω-scans and corrected for background, polarization and Lorentz effects. A semi-empirical absorption correction was applied for the data sets following Blessing's method.[119] The structure was solved by direct methods and refined anisotropically by the least squares procedure implemented in the ShelX program system.[120] The hydrogen atoms were included isotropically using the riding model on the carbon atoms. Selected data: Crystal dimensions 0.36 x 0.20 x 0.11 mm^3, $C_{15}H_{27}NO_7S$, M = 365.4424, Orthorhombic, space group P 2_1 2_1 2_1, a = 7.44860(10), b = 8.94580(10), c = 28.7024(4) Å, α = 90°, β = 90°, γ = 90°, V = 1912.55(4) Å^3, Z = 4, ρ = 1.269 g cm^{-3}, μ = 0.203 mm^{-1}, F(000) = 748, 18641 reflections ($2\theta_{max}$ = 27.99°) measured (4566 unique, R_{int} = 0.0606,

completeness = 99.4%), R ($I > 2\sigma(I)$) = 0.0708, wR_2 (all data) = 0.2054. GOF = 1.052 for 224 parameters and 14 restraints, largest diff. peak and hole 1.557/-0.438 e Å^3. CCDC-1016532 contains the supplementary data for this structure. These data can be obtained free of charge from www.ccdc.cam.ac.uk/data_request/cif.

2.5.2 Mass spectrometry

ESI mass spectra were recorded on a Bruker APEX IV Fourier-transform ion cyclotron resonance (FT-ICR) mass spectrometer with a 7.05 T magnet and an Apollo electrospray (ESI) ion source equipped with an off-axis 70° spray needle. Analyte solutions were fed into High Pressure PEEK mixing tees from Alltech and then introduced into the ion source with a single- and a dual syringe pump from Cole Parmer and KD Scientific, respectively, at flow rates of 50 µL/h to 16 ml/h. The *continuous-flow* experiments were performed with a setup of two mixing tees. The first one was used for mixing a solution of both butyraldehyde and diethyl ketomalonate (each 2 mmol/L) with a solution of the catalyst (1 mmol/L) and the second mixing tee served for sufficient dilution. Different reaction times were achieved by changing either the length of the capillary connecting both tees or by varying the flow rate. The theoretical reaction time between **1** and the reactants has been calculated from the experimental flow rates considering the volumes of both mixing tees and the connecting capillaries and under the assumption that the dilution in the second mixing tee decreases the reaction rate in the fashion of a bimolecular elementary reaction. For longer reaction times (> 200 s), the results can be compared with the ones from simple ESI measurements recorded at various times after offline mixing of the reaction partners. The results from both techniques match reasonably well, even though the reaction times calculated for the continuous-flow setup seem to be slightly underestimated.

Ionization parameters were adjusted as follows: capillary voltage: -2.380 to -3.800 V; end plate voltage -2300 to 3320 V; capexit voltage: 50 to 100 V; skimmer voltages: 7 to 17 V; temperature of drying gas: 50 to 80 °C. Nitrogen was used as nebulizing (1.38 to 4.14 bar) and drying gas (1.38 to 3.10 bar). The ions were accumulated in the instruments hexapole for 0.3 to 0.9 s, introduced into the FT-ICR cell which was operated at pressures below 10^{-10} mbar, and detected by a standard excitation and detection sequence. Collision-induced fragmentation was performed by on-resonance

excitation with argon gas pulsed into the ICR cell followed by a pumping delay of 3 - 5 s. For each measurement, 8 to 64 scans were averaged. All signal assignments are based on exact mass determinations.

2.6 Acknowledgements

Financial support from the DFG (SFB 624 “templates”) is gratefully acknowledged. We thank Charlotte Rödde and Dr. Gregor Schnakenburg for the X-ray structure determination and Prof. A. C. Filippou for providing X-ray infrastructure.

3 Probing the gas-phase structure of charge-tagged intermediates of a proline catalyzed aldol reaction – Vibrational spectroscopy distinguishes oxazolidinone from enamine species

The results of this Chapter have been published in:

J. A. Willms, J. Vidic, J. Barthelmes, V. Steinmetz, T. Bredow, P. Maître, M. Engeser, *Phys. Chem. Chem. Phys.* **2019**, DOI: 10.1039/c8cp04905j.

Own contributions to the manuscript

- Synthesis of all compounds, that were not commercially purchased
- Measurement,* processing and interpretation of all MS experiments
- Initial DFT optimizations of all geometries that were taken into account for the interpretation of the IRMPD spectra
- Comparison of all theoretical and experimental spectra
- Writing of the manuscript

---

* Recording of the IRMPD spectra was performed under the kind and experienced supervision of Vincent Steinmetz.

3.1 Abstract

An L-proline based catalyst with a charged phenyl-pyridinium substituent (**1**) was used to analyze intermediates of an organocatalyzed aldol reaction by infrared multi-photon dissociation (IRMPD) mass spectrometry after transfer into the gas phase *via* electrospray ionization (ESI). IRMPD spectra were interpreted with the aid of density functional theory (DFT) computations. A structurally restricted enamine species was used as referencing molecule for the calculated vibrational frequencies. A close correlation between theory and experiment was found for the energetically most favoured oxazolidinone structures.

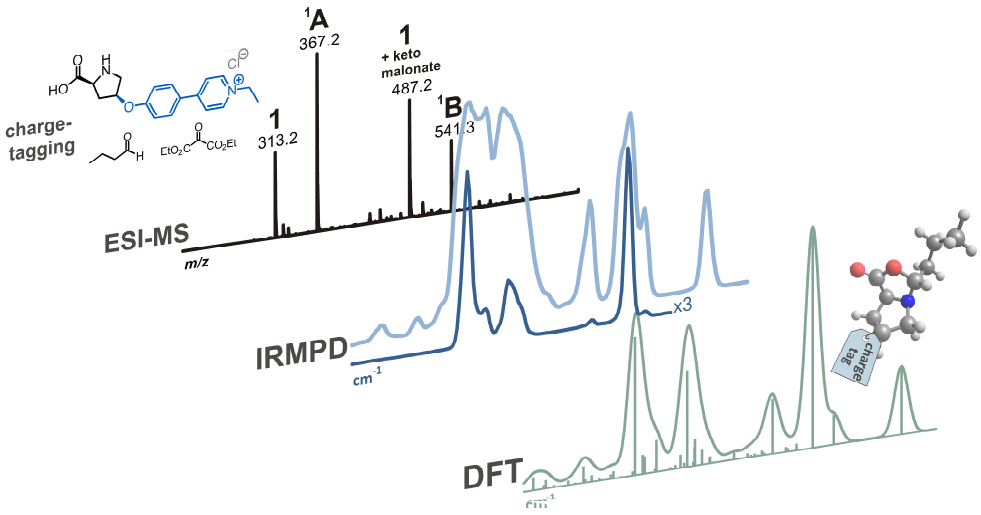

Figure 3.1 – Graphical Abstract of: J. A. Willms, J. Vidic, J. Barthelmes, V. Steinmetz, T. Bredow, P. Maître, M. Engeser, *Phys. Chem. Chem. Phys.* **2019**, DOI: 10.1039/c8cp04905j (Ref. [2]).

3.2 Introduction

During the past two decades, great progress was made in the development of asymmetric organocatalysis for the stereoselective functionalization of carbonyl compounds.[58,87] The principle of using chiral amines to catalyze organic reactions set off a veritable gold rush of publications[55–57,121] and is now an independent branch of stereoselective catalysis, complementary to enzymatic and organometallic catalysis.

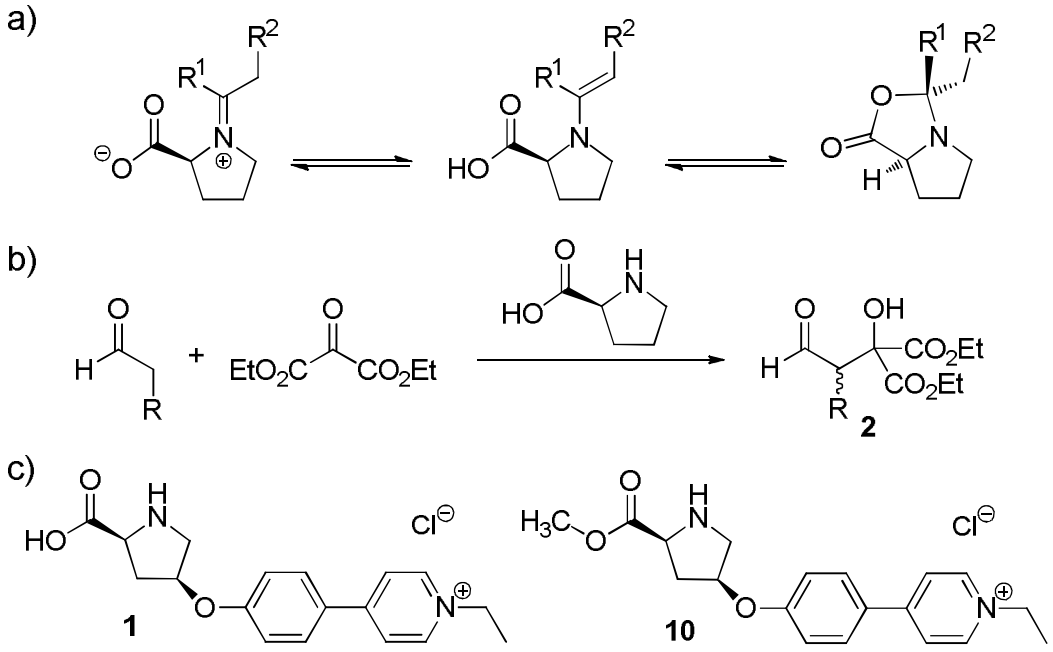

Figure 3.2 – a) Iminium (left), enamine (center), oxazolidinone (right) isomers; b) inverse aldol reaction with aldehyde donors according to *Jørgensen*[112]; c) charge-tagged L-proline derived catalysts **1** and **10**.

This rapid growth of scientific interest was triggered by the pioneering report from *List*, *Lerner* and *Barbas* about an inter- instead of intramolecular[59,60] asymmetric aldol reaction catalyzed by L-proline. An enamine catalyzed mechanism was proposed for the transformation.[61] While a broad variety of different enamine catalyzed reactions (e.g. Aldol,[122,123] Mannich,[124] Michael[125] and also multicomponent reactions[126–128] as well as synergistic catalytic transformations[129–133]) and versatile optimized catalysts[58,134–136] have been developed since then, opinions still differ on some mechanistic details of enamine catalysis. For reactions catalyzed by L-proline, it is generally agreed that the reactive key intermediate is an enamine carboxylic acid and/or an enamine carboxylate.[61,64,65,92,96,110,137–145] Yet its formation and the distinct role of

isomeric oxazolidinone species in the catalytic cycle remain uncertain (Figure 3.2a)).[92,110,138–142] The most commonly accepted mechanism for enamine catalysis was first proposed by *List* and *Houk* (Figure 3.3).[64,65,137]

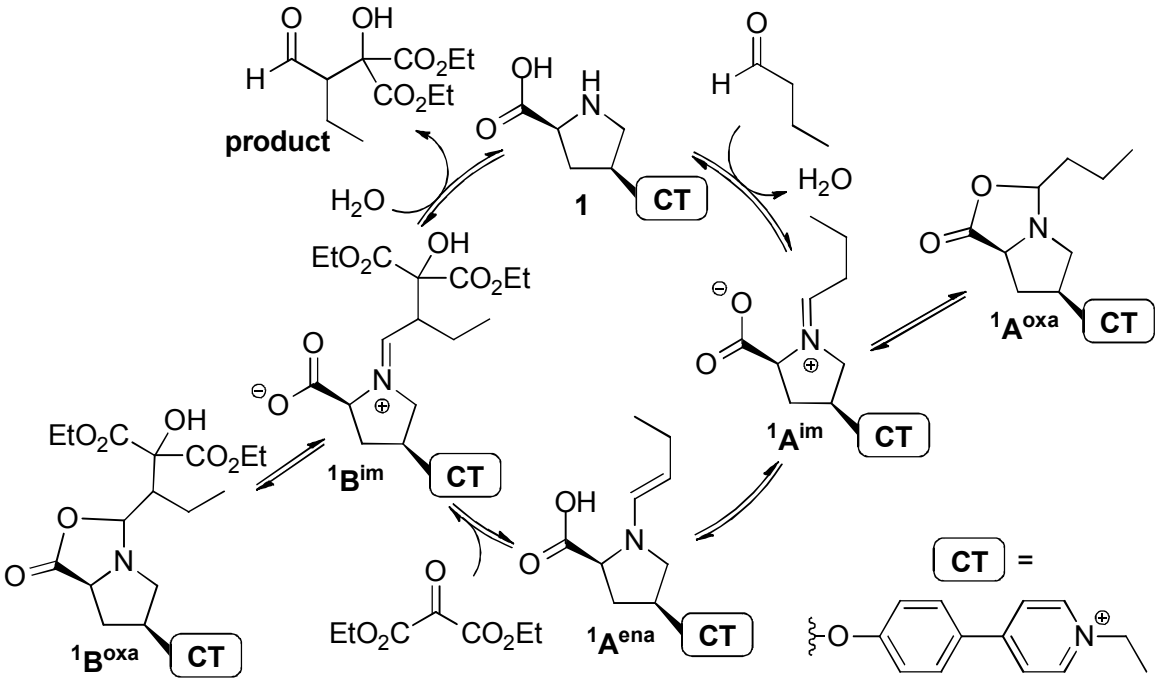

Figure 3.3 – Catalytic cycle of the aldol reaction with aldehyde donors catalyzed by **1**;[1,64,65,137] Intermediate notation used herein: Letter (**A**/**B**) with superscript (1/2) for the respective catalyst and superscript acronym (oxa/ena/im) for the isomeric structure.*

Electrospray ionization mass spectrometry[6] is a powerful analytical method that has evolved into an established technique to investigate reaction mechanisms.[14,28,75,146–148] ESI of reacting solutions allows monitoring the reaction progress and characterizing intermediates with tandem mass spectrometry. The sensitivity of ESI is very high for ionic species, while uncharged derivatives cause lower intensities or could even be suppressed by species with a better ESI response.[23] One way to improve the detection of specific derivatives is the charge tag strategy: A covalently attached charged substituent drastically increases the ESI response of the target compounds.[29–31,78,149,150] Established charge tags are cationic ammonium[31,149,151] or phosphonium[29,152] as well as anionic sulfonate[153–155] residues. Charge tags can basically be introduced into every

* Note that the designation system of the intermediate structures differs from the used notations in Chapter 2 for a clearer description of the different isomeric molecular structures. (e.g., $^{1}\mathbf{A}^{\mathbf{oxa}}$ in Chapter 3 is equivalent to species **II''b** in Chapter 2.)

component of a reaction, e.g. reagents[29,30,78,149,151,152] or catalysts/catalyst ligands.[86,153,155]

In a previous study (see Chapter 2),[1] we used the charge-tagged L-proline-derived organocatalyst **1** (Figure 3.2c)) with a 1-ethylpyridinium-4-phenoxy substituent to successfully detect intermediates of an inverse aldol reaction published by *Jørgensen* and coworkers.[112] **1** showed a strongly enhanced ESI response compared to unmodified L-proline (Figure 3.2b)). The rigid phenylpyridine linker separates the charge tag from the catalytically active center, the pyrrolidine nitrogen, in order to avoid unintended interactions. The use of **1** enabled the mass spectrometric detection of two key intermediates of the List-Houk mechanism for enamine catalysis and also a dead end species derived from the catalyst and diethyl ketomalonate. Reaction monitoring revealed a qualitative picture of the temporal evolution of catalyst **1**, intermediates and aldol product.

Probing the reactivity of a transient species present among and possibly in fast equilibrium with many others in the complex mixture of a reacting solution is a very difficult task.[156] One experimental approach to access the intrinsic reactivity of a specific intermediate is to study isolated ions under well-defined conditions in the gas phase.[157–159] These experiments can yield very valuable insight[160,161] although one has to keep in mind that the reactivity in the gas phase does not necessarily directly parallel the one in solution. With our charge-tagged proline derivative, we observed intermediates in sufficient abundances for gas-phase reactivity studies. However, a prerequisite for these is a well-defined structure of the reactant ion. In our case, three possible isomers are discussed to play a role in solution (Figure 3.2a)) and the situation might further be changed after transfer into the gas phase. Thus, a proper structural characterization of the detected gas-phase ions is inevitable. Collision induced dissociation (CID) of the intermediate species only showed the loss of carbon dioxide. It was thus impossible to discriminate between enamine, oxazolidinone and iminium isomers for an unambiguous structure assignment of the detected *m/z* values by simple CID experiments. For that reason, we aimed to elaborate on these results with a study based on action photodissociation spectroscopy.

Infrared multi-photon dissociation (IRMPD) spectroscopy[33–36] of trapped ions in the gas phase has developed into an effective tool for structure elucidation of ions. There

are only few examples regarding the investigation of organocatalytic species.[162] This method commonly requires a highly intense and tunable laser beam from a free electron laser (FEL) which has been particularly well suited for probing the mid-infrared fingerprint region.[39–41]

In this manuscript, we present IRMPD spectra in the mid-IR range of two ions obtained by transferring charge-tagged intermediates of L-proline catalyzed aldol reactions into the gas phase via ESI and the corresponding quantum chemical calculations. The study aims at a structural characterization of gas-phase variants of key intermediates of the List-Houk catalytic cycle.

3.3 Methods

3.3.1 Mass spectrometry and IRMPD spectroscopy

Measurements were performed on a commercial 7 T hybrid Fourier transform ion cyclotron resonance (FT-ICR) mass spectrometer (Bruker apex-Qe) equipped with an Apollo II ESI source coupled to the tunable IR free-electron laser (FEL) of CLIO[39] (Centre Laser Infrarouge d'Orsay).[163,164]

Analyte solutions were fed into a setup of two PEEK mixing tees (Alltech) which was directly coupled to the ESI source (Figure S3.1, Appendix S3).[1] In the first mixing tee, substrates dissolved in acetonitrile (butyraldehyde and diethyl ketomalonate: each [2 mM]; acetone: [10 % v/v]) were mixed with acetonitrile solutions of catalyst **1** [1 mM]. The second mixing tee served to sufficiently dilute the reacting solution for ESI. The flow rates were adjusted to set a theoretical reaction time of approximately 70 s. Experiments with catalyst **10** did not require a complicated setup due to its lower reactivity. Catalyst **10** [1 mM] was simply mixed with the reactant acetone (50 % v/v) in acetonitrile and electrosprayed directly.

The ions of interest were mass-selected with the quadrupole mass filter (if necessary*) and accumulated in an argon-filled (10^{-3} mbar) hexapole ion trap, also allowing for

* The analyzed intermediates ^{1}**A** and ^{1}**B** show a very simple fragmentation pattern: Only elimination of carbon dioxide is observed (Figure S3.5 and S3.6, Appendix S3). Therefore, both ions can be irradiated simultaneously for the acquisition of IRMPD spectra without any previous mass selection. Subsequent data processing to derive the respective energy dependent fragmentation efficiencies can be carried out independently.

thermalization. The ions were extracted to the ICR cell where they were irradiated for 180–1000 ms with infrared light in the 900–1900 cm^{-1} spectral range. Four mass spectra were recorded and averaged for each wavelength. Repeated and sufficient photon absorption at a fundamental vibrational frequency of a given ion led to unimolecular dissociation which was quantified by monitoring the signal intensities of parent and fragment ions in the resulting mass spectra. The fragmentation yield ($Y_{frag} = -\ln(I_{precursor}/[I_{precursor} + \Sigma I_{fragments}])$) was plotted against the respective photon energy to obtain the presented IRMPD spectra.

IR spectra were recorded using varying degrees of attenuation of the IR laser beam (-3 to -15 dB). High laser fluence in conjunction with large IR absorption cross-section may lead to saturation effects, which are accompanied by band red-shifts. Conversely, in the case of the reference ion $\mathbf{^{10}A^{ena}}_{(acetone)}$ (Figure 3.4), an auxiliary broadband CO_2 laser pulse (BFi OPTiLAS, Evry, France) had to be used in order to enhance the fragmentation yield. A 30 ms long CO_2 pulse following each IR-FEL pulse with a delay of a few μs was used.[165]

3.3.2 DFT calculations

Minima for the examined ions were searched using the Minima Hopping (MH)[166] algorithm employing the GPAW[167] code within the ASE framework.[168] The wavefunction was calculated with the PBE functional using a dzp (double-zeta valence plus polarization functions) basis set. Molecular dynamics (MD) simulations were performed with initial temperatures between 325 K and 400 K. The number of MD steps for each MH cycle was restricted to 250. The MH structures with lowest energy were subsequently fully optimized and their vibrational frequencies were calculated at the B3LYP-D3[169,170]/def2-TZVP[171] level using the Gaussian 09 program package.[172] For comparison with IRMPD spectra, calculated bands (applied scaling factor: 0.979) were convoluted with a gaussian profile with a full width at half maximum (FWHM) of 20 cm^{-1}.

3.4 Results and discussion

IRMPD is potentially an isomer specific activation mode providing that each isomer has distinct IR signatures. The spectral shifts of carbonyl CO stretching bands could serve as a distinct feature for the enamine $^{1}\mathbf{A}^{\mathbf{ena}}$ (carboxylic acid), oxazolidinone $^{1}\mathbf{A}^{\mathbf{oxa}}$ (lactone) or iminium $^{1}\mathbf{A}^{\mathbf{im}}$ (carboxylate) species.

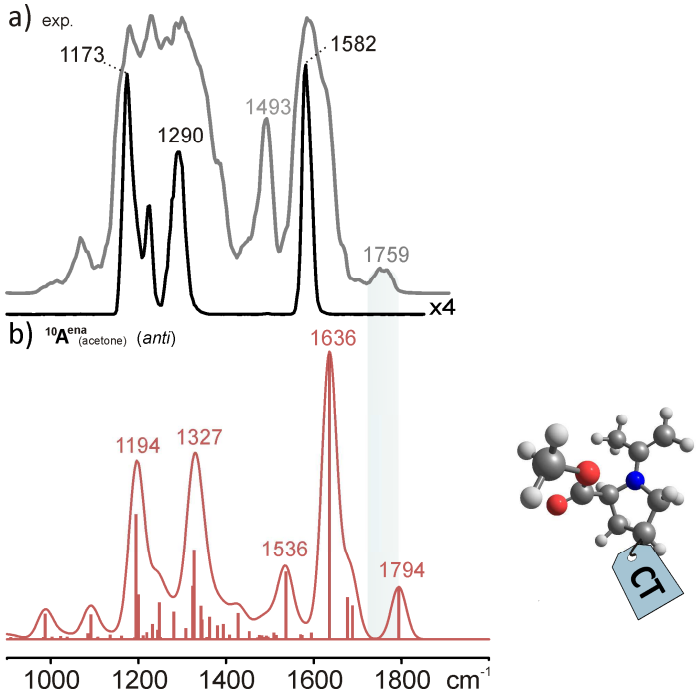

Figure 3.4 – a) IRMPD spectra of $^{10}\mathbf{A}^{\mathbf{ena}}_{(acetone)}$ (*m/z* = 367) with 3 dB attenuation of the IR laser (black) and with an additional CO_2 laser pulse (grey); b) unscaled calculated (B3LYP-D3/def2-TZVP) spectrum of $^{10}\mathbf{A}^{\mathbf{ena}}_{(acetone)}$ (*anti*); C=O stretching highlighted; CT = phenyl-pyridinium charge tag (complete structure in Appendix S3).

Interpretation of IRMPD spectra in most cases requires comparison with calculated harmonic vibrational frequencies that are commonly derived at the density-functional theory (DFT) level. The calculated frequency values are often larger than the experimental ones due to the harmonic approximation and limitations of the quantum chemical methods. Thus, theoretical frequencies are often uniformly scaled.[43,44]

3.4.1 Scaling approach.

Finding suitable scaling factors is a non-trivial task.[173] We thus decided to derive an individual scaling factor from experimental IRMPD spectra of a closely related

reference compound for which a single enamine isomer is expected. We therefore synthesized the "blocked" catalyst **10** with a methyl ester group (Figure 3.2c)) and mixed it with an excess of acetone in acetonitrile to form enamine $^{10}\mathbf{A}^{ena}_{(acetone)}$ before ESI-MS analysis. $^{10}\mathbf{A}^{ena}_{(acetone)}$ can neither undergo lactonization to the corresponding oxazolidinone nor form a singly charged iminium ion scaffold *via* hydrogen transfer.

Table 3.1 – Calculated (B3LYP-D3/def2-TZVP) vibrational frequencies (in units of cm^{-1}), experimental IR bands and derived scaling factors for selected reference compounds.

Species	IR mode	Exptl. IR	Exptl. IRMPD	Theory	Ratio exp/theory
4-phenyl-pyridine	$\delta'_{CH}, \delta''_{CH}$	1480[c]		1522 (17.9)	0.972
4-phenyl-pyridine	δ'_{CH}	1217[c]		1250 (5.6)	0.974
methyl acetate	ν_{CO}	1769[d]		1815 (351)	0.975
γ-butyro-lactone	ν_{CO}	1822[c]		1856 (419)	0.982
$^{10}\mathbf{A}^{ena}_{(acetone)}$	ν_{CO}		1759	1794	0.980
$^{10}\mathbf{A}^{ena}_{(acetone)}$	s.v.		1582[e]	1636	0.968
$^{10}\mathbf{A}^{ena}_{(acetone)}$	$\delta'_{CH}, \delta''_{CH}$		1493	1536	0.972
$^{10}\mathbf{A}^{ena}_{(acetone)}$	s.v.		1290[e]	1327	0.972
$^{10}\mathbf{A}^{ena}_{(acetone)}$	δ'_{CH}		1223[e]	1248	0.979
$^{10}\mathbf{A}^{ena}_{(acetone)}$	s.v.		1173[e]	1194	0.982

[a] ν = stretch; δ = in-plane bend; 'pyridine unit, "phenyl unit, s.v. = three or more superposed vibrations; [b] without scaling; calculated IR intensities (in parentheses) in km/mol; [c] from Ref. [174]; [d] from Ref. [175]; [e] 3 dB attenuation of the IR laser.

We tested the B3LYP-D3[169,170], PBE-D3[176], HCTH93[177] and HCTH407[178] functionals to determine vibrational frequencies of $^{10}\mathbf{A}^{ena}_{(acetone)}$ and compared the calculated IR spectra with the experimental IRMPD spectra (Figure 3.4a). The TZVP (triple-zeta valence plus polarization functions) basis set was found to provide satisfactory results. Altogether, computations at the B3LYP-D3/def2-TZVP level

showed the best matching of calculated and measured band shapes and positions and were thus used for structural analysis of the IRMPD spectra.*

The agreement between the computed IR spectrum and the experimental IRMPD spectrum of enamine derivative $^{10}\mathbf{A}^{\mathbf{ena}}_{(\text{acetone})}$ is satisfactory (Figure 3.4). Calculated and experimental IRMPD frequencies are provided in Table 3.1. This table also includes experimental values[180] of vibrational frequencies of simple model molecules, which are compared to calculated values at the chosen level of theory. The scaling factor derived from the C=O stretching vibrational mode (ratio exp/theory) is 0.98, which is in good accordance with reported values for a comparable level of theory.[181] Inspection of Table 3.1 suggests that a uniform scaling would be adapted in the present case. Since the diagnostic vibration for structural elucidation is the C=O stretching mode, we chose 0.979 as general scaling factor for the calculations at the B3LYP-D3/def2-TZVP level.

3.4.2 IRMPD experiments

Intermediate species of the aldol reaction (Figure 3.2b)) catalyzed by **1** were generated and transferred into the gas phase using a setup of two mixing tees directly coupled to the ESI source (Figure S3.1, Appendix S3). Reaction intermediates of a defined and constant reaction time could thus be measured continuously (longer than one hour). This made it possible to perform IRMPD spectroscopy within a spectral range of 1000 wavenumbers in a single run. Ionic reaction intermediates were detected in high abundance when mixing catalyst **1** with butyraldehyde and diethyl ketomalonate in acetonitrile using the described setup (Figure S3.2, Appendix S3).[1] IRMPD spectroscopy of the intermediates $^{1}\mathbf{A}$ (*m/z* = 367) and $^{1}\mathbf{B}$ (*m/z* = 541) and the implications for their gas-phase structures is reported in the following.

* When focusing on the experimentally determined C=O stretching band of $^{2}\mathbf{A}^{\mathbf{ena}}_{(\text{acetone})}$ (1759 cm^{-1}), DFT computations on the HCTH93/def2-TZVP level showed the best agreement (1766 cm^{-1}) and scaling was not required.[179] Nevertheless, the overall spectral shape and frequency values of other IRMPD spectra were much better described with B3LYP-D3/def2-TZVP.

3.4.3 IRMPD of species ^{1}A

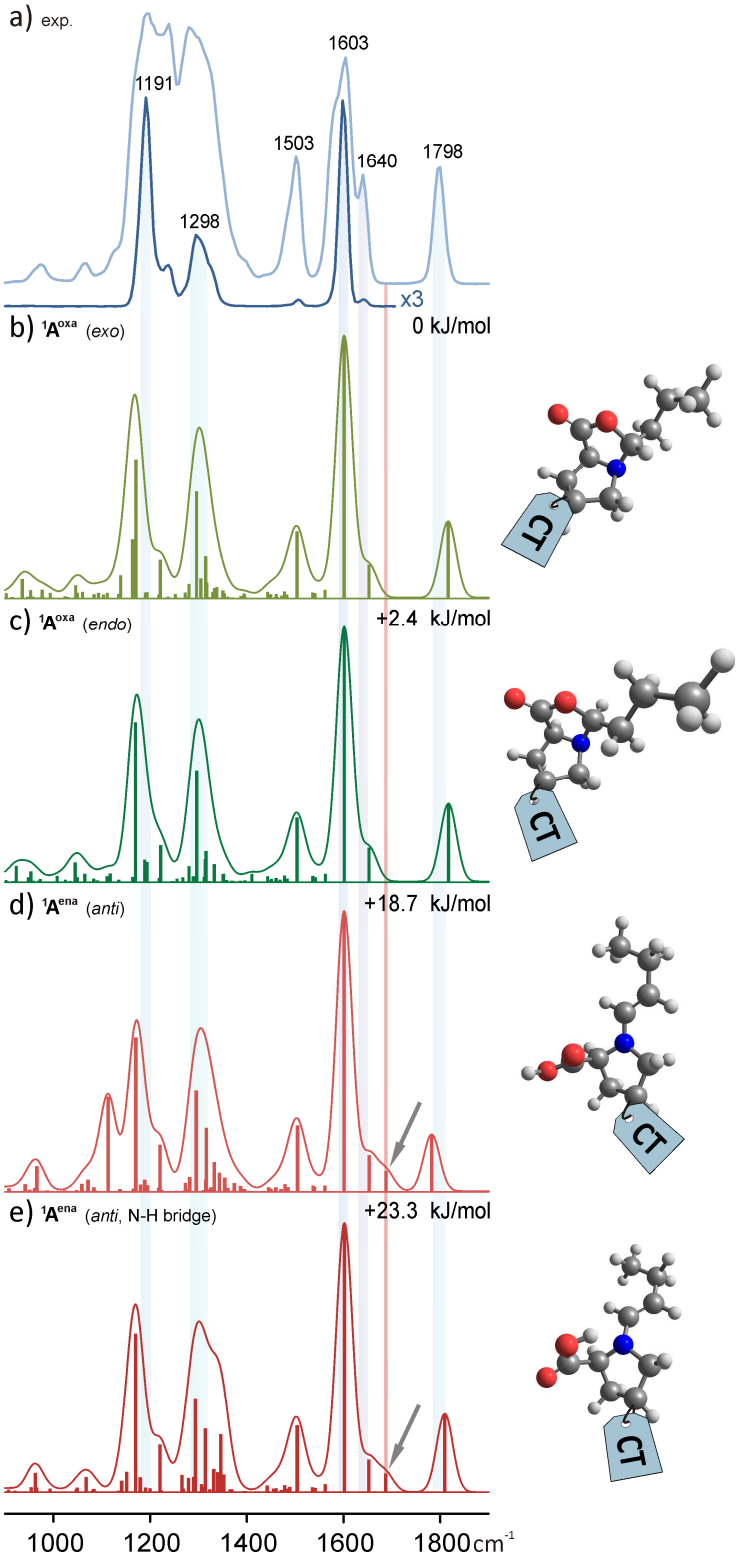

Figure 3.5 – a) IRMPD spectra of ^{1}**A** (*m/z* = 367) with 3 dB (light blue) and 12 dB (blue) attenuation; b) calculated* IR spectrum of $^{1}\mathbf{A}^{oxa}$ (*exo*); c) calculated* IR spectrum of $^{1}\mathbf{A}^{oxa}$ (*endo*); d) calculated* IR spectrum of $^{1}\mathbf{A}^{ena}$ (*anti*); e) calculated* IR spectrum of $^{1}\mathbf{A}^{ena}$ (*anti*, with N-H bridge); *B3LYP-D3/def2-TZVP (scaling: 0.979); CT = phenyl-pyridinium charge tag (complete structures in Appendix S3); Relative stabilities of the calculated isomers are given on the top right of each spectrum.

Reactive intermediate $^{1}\mathbf{A}$ is formed from catalyst **1** and butyraldehyde by condensation (Figure 3.3). Essentially, three different structures have to be considered for this ion: enamine $^{1}\mathbf{A}^{ena}$, oxazolidinone $^{1}\mathbf{A}^{oxa}$ and iminium species $^{1}\mathbf{A}^{im}$ as well as several conformational isomers (e. g. *syn*/*anti* enamines) and configurational isomers (e. g. *E*/*Z* iminium derivatives and *endo*/*exo* oxazolidinones) thereof.

Iminium derivatives derived from L-proline and small ketones or aldehydes were found to be energetically less preferred than the corresponding enamines and oxazolidinones at the DFT level.[138,182,183]* In the present case, no minimum corresponding to an iminium ion could be found. We observed lactonization of iminium structures to the corresponding oxazolidinone isomers during optimization before the first MD step in the course of the Minima Hopping procedure.[166,167] Thus, the presence of any iminium species in the gas phase of the mass spectrometer was ruled out as there are no stabilizing solvation effects. The detected species either possess an oxazolidinone or an enamine scaffold.

Figure 3.5 shows two IRMPD spectra of the ion $^{1}\mathbf{A}$ (*m/z* = 367) compared to calculated IR spectra for the four energetically most preferred structures. The two spectra were recorded using two different grades of attenuation of the CLIO laser beam. Overall, a striking resolution with well-defined bands was achieved. The narrow band in the C=O stretching region at 1798 cm^{-1} has a width (FWHM) of 28 cm^{-1} in good accordance with an IRMPD band resulting from one single infrared active mode.[185] This suggests that the examined ion cloud predominantly consists of one species.

According to the DFT calculations, all other pronounced IRMPD bands result to a large extent from vibrational features of the charge-carrying 1-ethylpyridinium-4-phenoxy unit, similar to the findings for $^{10}\mathbf{A}^{ena}_{(acetone)}$. For instance, the intense bands at 1603 cm^{-1} and 1191 cm^{-1} mostly result from C=C stretching and C–H bending vibrations of both aromatic rings of the charge tag.

Overall, the enamine rotamers were found to be higher in energy than the oxazolidinone forms. The calculated structure of the *exo* isomer is slightly more stable than the *endo* analogue which is in accordance with previous calculations on comparable structures

* This situation changes when solvation effects are considered which are negligible in the present case.[182,184] Conceivable iminium structures are expected to convert into oxazolidinone species during the transfer from solution into the gas phase in our experiment.

without a charge-tagging unit.[138,182] A preference for the *exo* form was also reported in experimental and theoretical studies of comparable derivatives in solution,[92,141,182,186] where *exo* oxazolidinones are in equilibrium with minor amounts of the corresponding endo species.

A very high correlation between calculations of (*exo* and *endo*) oxazolidinone species (Figure 3.5b),c)) and the IRMPD spectrum of **^{1}A** (Figure 3.5a)) was observed. The most intense bands, observed with laser attenuation (blue), at 1191, 1298, 1503, 1603, 1640, and 1798 cm^{-1} nicely match with the most intense predicted IR absorption bands of the lowest energy structure. At the highest laser fluence (light blue), two predicted weak absorption features below 1100 cm^{-1} are also observed in the IRMPD spectrum. The observed CO stretching frequency is 1798 cm^{-1}. It can be compared to the 1759 cm^{-1} band observed for the reference compound, which could be unambiguously assigned to an ester carbonyl stretch. The 1798 cm^{-1} band could thus be assigned to a lactone carbonyl stretch.

The IR spectra calculated for the higher energy enamine isomers do not fit to the experimental spectra as well Figure 3.5d),e). The DFT calculations yielded two energetically low-lying enamine structures. Both structures have an *E*-configurated C=C double bond which is oriented anti towards the carboxylic acid function. *Gschwind* and coworkers proved the presence of this conformation for enamines in solution by NMR of species derived from L-proline and propionaldehyde.[92] One of the two calculated energetically low-lying enamine structures features a hydrogen bond between the nitrogen atom of the pyrrolidine unit and the hydrogen of the carboxylic acid function. The C=O bond length is slightly shorter (1.198 Å) in this enamine structure (Figure 3.5e)) compared to the respective structure without N-H hydrogen bonding (1.200 Å, Figure 3.5d)), which causes a weak blue-shift of the C=O stretching band by ~30 cm^{-1}.

The distinctive feature of both enamine conformations however is the C=C stretching vibration below 1700 cm^{-1} (highlighted in Figure 3.5 with arrows and a red bar). This band helps distinguishing the putative enamine conformations from the experimental ones: It is not observed in the experiment even when full IR laser power is used. The IR spectrum in the C=C stretching region is thus consistent with theory which predicts the

enamine isomers too high in energy to be significantly populated at room temperature. It can thus be concluded that the examined ions **^{1}A** do not possess an enamine structure.

In summary, the IRMPD spectra revealed an oxazolidinone structure for **^{1}A** in the gas phase. A mixture of both *exo* and *endo* isomers with higher amounts of *exo* isomers is likely. No evidence was found for enamines in accordance with findings reported for acetonitrile solutions.[92] Enamines which are considered to be key intermediates of L-proline catalyzed aldol reactions might still be present however in an equilibrium between stable oxazolidinone species and very small amounts of transient enamine intermediates which cannot be monitored due to insufficient sensitivity of our experimental setup.

3.4.4 IRMPD of species ^{1}B

Signals for species **^{1}B** (*m/z* = 541) were detected in excellent abundances. As depicted in Figure 3.3, **^{1}B** is formed out of **^{1}A^{ena}** by nucleophilic addition of the second carbonyl substrate, i.e. diethyl ketomalonate. The last step in the proposed catalytic cycle then is hydrolysis of **^{1}B** to form the aldol product and recover the catalyst. This hydrolysis is expected to occur *via* an iminium species.[61,138,183,184] The structure of the ions **^{1}B** was analyzed using the same procedure as above. Again, three isomeric oxazolidinone, iminium and enamine structures as well as different constitutional or configurational isomers thereof had to be considered as possible geometries of **^{1}B**. The stereoselectivity of the reaction was taken into account.[112]*

Figure 3.6 shows the comparison of two IRMPD spectra of ion **^{1}B** (*m/z* = 541) with calculated IR spectra for energetically low-lying structures. Two carbonyl bands are observed at 1759 and 1799 cm^{-1}. Based on the above discussion on the **^{10}A^{ena}**$_{(acetone)}$ and **^{1}A** ions, these two bands can be assigned to ester and lactone carbonyl stretches respectively. The theoretical IR spectrum of the *exo* oxazolidinone structure (Figure 3.6b)), which is predicted to be the lowest energy isomer, matches the experimental spectrum very well. Although the frequencies of the C=O stretching vibration are slightly overestimated, all vibrational bands are sufficiently reproduced. In

* In approximation, the reaction was considered to yield exclusively the (*S*)-product. In any case, the spectral features of interest may not be affected significantly by the configuration of the ketomalonate periphery.

contrast, calculated and measured spectra of the corresponding endo oxazolidinone do not correlate as well.

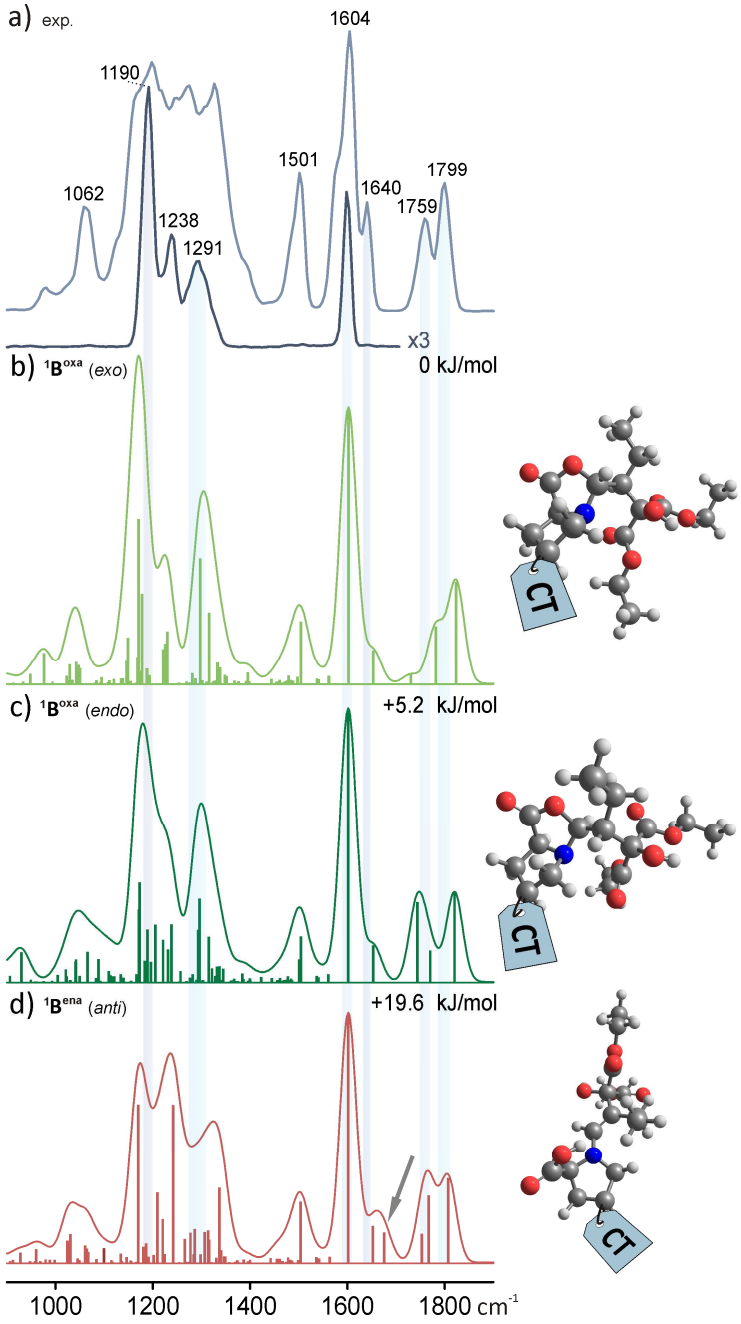

Figure 3.6 – a) IRMPD spectra of ^{1}**B** *(m/z* = 541) with 3 dB (pale blue) and 12 dB (dark blue) attenuation; b) calculated* spectrum of ^{1}**B**^{oxa} (*exo*); c) calculated* spectrum of ^{1}**B**^{oxa} (*endo*); d) calculated* spectrum of ^{1}**B**^{ena} (*anti*); *B3LYP-D3/def2-TZVP (scaling: 0.979); CT = phenyl-pyridinium charge tag (complete structures in Appendix S3); Relative stabilities of the calculated isomers are given on the top right of each spectrum.

As mentioned above, we observed cyclization to the respective oxazolidinone analogues when iminium structures were optimized in the course of the Minima Hopping procedure. Therefore, iminium species were not included in the theoretical interpretation of the experiment. Nonetheless, deprotonation of the carboxylic acid function to form any iminium isomers would cause a significant shift of the carboxylate stretching modes to lower frequencies which was not observed in the IRMPD spectra.[187,188]

The enamine isomer exhibits an *E*-anti conformation of the C=C double bond. In addition to poor matching between theory and experiment in the range 1300–1400 cm^{-1}, there was no experimental indication for the C=C stretching vibration below 1700 cm^{-1}. According to the IRMPD spectra species **^{1}B** thus consists of an oxazolidinone scaffold with an *exo*-directed hydroxy-malonate unit. In accordance with the results for **^{1}A**, the thermodynamically preferred oxazolidinone structure was obtained for **^{1}B** as well. The presence of minor amounts of other isomeric species however cannot be excluded.

3.4.5 Additional remarks

The photodissociation experiments on **^{1}A** and **^{1}B** in the range of 900–1900 cm^{-1} both revealed an *exo* oxazolidinone structure. Another diagnostic mode for further confirmation of the results is the O–H stretching frequency. Unfortunately, our attempts to derive IRMPD spectra in the range of 3200 to 3700 cm^{-1} using a benchtop optical parametric oscillator/amplifier (OPO/OPA) laser coupled to a CO_2 laser[189] were not sufficiently reliable due to insufficient fragmentation yield of the analyzed ions. We further probed the ions by gas-phase hydrogen-deuterium exchange[190] (HDX) experiments. No hydrogen exchange could be observed for **^{1}A** and **^{1}B** when applying conditions under which HDX of the acidic hydrogen of the catalyst **1** was successful. Since the oxazolidinone structures do not bear any acidic protons, these experiments are in full accordance with the IRMPD results.

In addition, we recorded IRMPD spectra in the range of 900–1900 cm^{-1} of **^{1}A**$_{(acetone)}$ derived from catalyst **1** and acetone (Figure S3.9, Appendix S3). A comparison of the experimental spectrum with calculated spectra of putative structures again indicates an oxazolidinone species although the distinction is less concise in this case.

The calculated IR spectra match the experimental IRMPD spectra rather well. However, even better frequency values would still be desirable. Vibrational frequencies were calculated at the B3LYP-D3[169,170]/def2-TZVP[171] level and scaled with an empirical factor derived from measurements of the reference molecule $^{10}\mathbf{A}^{\mathbf{ena}}_{(\text{acetone})}$. Indeed, $^{10}\mathbf{A}^{\mathbf{ena}}_{(\text{acetone})}$ has a well-defined atomic arrangement and is structurally very closely related to the ions of interest $^{1}\mathbf{A}$ and $^{1}\mathbf{B}$. It is thus well-suited as a reference molecule. Yet, it exhibits a significantly lower fragmentation efficiency which is illustrated by the comparatively high energy required for CID of this ion (see Figure S3.5-8, Appendix S3). As a result, the internal energy of the molecule is higher in the course of the IRMPD experiment due to the enhanced irradiative excitation which leads to slightly broadened, red-shifted bands and thus a reduced comparability of this molecular reference.[191,192] Also, theoretical spectra could be further refined. The computed derivatives show several structurally closely related local minima. An adequate number of lowest minima structures of a given derivative could be taken into account in terms of a Boltzmann distribution. The latter could be used to produce an IR spectrum of the Boltzmann-weighted computed vibrational frequencies. We chose the 32 most stable rotamers of $^{1}\mathbf{A}^{\mathbf{oxa}}$ to illustrate their impact on the theoretical IR spectrum. Vibrational frequencies were calculated for each structure and an averaged IR spectrum was created taking into account the percentage shares of the individual isomers according to a Boltzmann weighting of the respective calculated relative stabilities. Since these local minima are structurally very similar, the resulting theoretical IR spectra hardly differ and the Boltzmann-weighted average closely matches the spectrum of the most stable isomer (Figure S3.11, Appendix S3). Thus, the consideration of only the most stable isomer does seem to be justified in this case.

3.5 Conclusions

The charge-tagged organocatalyst **1** is well suited to capture intermediates of L-proline catalyzed reactions by ESI mass spectrometry. IRMPD spectra of the ions detected when spraying a reacting solution revealed a clear and consistent picture of the structures in the gas phase. The detected ions $^{1}\mathbf{A}$ and $^{1}\mathbf{B}$ both are *exo* oxazolidinones. The presence of minor amounts of the respective *endo* oxazolidinones or other species

below the detection limit of our experiment cannot be ruled out.[92,141,182,186] The timescale to detect reacting species with our setup is in the order of seconds which unfortunately prevents us from probing short lifetime species.

The verification of the predominant presence of oxazolidinone species for the examined gas-phase ions $^{1}\mathbf{A}$, $^{1}\mathbf{B}$ and $^{1}\mathbf{A}_{(acetone)}$ is a significant result. It is in accordance with the energetic profile of the respective isomeric enamine, iminium and oxazolidinone species (Figure 3.3). In each case, the oxazolidinone structure is the thermodynamically most favored one in the gas phase. This result is fully consistent with the findings for proline-catalyzed reactions in solution obtained by NMR spectroscopy.[92]

The distinctive feature of our approach is the charge-tagging substituent. Uncharged species typically are protonated during the electrospray ionization process,[63] which results in a drastic change of the chemical nature of the species. In contrast, the use of charge-tagged catalyst **1** enables the transfer of oxazolidinone intermediates in the gas phase while leaving their chemical character unaffected. It thus allows an analysis of the gas-phase behavior of intact oxazolidinone derivatives. We currently are studying their gas-phase reactivity against volatile carbonyl compounds which could help to gain a deeper understanding of the role of oxazolidinone species in the course of enamine catalysis.

3.6 Acknowledgements

We thank the whole CLIO team for technical assistance. Financial support from European Community's Framework Programme Horizon 2020 (CALIPSOplus, under grant agreement 730872) and from the French FT-ICR network (FR3624 CNRS) is gratefully acknowledged. Furthermore, we thank the Deutsche Forschungsgemeinschaft (SFB 813) for financial support.

PART III

Using an electrochemical flow cell for the ESI-MS study on an oxidative coupling reaction

Preamble of Part III

The catalytic functionalization of organic compounds by C-H activation is a very attractive and atomic-economic way to construct new C-C as well as C-X bonds without the assistance of directing groups and therefore is of considerable benefit for organic syntheses. In recent years, various metal catalytic as well as metal free approaches have been established to manipulate the reactivity of the normally thermodynamically stable carbon-hydrogen bond.[193] One part of this brought field is oxidative coupling of tertiary amines[194,195] and a pronounced research activity was initiated by the pioneering works of *Murahashi*[196] and *Li*[197]. In this respect, considerable interest in derivatives of Tetrahydroisochinolines (THIQs), which are common structural motifs in alkaloids,[198] emerged and effective nucleophiles as well as catalyst/oxidant systems for their functionalization have been developed.[195] However, the circumstance that a significant amount of publications deals with the derivatization of *N*-aryl-THIQ compounds is certainly also due to a lower reactivity of, for example, acylated analogues.[199] Since the removal of the phenyl group is difficult,[200–202] it can be disadvantageous in subsequent synthetic steps. Therefore, efficient coupling of alternative THIQ derivatives is desirable.[203–207] A deeper understanding of the underlying mechanisms of such reactions could provide a basis for further extension of the substrate scope.

As part of Prof. Dr. Dirk Menche's project in the SFB (Sonderforschungsbereich, Collaborative Research Center) 813, Tongtong Wang evaluated a new method for the C-1-alkylation of THIQs with diethylzinc. This oxidative coupling reaction was proposed to proceed *via* a radical mechanism.[208] When *Wang* presented his results at an SFB conference, the subsequent discussion gave rise to the idea of experimentally proving or refining the proposed reaction mechanism using electrospray mass spectrometry (ESI-MS) in a cooperative project between the *Engeser* and *Menche* groups. With a first ESI-MS screening of the reaction mixture with the unbiased aim to detect radical species, a completely new research series started within the course of this thesis. As part of the analytics, linking of a commercial electrochemical flow cell with the ESI source revealed deeper insight in the formation of the iminium key

intermediate. The experiments encouraged a comparison of the MS data with cyclovoltammograms of the investigated THIQ substrates, which were thus recorded. The eventual outcome was an interdisciplinary mechanistic study presented in Chapter 4.

4 Investigations of the copper-catalyzed oxidative cross-coupling of tetrahydroisoquinolines with diethylzinc by a combination of mass spectrometric and electrochemical methods

The results of this Chapter have been published in:
J. A. Willms, H. Gleich, M. Schrempp, D. Menche, M. Engeser, *Chem. Eur. J.* **2018**, *24*, 2663–2668.

Own contributions to the manuscript

- Synthesis of some compounds, that were not commercially purchased
- Design of MS experiments
- Measurement, processing and interpretation of all MS and EC-MS experiments (i.e. reaction monitoring, voltage-dependent ion intensity curves, EC synthesis)
- Measurement and processing of all CV curves
- Writing of the manuscript

4.1 Abstract

The aerobic oxidative cross-coupling of tetrahydroisoquinolines (THIQs) with diethylzinc catalyzed by $CuCl_2$ has been examined by means of electrospray mass spectrometry (ESI-MS). Substrates, intermediates, and the product were readily detected. Particular emphasis has been placed on the role of $CuCl_2$. Formation of the intermediate iminium species has been investigated in more detail by ESI-MS, electrochemistry-coupled ESI mass spectrometry, and cyclic voltammetry. Our experiments have consistently revealed strong influences of the *N*-substituent of the THIQ derivative and its oxidation stability with respect to $CuCl_2$. The results may help to expand the synthetic scope of the reaction, while also further establishing EC-MS as a valuable technique for linking mass spectrometry with cyclic voltammetry in mechanistic studies of organic redox reactions.

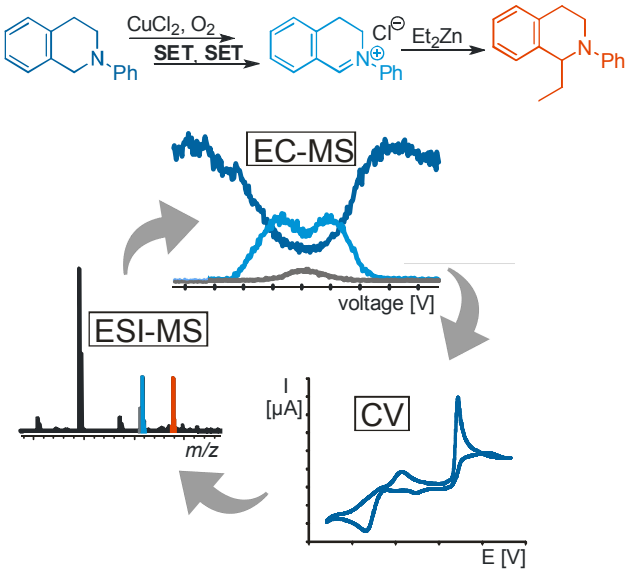

Figure 4.1 – Graphical Abstract of: J. A. Willms, H. Gleich, M. Schrempp, D. Menche, M. Engeser, *Chem. Eur. J.* **2018**, *24*, 2663–2668 (Ref. [3]).

4.2 Introduction

Electrospray mass spectrometry[6] is a powerful tool for gaining insight into the mechanisms of chemical reactions in solution. Even reactive intermediates at low concentrations may be detected, characterized, and probed for their reactivity, due to the low detection limits. Therefore, ESI-MS has been successfully utilized for mechanistic investigations of a broad range of organic and inorganic reactions.[14,28,29,75,146,150] A less commonly used extension of ESI-MS is online electrochemistry mass spectrometry (EC-MS), which has been used for metabolism research by simulating oxidative processes.[45,209,210] This technique allows the electrochemical treatment of analytes in solution immediately prior to their mass spectrometric analysis, and is thus considered a highly suitable method for studying redox reactions in the liquid phase.

Over the past few years, interest in the oxidative coupling of tertiary amines has been increasing.[211,212] This cross-dehydrogenative coupling[194] (CDC) involves the direct formation of a C–C bond from an activated C–H bond. THIQs have become a compound class of central interest in this research area, and broad ranges of both effective nucleophiles and catalyst/oxidant systems for their functionalization have been developed.[195] The combination of a Cu^{II} catalyst and air or oxygen as an inexpensive and sustainable oxidant for the activation of amines has been reported.[213–218]

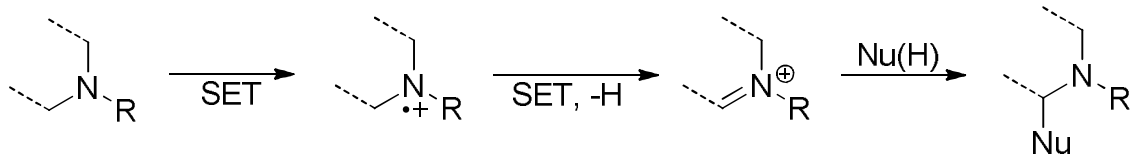

Scheme 4.1 – Mechanism of the oxidative coupling of amines *via* amine radical cation formation.[215]

The key mechanistic feature of the aerobic cross-coupling is the formation of an iminium intermediate[219] from the amine substrate by single-electron-transfer (SET) and proton-transfer steps (Scheme 4.1).[220–223] Under anaerobic conditions, a radical pathway for the coupling step has been assumed.[220,224–227]

A detailed understanding of the mechanism of CDC reactions[220,221,225] is a core requirement for synthetic improvements. We aimed to contribute to the ongoing

research activity with a mass spectrometric study. As a model system for the experiments, we chose the functionalization of *N*-phenyl-1,2,3,4-tetrahydroisoquinoline **11a** (*N*-Ph-THIQ) with diethylzinc, as developed by one of our group (Scheme 4.2).[208]

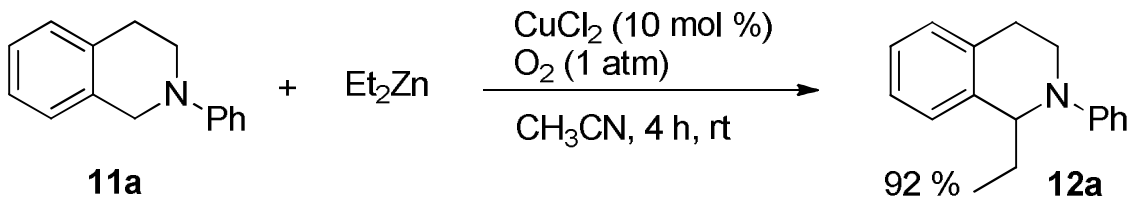

Scheme 4.2 – *Menche's* aerobic oxidative cross-coupling of THIQs with organozincreagents catalyzed by $CuCl_2$.[208]

Through our experiments, we also aimed to refine the proposed catalytic cycle (Scheme 4.3). We chose ESI-MS as a highly suitable method to monitor the copper(II)-catalyzed formation of the iminium species **14a**.

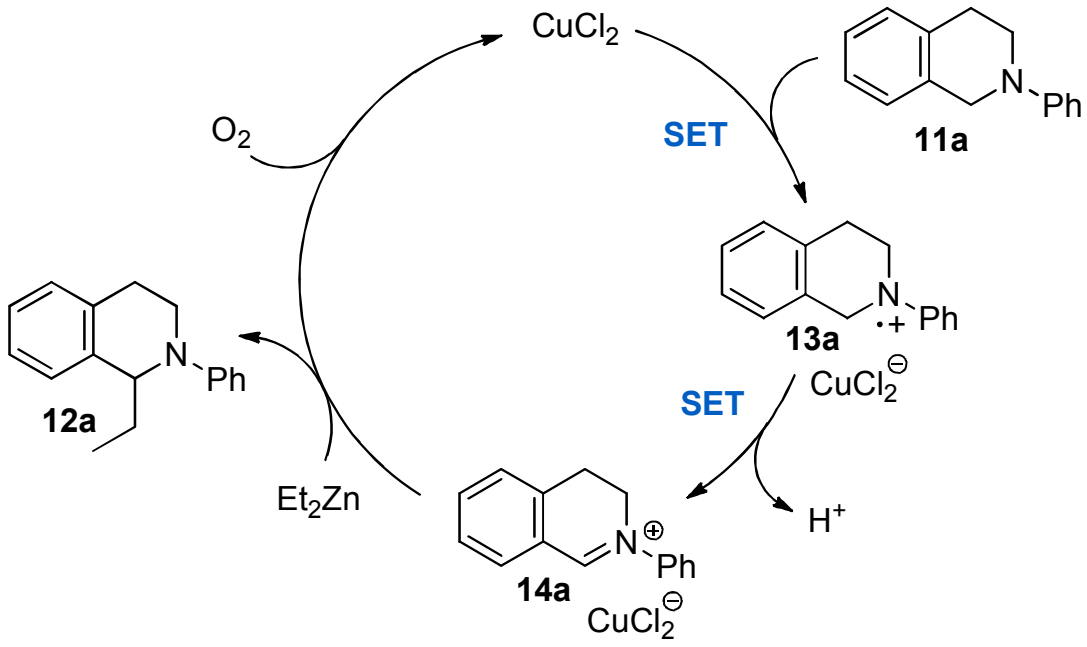

Scheme 4.3 – Proposed catalytic cycle of the CDC reaction between *N*-Ph-THIQ **11a** and diethylzinc according to *Menche* and co-workers.[208]

In addition, we coupled a commercial electrochemical flow cell to the ESI source of our mass spectrometer to obtain ESI mass spectra of electrochemically oxidized THIQ species. These data were compared with cyclic voltammograms of the same derivatives.

Thus, we present herein a promising technique to bridge the gap between mass spectrometry and cyclic voltammetry (CV) using EC-MS.

4.3 Results and Discussion

4.3.1 Formation of the iminium intermediate

We started our mass spectrometric investigations by focusing on the first half of the proposed catalytic cycle for the selected coupling reaction, that is, oxidative formation of the key intermediate iminium ion **14a** (Scheme 4.3). For this purpose, we analyzed solutions of the substrate **11a** and $CuCl_2$ in acetonitrile by ESI-MS. The oxidation process was followed by MS analysis of diluted samples of the reaction solution, which were taken at appropriate time intervals after mixing of the components (Figure 4.2A)).

The choice of diluent and the analyte concentration proved to be crucial in these experiments, because unintended oxidation of THIQ **11a** (to intermediate **14a**) during the ionization process had to be suppressed. The use of pure methanol or acetonitrile as spraying solvent and sample concentrations higher than 30 mM did not fulfill this requirement. Lower sample concentrations, a 1:1 mixture of dichloromethane and methanol as spraying solvent, in combination with mild electrospray conditions, delivered the best results.[I] Owing to the complexity of the ESI process, there are several possible explanations for these findings.[228] We assume that faster shrinkage of charged droplets due to faster solvent evaporation, lower ion concentration, and reduced dielectric constant of the mixture, decrease the oxidation during the ESI event. In any case, by using dichloromethane/methanol as spray solvent, it was possible to monitor the oxidation process by ESI-MS. A steady increase in the amount of iminium ion **14a** was detected over the course of 1 h.

[I]Note that in the upper MS spectrum of Figure 4.2A) a minor signal of iminium ion **14a** can be detected even though there is no copper(II) present in the solution.

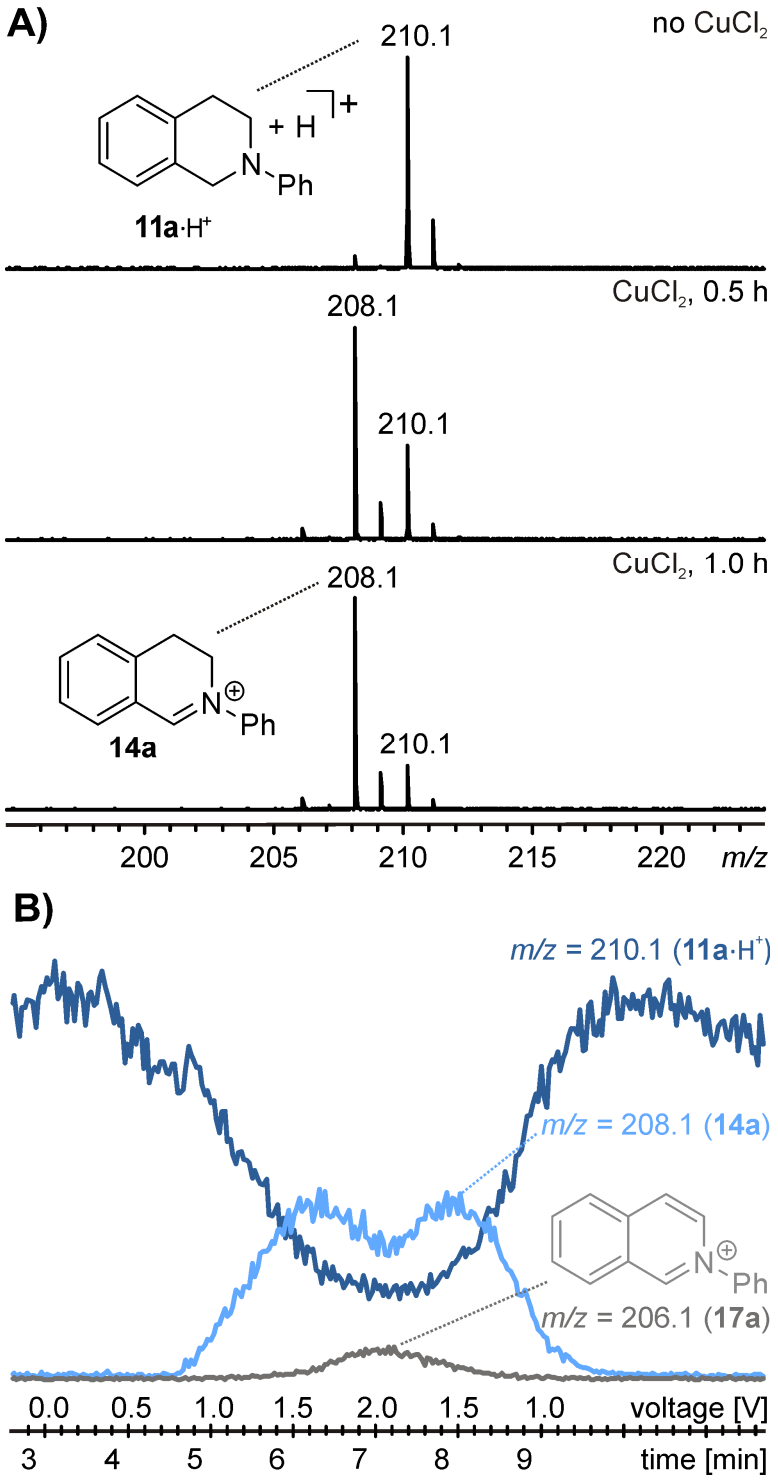

Figure 4.2 – A) ESI(+) mass spectra of samples from solutions in acetonitrile, under O_2 atmosphere (balloon), of *N*-Ph-THIQ **11a** [12.2 mm] (top), *N*-Ph-THIQ **11a** [12.2 mm] and 0.1 equiv. $CuCl_2$ [1.2 mm] after 0.5 h (center), and *N*-Ph-THIQ **11a** [12.2 mm] and 0.1 equiv. $CuCl_2$ [1.2 mm] after 1.0 h (bottom); samples diluted 1:400 with CH_2Cl_2/MeOH (1:1) for ESI; B) selected-ion chromatograms of *m/z* 210.1, 208.1, and 206.1 plotted against applied voltage to a solution of *N*-Ph-THIQ **11a** [3.2 mm] in CH_2Cl_2/MeOH (1:1) recorded with an EC-MS flow cell set-up; peak voltage 2.0 V, magic diamond (MD) electrode.

Whilst substrate **11a** and intermediate **14a** were easily detected, finding evidence for the aminium radical cationic intermediate **13a** proved to be much more difficult. With a nominal mass-to-charge ratio of *m*/*z* 209, its assumed MS signal overlaps with the ^{13}C signal of the isotope pattern of iminium ion **14a**. With higher mass spectrometric resolution, however, we succeeded in detecting aminium species **13a** at trace levels (Figure 4.3).

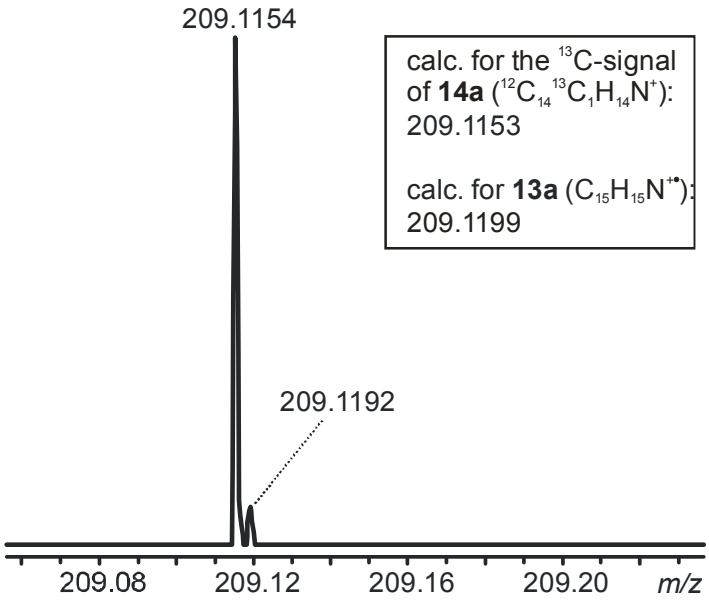

Figure 4.3 – Enlargement of an ESI(+) mass spectrum with the resolution set to R=100000 reveals the presence of **13a**. *N*-Ph-THIQ **11a** [0.313 mm] was mixed with $CuCl_2$ [0.125 mm] in acetonitrile. After 2.5 min, a sample was withdrawn, diluted 1:10 with CH_2Cl_2/MeOH (1:1), and analyzed with an Orbitrap XL mass spectrometer.

The involvement of a radical intermediate during the oxidation process was also indirectly verified by adding a radical scavenger to the reaction mixture, similar to previous examinations of other CDC reaction types.[225,229] Formation of iminium ion **14a** was considerably suppressed (although not fully eliminated) when 2,6-di-*tert*-butyl-4-methyl-phenol (BHT) was added to a solution of **11a** and $CuCl_2$, supporting the assumption of involvement of an aminium intermediate (Figure S4.3, Appendix S4). Furthermore, we obtained voltage-dependent chromatograms of pertinent ion abundances by electrochemically oxidizing compound **11a** immediately before MS analysis (Figure 4.2B)). For this purpose, a solution of the analyte was pumped through an electrochemical flow cell. The applied voltage in the EC cell was gradually increased and then decreased while continuously recording mass spectra.[230] Data processing was performed by plotting the relative intensity of the MS signals of interest against the

applied voltage. Figure 4.2B) shows an impressive example of how the peak due to substrate [**11a**+H]$^+$ (*m*/*z* 210.1) decreased as the applied potential was increased to around 0.7 V, with the peak of the oxidized form **14a** (*m*/*z* 208.1) appearing slightly thereafter. Furthermore, at higher voltages, a second oxidation to fully aromatic isoquinolinium species **17a** was detected to a minor extent (*m*/*z* 206.1). Due to the continuous analyte flow in the set-up, the original signal ratios are recovered once the applied voltage is subsequently reduced. In comparison to chemical oxidation employing $CuCl_2$ (Figure 4.2A)), the EC cell technique provides useful and consistent indications about voltage-dependent oxidative changes of **11a**, that is, visible changes of the MS signals.

4.3.2 Ethylation of the iminium intermediate with $ZnEt_2$

To investigate the actual C–C coupling step, the entire CDC reaction was conducted by mixing substrate **11a** and $CuCl_2$ in acetonitrile and adding a solution of $ZnEt_2$ in acetonitrile after 1.5 h. Mass spectra were obtained by ESI-MS analysis of diluted samples of the reaction mixture (Figure 4.4). Immediately after mixing pre-formed **14a** with $ZnEt_2$, the desired coupling product **12a** could be detected through a peak due to [**12a**+H]$^+$ (*m*/*z* 238.2) with significant intensity (Figure S4.4, Appendix S4). Thus, C–C coupling was significantly faster than iminium ion formation.

In addition, we found "off-cycle" species **15a** and **16a**, which *Klussmann* et al. have previously observed for CDC reactions with $CuCl_2 \cdot 2\,H_2O/O_2$ in MeOH.[221,225] The generation of hemiaminal **15a** can be attributed to contamination with traces of moisture during sample preparation. **16a** is formed when the reaction mixture is diluted with CH_2Cl_2/MeOH in preparation for ESI-MS analysis. Minor formation of the doubly-oxidized species **17a** has also been reported previously.[221] A small amount of the isoquinolinium species was therefore certain to be present in the reaction mixture. In fact, its MS signal (*m*/*z* 206.1) was rather pronounced and at this juncture we assume that the majority of **17a** detected in the mass spectrum in Figure 4.4 was generated during the ESI process. The same applies to the observation of Cu^I species rather than Cu^{II}. It is known from the literature that charge-transfer between the copper center and gas-phase solvent molecules, coupled with stabilization of Cu^I by acetonitrile ligands, leads to complete reduction of Cu^{II} derivatives in the course of the ESI process.[231–233]

No signals due to $ZnEt_2$ (or other zinc species) were detected under the measurement conditions applied for the reaction monitoring due to its reactivity towards methanol, its moisture sensitivity, and the insolubility of the degradation product ZnO.[234] However, optimized inert settings, acetonitrile as spray solvent, and significantly increased concentrations of $ZnEt_2$ made it possible to detect zinc-derived species (Figure S4.1 and Figure S4.2, Appendix S4).

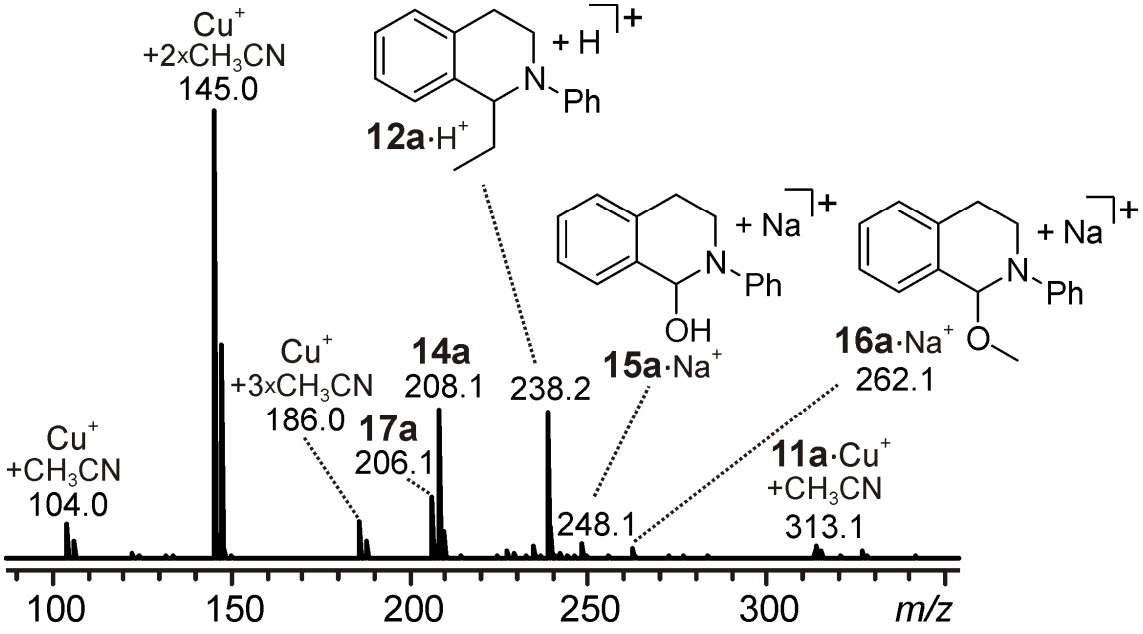

Figure 4.4 – ESI(+) mass spectrum of a CDC reaction mixture containing *N*-Ph-THIQ **11a** [50 mm] and diethylzinc [0.2m] with $CuCl_2$ [5 mm] as catalyst after 2.5 min; the sample was diluted 1:400 with CH_2Cl_2/MeOH (1:1) for ESI.

Reaction monitoring revealed that the formation of electrophile **14a** was rather slow, whereas the subsequent coupling with $ZnEt_2$ did not require multi-hour stirring, in contrast to our original procedure.[208] The reaction time may indeed be drastically shortened.

In order to ascertain whether the presence of $CuCl_2$ in the reaction mixture is not only necessary for oxidation, but also for the ethylation step, the CDC reaction was performed without any additives, that is, in the absence of Cu species. A solution of substrate **11a** in acetonitrile was subjected to electrochemical oxidation in the EC flow cell, and then mixed with $ZnEt_2$ in acetonitrile (Figure 4.5).

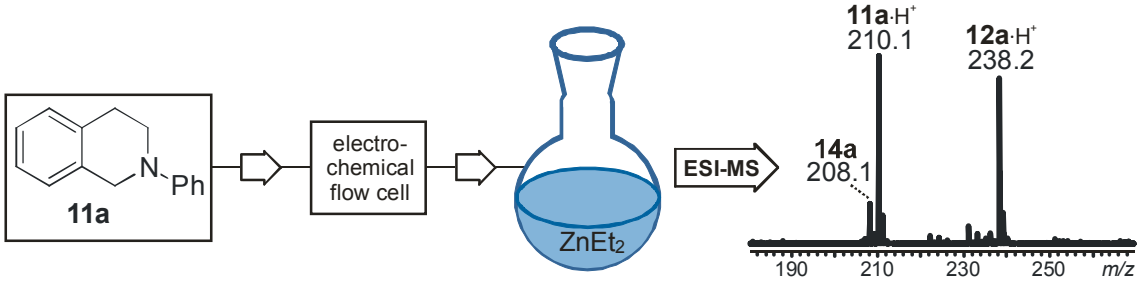

Figure 4.5 – Experimental set-up and resulting ESI mass spectrum for the electrochemically induced ($CuCl_2$-free) CDC reaction of **11a** with $ZnEt_2$.

Subsequent ESI-MS analysis of the reaction mixture proved formation of the CDC product **12a**. In addition, unreacted substrate **11a** was observed due to incomplete oxidation in the EC flow cell. This experiment demonstrated that neither $CuCl_2$ nor any other copper species is essential for the ethylation of iminium ion **14a**. The success of the CDC reaction is thus mainly determined by the stability of the formed dihydroisoquinolinium intermediate and by the oxidizing power of the catalyst, as shown in the following. These results also explain unsuccessful efforts by our group to exert asymmetric induction on the reaction through the use of chiral ligands bound to the copper center.

4.3.3 Substituent effects

We acquired the aforementioned EC cell voltage/ion intensity curves as well as cyclic voltammograms of several THIQ derivatives to test their applicability for the examined CDC reaction and to combine the results of both analytical techniques.

Figure 4.6 shows the results of EC/MS examinations as well as cyclic voltammograms of **11a** and the structurally closely related *N*-naphth-2-yl-THIQ **11b**.

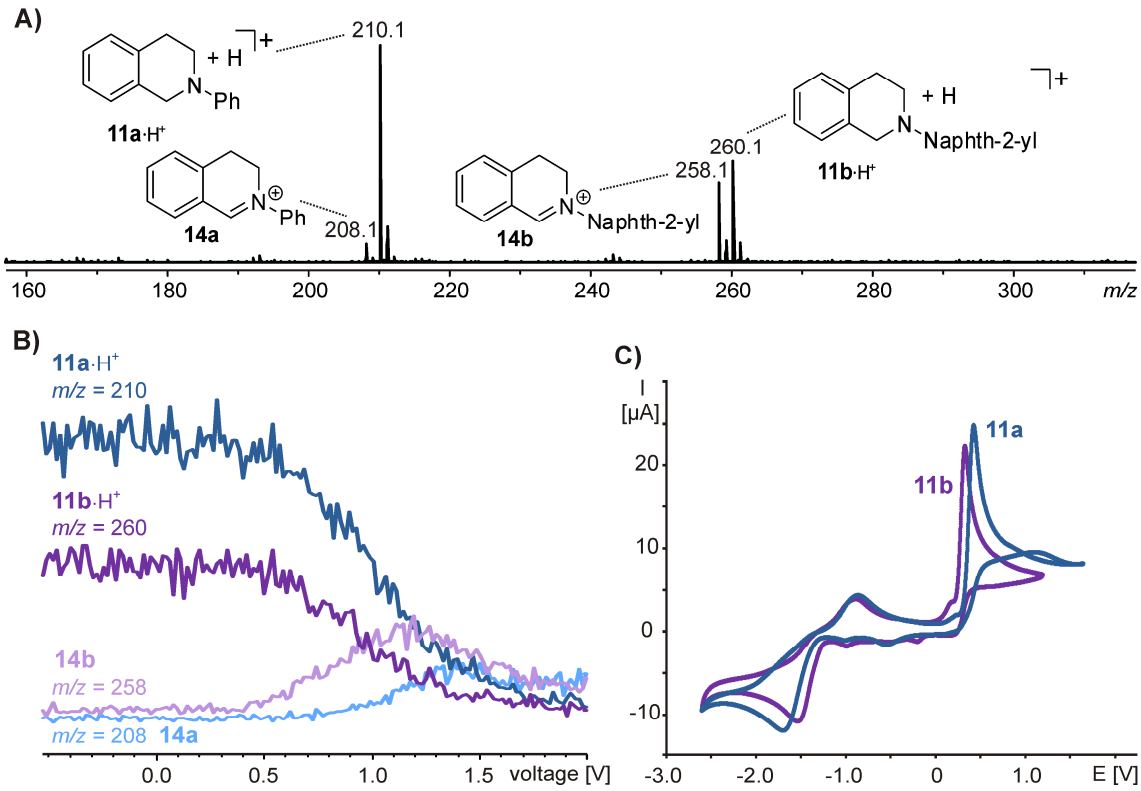

Figure 4.6 – A) ESI(+) mass spectrum of a mixture of *N*-Ph-THIQ **11a** [9.5 mm] and *N*-naphth-2-yl-THIQ **11b** [9.5 mm] in CH_2Cl_2/MeOH (1:1) after oxidation in an EC flow cell with 1.0 V; B) selected-ion chromatograms of *m/z* 260.1, 258.1, 210.1, and 208.1 plotted against applied voltage to a mixture of *N*-Ph-THIQ **11a** [9.5 mm] and *N*-naphth-2-yl-THIQ **11b** [9.5 mm] in CH_2Cl_2/MeOH (1:1); C) cyclic voltammograms of *N*-Ph-THIQ **11a** [5 mm] and *N*-naphth-2-yl-THIQ 1b [5 mm] in acetonitrile; E vs. Fc/Fc^+, Pt electrode, scan rate 50 mVs^{-1}.

Both methods reveal the similar oxidation behavior of the respective substrates, albeit with a slightly better oxidizability of **11b**. These methods both add insight for a more complete view of the process. Whilst cyclic voltammograms provide distinct values of the peak current of the oxidation process,[235–237] EC/MS observations give additional information about the nature of the oxidized species. Of course, this only applies if the electrochemically formed species are sufficiently stable under the experimental conditions.

Since removal of the *N*-substituent of the THIQ product is highly desirable in organic syntheses, we investigated THIQ derivatives with various protecting groups (Figure 4.7 and Figure S4.8–Figure S4.20, Appendix S4). The results demonstrate that, apart from *N*-naphth-2-yl-THIQ **11b**, all other examined substrates were less easily oxidized than **11a**. Thus, *N*-butyloxycarbonyl-THIQ **11d**, *N*-carbobenzyloxy-THIQ **11e**, and

N-tosyl-THIQ **11f** each show an oxidation peak approximately 1.5 V higher than that of **11a**. This precludes use of the inexpensive and favorable catalyst/oxidant system $CuCl_2/O_2$ as a suitable reagent for these derivatives.

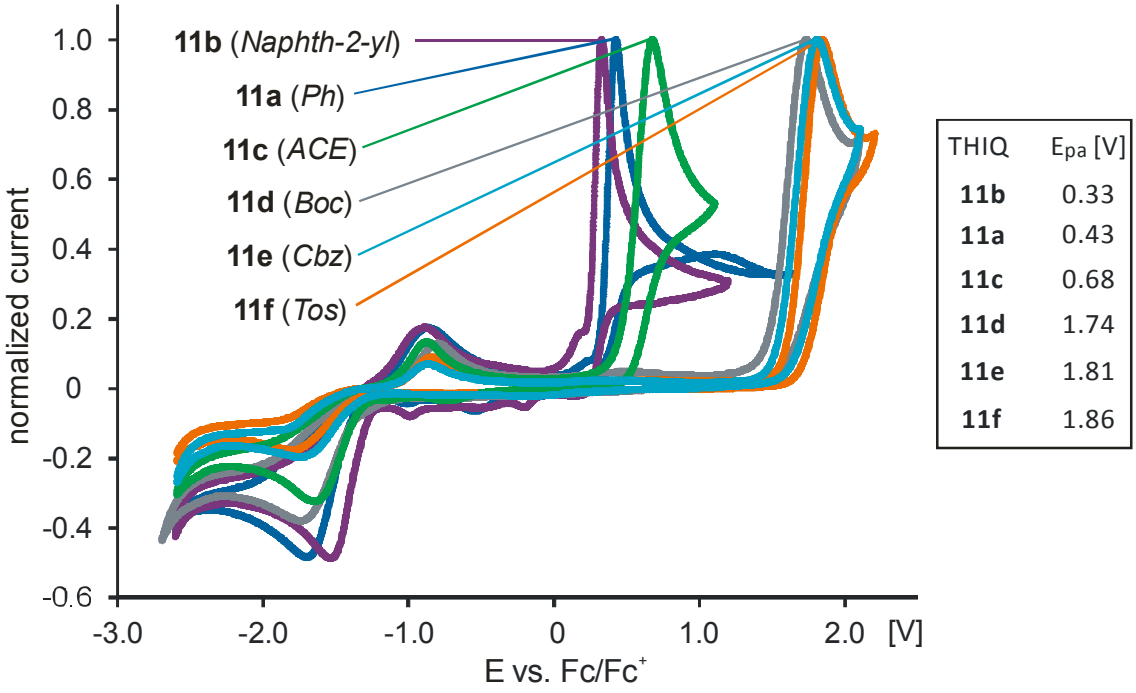

Figure 4.7 – Cyclic voltammograms of *N*-phenyl-THIQ **11a** [5 mm] (blue), *N*-naphth-2-yl-THIQ **11b** [5 mm] (purple), *N*-(2-acetoxyethyl)-THIQ **11c** [10 mm] (green), *N*-tert-butyloxycarbonyl-THIQ **11d** [10 mm] (gray), *N*-carbobenzyloxy-THIQ **11e** [10 mm] (light-blue), and *N*-tosyl-THIQ **11f** [10 mm] (orange) in acetonitrile; Pt electrode, scan rate 50 mVs^{-1}.

In accordance with these electrochemical findings, we also successfully detected the transient aminium radical cation species **13b** derived from *N*-naphth-2-yl-THIQ **11b** in the presence of $CuCl_2$ by high-resolution ESI-MS (Figure S4.5, Appendix S4), but could not find any indication of similar intermediates when treating the other mentioned THIQ derivatives **11c-f** with $CuCl_2$. For instance, MS investigation of a mixture of *N*-Boc-THIQ **11d** and $CuCl_2$ in acetonitrile indicated no reaction at all. A straightforward broadening of the scope of the reaction is probably possible by using a more effective oxidizing agent for less reactive substrates. Nevertheless, in the particular case of Boc-protected **11d**, several side reactions impede successful coupling reactions with this specific protective group. In EC/MS experiments, electrochemically formed iminium species **14d** reacts directly with the electrospray solvent (Figure S4.10, Appendix S4). This also explains why reported CDC reactions of **11d** have involved neat reaction conditions.[238,239] Among the tested THIQ derivatives bearing alternative

protective groups, the photolabile[240] *N*-(2-acetoxyethyl)-THIQ **11c** proved to be the most promising as a suitable surrogate with the $CuCl_2/O_2$ system, even though initial studies following our original reaction protocol[208] did not result in any conversion. However, an alternative oxidation strategy may facilitate successful ethylation.

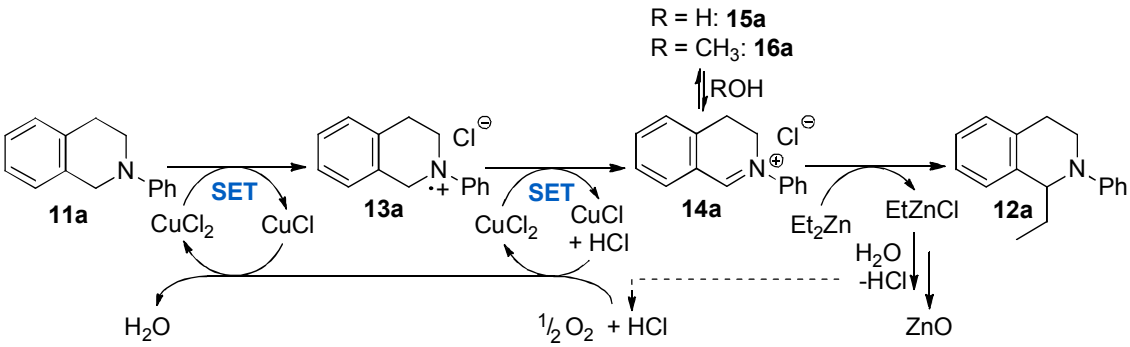

Scheme 4.4 – Refined mechanistic proposal for the CDC reaction with $ZnEt_2$ based on the results presented herein, which is in agreement with *Klussmann's* previous work.[223]

In line with these analyses, we suggest a refined mechanistic interpretation of the CDC reaction without any influence of copper species in the ethylation step, as shown in Scheme 4.4. Moreover, a strong dependence on the solvent has to be considered due to the solubility of the copper(II) salt and stabilizing effects on the radical cationic (**13a**) and cationic (**14a**) intermediates.

4.4 Conclusion

Thorough investigations of the aerobic oxidative cross-coupling of THIQs with organozinc reagents catalyzed by $CuCl_2$ have provided mass spectrometric insight into the reaction process. The transient aminium species **13a** could be detected, and the key intermediate iminium ion **14a** was observed after chemical and/or electrochemical oxidation. Voltage-dependent ion intensity curves derived from EC-MS experiments on a series of derivatives have provided helpful information about substituent effects and oxidation products associated with cyclic voltammetric oxidation peaks. Moreover, the ethylated coupling product has also been synthesized under Cu-free conditions by

electrochemical generation of the iminium intermediate before treatment with diethylzinc. This experiment illustrates the role of $CuCl_2$. Its presence is not essential in the actual coupling reaction.

The results provide a rational explanation for limitations of the ethylation reaction. The critical step is the formation of iminium intermediate **14**. The oxidation potential of $CuCl_2$ is insufficient to oxidize THIQ substrates without *N*-aryl substituents. More efficient oxidants should readily allow an expansion of the substrate scope. Furthermore, the technique of linking mass spectrometry with cyclic voltammetry is a good example of a rational alternative to synthetic screening methods for reaction optimization.

4.5 Experimental section

4.5.1 Mass spectrometry

ESI mass spectra were recorded from solutions (3 μM-25 mM) in acetonitrile or CH_2Cl_2/MeOH (1:1) on a commercial quadrupole/time-of-flight (Q/TOF) mass spectrometer (Bruker micrOTOF-Q) equipped with an Apollo ESI source. In individual cases, a commercial Orbitrap mass spectrometer (Thermo Fisher Scientific LTQ-Orbitrap XL) was utilized for higher mass resolution. Nitrogen was used as spraying and nebulizing gas. Signal assignments are based on selected representative experiments with careful mass calibration. Voltage/ion intensity curves were obtained with a commercial electrochemical flow cell [Antec Scientific ROXY potentiostat and thin-layer ReactorCell (cell volume: 0.7 μL) with a magic diamond (MD) working electrode (Ø: 8 mm), an HyREF reference electrode, and a 50 μm spacer]. This EC cell was directly coupled to the ESI source of the Q/TOF mass spectrometer. Peak voltage (2.0/3.5 V) and step size (0.1 V per 0.2 min) were adjusted using the corresponding software (Dialogue, Antec Scientific). Analyte solutions (3-30 μM) were passed into the cell through PEEK tubing (1.6 mm OD × 0.13 mm ID) at a flow rate of 300 μL h^{-1} using a syringe pump (Cole Parmer) and a 250 μL glass syringe (Hamilton).

4.5.2 Cyclic voltammetry

Cyclic voltammograms were recorded from solutions of the analyte (5-10 mM) and nBu$_4$N$^+$PF$_6^-$ (0.1 M) in acetonitrile with a three-electrode electrochemical cell (Gamry Interface 1000 potentiostat) with an Ag/AgNO$_3$ reference electrode (0.01 M with 0.1 M nBu$_4$N$^+$PF$_6^-$ in acetonitrile), a platinum counter electrode, and a platinum working electrode. CV curves were recorded at a potential scan rate of 50 mV s^{-1}. Ferrocene (Fc) was added as an internal reference after every experiment, and all of the measurements were referenced relative to the $E_{1/2}$ value of the Fc/Fc$^+$ couple, estimated as ½ (E_{pa}+E_{pc}), where E_{pa}=anode peak potential and E_{pc}=cathode peak potential. The cyclic voltammogram of ferrocene recorded with our experimental set-up is provided (Figure S4.14, Appendix S4).

4.6 Acknowledgements

Financial support from the Deutsche Forschungsgemeinschaft (SFB 813) is gratefully acknowledged.

5 Concluding remarks and outlook

In this thesis charge-tagging, mixing tee infusion, IRMPD and electrochemistry/MS were successfully used as sophisticated modern mass spectrometric strategies for the mechanistic investigation of an organocatalytic aldol reaction and an oxidative coupling reaction by means of ESI-MS.

The extensive ESI-MS studies on *Jørgensen's*[112] inverse aldol reaction and the reaction of catalyst **1** with acetone presented in Chapters 2 and 3 reveal the predominant presence of oxazolidinone derivatives among catalyst-based species in an electrosprayed reaction mixture. This fundamental result is consistent with condensed-phase studies of enamine-catalyzed reactions.[92,141,182] This work presents a unique structural examination of such L-proline derived intermediates in the gas phase using mass spectrometry.

The field of application of the charge-tagged catalyst **1** in reaction investigations with ESI-MS can be extended in many ways. In a further study on a Diels-Alder reaction with inverse electron demand, we have already been successful in detecting and analyzing three relevant intermediate species.[4] During investigations of the same reaction using either a charge-tagged substrate or no tagging strategy at all, only two or less of the three mentioned species were detected. Also, a certain reduction of the performance of catalyst **1** compared to L-proline was observed. The potential of **1** may therefore be summarized as valuable but conditionally limited. A thorough screening of various organocatalytic reactions should provide extremely useful results in form of a mass spectrometric isolation of various intermediates.

As already discussed in Subsection 3.5, an outstanding advantage in ESI-MS investigations of intermediates based on **1** is their unaltered chemical nature. Certainly, the bulky 1-ethylpyridinium-4-phenoxy unit must influence the catalyst properties and its reaction behavior in one way or another. Nevertheless, if the formation and detection of intermediary species of interest is successful, they can be investigated in the gas

phase without their primary structural properties being affected by protonation, oxidation or other ESI influenced changes – an advantage which has already been exploited in the MS study in Chapter 3 as well as further investigations[70] and which gives rise to additional research projects. The direct initiation of reactions with intermediates in the cell of an FT-ICR mass spectrometer by pulsing a second substrate offers an excellent opportunity for comparative kinetic measurements with isolated intermediate species. For example, the gas-phase reactivity of oxazolidinone species could be investigated to elucidate their role in the catalytic cycle of enamine catalysis.

The study of *Menche's*[208] aerobic oxidative cross-coupling of THIQs with diethylzinc catalyzed by $CuCl_2$, which is presented in Chapter 4, allows a refined postulation of the reaction mechanism. In addition to several successful experiments to follow the reaction progress using ESI-MS, even the transient aminium species **13a** and **13b** could be detected. The results of ESI-MS, EC/MS and CV measurements consistently revealed the strong influence of the *N*-substituents of the different THIQ substrates on their oxidation stability against $CuCl_2$.

The profitable use of the EC flow cell provided an electrochemical counterpart to the results obtained from investigations on the $CuCl_2$ catalyzed formation of iminium key intermediate **14a**. The results also show that EC/MS is not restricted for the metabolism analyses of drugs,[45–47] but is also suitable for the clarification of questions regarding to oxidative transformations in solution in organic syntheses.

Semi-preparative electrochemically induced formation of the coupling product by the EC flow cell provided excellent evidence that $CuCl_2$ is not essential for the actual coupling step of the CDC reaction (Figure 4.5). This setup is not recommended for experimental applications beyond such a proof of principle. For preparative purposes the associated low conversion and low flow rates are unfavorable.

The recording of voltage-dependent ion-intensity curves[52–54] sometimes is a certain experimental challenge because a stable electrospray is required for several minutes. However, they also offer an excellent method for the observation of oxidative and reductive species. Overall, flow cell assisted EC/MS is a suitable alternative to synthetic screening approaches. The scope for further research projects on redox processes is not limited to a specific substrate type. Furthermore, EC/MS can be considered as a link

between mass spectrometry and cyclovoltammetry. It can also serve as highly suitable tool for the interpretation of cyclic voltammograms.

The mass spectrometric and electrochemical methods used in this work will yield useful results in countless other experiments. Hopefully, in some cases, this work can provide a little help in the investigation of further, unknown processes.

6 References

[1] J. A. Willms, R. Beel, M. L. Schmidt, C. Mundt, M. Engeser, *Beilstein J. Org. Chem.* **2014**, *10*, 2027–2037.

[2] J. A. Willms, J. Vidic, J. Barthelmes, V. Steinmetz, T. Bredow, P. Maître, M. Engeser, *Phys. Chem. Chem. Phys.* **2019**; DOI: 10.1039/c8cp04905j.

[3] J. A. Willms, H. Gleich, M. Schrempp, D. Menche, M. Engeser, *Chem. Eur. J.* **2018**, *24*, 2663–2668.

[4] A. Schnell, J. A. Willms, S. Nozinovic, M. Engeser, *Beilstein J. Org. Chem.* **2019**, *15*, 30–43.

[5] J. H. Gross (Ed.), *Mass Spectrometry: a Textbook*; Springer: Cham, 2017.

[6] R. B. Cole (Ed.), *Electrospray Ionization Mass Spectrometry*; Wiley: New York, 1997.

[7] M. Dole, L. L. Mack, R. L. Hines, R. C. Mobley, L. D. Ferguson, M. B. Alice, *J. Chem. Phys.* **1968**, *49*, 2240–2249.

[8] M. Yamashita, J. B. Fenn, *J. Phys. Chem.* **1984**, *88*, 4451–4459.

[9] M. Yamashita, J. B. Fenn, *J. Phys. Chem.* **1984**, *88*, 4671–4675.

[10] C. M. Whitehouse, R. N. Dreyer, M. Yamashita, J. B. Fenn, *Anal. Chem.* **1985**, *57*, 675–679.

[11] J. B. Fenn, M. Mann, C. K. Meng, S. F. Wong, C. M. Whithouse, *Science* **1989**, *246*, 64–71.

[12] J. B. Fenn, *Angew. Chem.* **2003**, *115*, 3999–4024; *Angew. Chem. Int. Ed.* **2003**, *42*, 3871–3894.

[13] P. Nemes, I. Marginean, A. Vertes, *Anal. Chem.* **2007**, *79*, 3105–3116.

[14] D. Schröder, *Acc. Chem. Res.* **2012**, *45*, 1521–1532.

[15] H. Awad, M. M. Khamis, A. El-Aneed, *Appl. Spectrosc. Rev.* **2014**, *50*, 158–175.

[16] P. Kebarle, L. Tang, *Anal. Chem.* **1993**, *65*, 972A–986A.

[17] M. S. Wilm, M. Mann, *Int. J. Mass Spectrom. Ion Process.* **1994**, *136*, 167–180.

[18] Rayleigh, *The London, Edinburgh and Dublin Philosophical Magazine and Journal of Science* **1882**, *14*, 184–186.

[19] R. L. Grimm, J. L. Beauchamp, *J. Phys. Chem. B* **2005**, *109*, 8244–8250.

[20] R. B. Cole, *J. Mass Spectrom.* **2000**, *35*, 763–772.

[21] J. V. Iribarne, B. A. Thomson, *J. Chem. Phys.* **1976**, *64*, 2287–2294.

[22] P. Kebarle, M. Peschke, *Anal. Chim. Acta* **2000**, *406*, 11–35.

[23] N. B. Cech, C. G. Enke, *Mass Spectrom. Rev.* **2001**, *20*, 362–387.

[24] R. Juraschek, F. W. Röllgen, *Int. J. Mass Spectrom.* **1998**, *177*, 1–15.

[25] L. de Juan, J.F. de La Mora, *J. Colloid Interface Sci.* **1997**, *186*, 280–293.

[26] J. Martin E. Quirke, Christopher L. Adams, G. J. Van Berkel, *Anal. Chem.* **1994**, *66*, 1302–1315.

[27] N. B. Cech, J. R. Krone, C. G. Enke, *Rapid Commun. Mass Spectrom.* **2001**, *15*, 1040–1044.

[28] M. N. Eberlin, *Eur. J. Mass Spectrom.* **2007**, *13*, 19–28.

[29] K. L. Vikse, Z. Ahmadi, C. C. Manning, D. A. Harrington, J. S. McIndoe, *Angew. Chem.* **2011**, *123*, 8454–8456; *Angew. Chem. Int. Ed.* **2011**, *50*, 8304–8306.

[30] C. Adlhart, P. Chen, *Helv. Chim. Acta* **2000**, *83*, 2192–2196.

[31] R. L. Smith, H. I. Kenttämaa, *J. Am. Chem. Soc.* **1995**, *117*, 1393–1396.

[32] R. L. Woodin, D. S. Bomse, J. L. Beauchamp, *J. Am. Chem. Soc.* **1978**, *100*, 3248–3250.

[33] J. Oomens, B. G. Sartakov, G. Meijer, G. von Helden, *Int. J. Mass Spectrom.* **2006**, *254*, 1–19.

[34] L. Mac Aleese, P. Maître, *Mass Spectrom. Rev.* **2007**, *26*, 583–605.

[35] J. R. Eyler, *Mass Spectrom. Rev.* **2009**, *28*, 448–467.

[36] N. C. Polfer, *Chem. Soc. Rev.* **2011**, *40*, 2211–2221.

[37] A. G. Marshall, C. L. Hendrickson, G. S. Jackson, *Mass Spectrom. Rev.* **1998**, *17*, 1–35.

[38] R. E. March, *J. Mass Spectrom.* **1997**, *32*, 351–369.

[39] R. Prazeres, J. M. Berset, R. Chaput, F. Glotin, D. A. Jaroszynski, J. M. Ortega, *Nucl. Instrum. Methods Phys. Res.* **1994**, *89*, 54–59.

[40] D. Oepts, A. F. G. van der Meer, P. W. van Amersfoort, *Infrared Phys. Technol.* **1995**, *36*, 297–308.

[41] W. Schöllkopf, S. Gewinner, H. Junkes, A. Paarmann, G. von Helden, H. Bluem, A. M. M. Todd, *Proc. SPIE* **2015**, *9512*, 95121L.

[42] E. R. Grant, P. A. Schulz, A. S. Sudbo, Y. R. Shen, Y. T. Lee, *Phys. Rev. Lett.* **1978**, *40*, 115-118.

[43] J. P. Merrick, D. Moran, L. Radom, *J. Phys. Chem. A* **2007**, *111*, 11683–11700.

[44] M. D. Halls, J. Velkovski, H. B. Schlegel, *Theor. Chem. Acc.* **2001**, *105*, 413–421.

[45] a) U. Karst, *Angew. Chem.* **2004**, *43*, 2476–2478; *Angew. Chem. Int. Ed.* **2004**, *43*, 2476–2478; b) S. Jahn, U. Karst, *J. Chromatogr. A* **2012**, *1259*, 16–49.

[46] H. Faber, M. Vogel, U. Karst, *Anal. Chim. Acta* **2014**, *834*, 9–21.

[47] J. Gun, S. Bharathi, V. Gutkin, D. Rizkov, A. Voloshenko, R. Shelkov, S. Sladkevich, N. Kyi, M. Rona, Y. Wolanov, M. Koch, S. Mizrahi, P. V. Pridkhochenko, A. Modestov, O. Lev, *Isr. J. Chem.* **2010**, *50*, 360–373.

[48] F. Zhou, G. J. van Berkel, *Anal. Chem.* **1995**, *67*, 3643–3649.

[49] X. Xu, W. Lu, R. B. Cole, *Anal. Chem.* **1996**, *68*, 4244–4253.

[50] W. Lohmann, A. Baumann, U. Karst, *LC GC Eur.* **2010**, *23*, 1–7.

[51] M. Prudent, H. H. Girault, *Analyst* **2009**, *134*, 2189–2203.

[52] J. Gun, A. Modestov, O. Lev, R. Poli, *Eur. J. Inorg. Chem.* **2003**, 2264–2272.

[53] J. Gun, A. Modestov, O. Lev, D. Saurenz, M. A. Vorotyntsev, R. Poli, *Eur. J. Inorg. Chem.* **2003**, 482–492.

[54] T. Hoffmann, D. Hofmann, E. Klumpp, S. Küppers, *Anal. Bioanal. Chem.* **2011**, *399*, 1859–1868.

[55] P. I. Dalko, L. Moisan, *Angew. Chem.* **2004**, *116*, 5248–5286; *Angew. Chem. Int. Ed.* **2004**, *43*, 5138–5175.

[56] D. W. C. MacMillan, *Nature* **2008**, *455*, 304–308.

[57] S. Bertelsen, K. A. Jørgensen, *Chem. Soc. Rev.* **2009**, *38*, 2178–2189.

[58] B. List (Ed.), *Asymmetric Organocatalysis*; Springer: Berlin, Heidelberg, 2010.

[59] U. Eder, G. Sauer, R. Wiechert, *Angew. Chem.* **1971**, *83*, 492–493; *Angew. Chem. Int. Ed.* **1971**, *10*, 496-497.

[60] Z. G. Hajos, D. R. Parrish, *J. Org. Chem.* **1974**, *39*, 1615–1621.

[61] B. List, R. A. Lerner, C. F. Barbas III, *J. Am. Chem. Soc.* **2000**, *122*, 2395–2396.

[62] P. Hickmott, *Tetrahedron* **1982**, *38*, 1975–2050.

[63] C. Marquez, J. O. Metzger, *Chem. Commun.* **2006**, 1539–1541.

[64] C. Allemann, R. Gordillo, F. R. Clemente, P. H.-Y. Cheong, K. N. Houk, *Acc. Chem. Res.* **2004**, *37*, 558–569.

[65] B. List, L. Hoang, H. J. Martin, *J. Proc. Natl. Acad. Sci. U. S. A.* **2004**, *101*, 5839–5842.

[66] R. Beel, *Diploma thesis*, Rheinische Friedrich-Wilhelms-Universität, Bonn, 2010.

[67] C. Mundt, *Diploma thesis*, Rheinische Friedrich-Wilhelms-Universität, Bonn, 2012.

[68] D. Schunkert, *Bachelor thesis*, Rheinische Friedrich-Wilhelms-Universität, Bonn, 2012.

[69] K. H. Schuppener, *Bachelor thesis*, Rheinische Friedrich-Wilhelms-Universität, Bonn, 2016.

[70] J. Barthelmes, *Bachelor thesis*, Rheinische Friedrich-Wilhelms-Universität, Bonn, 2017.

[71] J. A. Willms, *Diploma thesis*, Rheinische Friedrich-Wilhelms-Universität, Bonn, 2013.

[72] J. B. Fenn, *Angew. Chem.* **2003**, *115*, 3999–4024; *Angew. Chem. Int. Ed.* **2003**, *42*, 3871–3894.

[73] P. Chen, *Angew. Chem.* **2003**, *115*, 2938–2954; *Angew. Chem. Int. Ed.* **2003**, *25*, 2832–2847.

[74] L. S. Santos, L. Knaack, J. O. Metzger, *Int. J. Mass Spectrom.* **2005**, *246*, 84–104.

[75] D. A. Plattner, *Top. Curr. Chem.* **2003**, *225*, 153–203.

[76] F. F. D. Oliveira, M. R. dos Santos, P. M. Lalli, E. M. Schmidt, P. Bakuzis, A. A. M. Lapis, A. L. Monteiro, M. N. Eberlin, B. A. D. Neto, *J. Org. Chem.* **2011**, *76*, 10140–10147.

[77] K. L. Vikse, M. A. Henderson, A. G. Oliver, J. S. McIndoe, *Chem. Commun.* **2010**, *46*, 7412–7414.

[78] M. A. Schade, J. E. Fleckenstein, P. Knochel, K. Koszinowski, *J. Org. Chem.* **2010**, *75*, 6848–6857.

[79] E. Thiery, C. Chevrin, J. Le Bras, D. Harakat, J. Muzart, *J. Org. Chem.* **2007**, *72*, 1859–1862.

[80] L. S. Santos, G. B. Rosso, R. A. Pilli, M. N. Eberlin, *J. Org. Chem.* **2007**, *72*, 5809–5812.

[81] P.-A. Enquist, P. Nilsson, P. Sjöberg, M. Larhed, *J. Org. Chem.* **2006**, *71*, 8779–8786.

[82] A. A. Sabino, A. H. L. Machado, C. R. D. Correia, M. N. Eberlin, *Angew. Chem.* **2004**, *116*, 2568–2572; *Angew. Chem. Int. Ed.* **2004**, *43*, 2514–2518.

[83] A. O. Aliprantis, J. W. Canary, *J. Am. Chem. Soc.* **1994**, *116*, 6985–6986.

[84] A. Teichert, A. Pfaltz, *Angew. Chem.* **2008**, *120*, 3408–3410; *Angew. Chem. Int. Ed.* **2008**, *47*, 3363–3366.

[85] S. Fürmeier, J. O. Metzger, *J. Am. Chem. Soc.* **2004**, *126*, 14485–14492.

[86] D. M. Chisholm, J. S. McIndoe, *Dalton Trans.* **2008**, 3933–3945.

[87] A. Berkessel, H. Gröger (Eds.), *Asymmetric Organocatalysis*; Wiley-VCH: Weinheim, 2005.

[88] P. I. Dalko (Ed.), *Enantioselective Organocatalysis*; Wiley-VCH: Weinheim, 2007.

[89] P. Melchiorre, M. Marigo, A. Carlone, G. Bartoli, *Angew. Chem.* **2008**, *120*, 6232–6265; *Angew. Chem. Int. Ed.* **2008**, *47*, 6138–6171.

[90] S. Mukherjee, J. W. Yang, S. Hoffmann, B. List, *Chem. Rev.* **2007**, *107*, 5471–5569.

[91] W. Notz, F. Tanaka, C. F. Barbas III., *Acc. Chem. Res.* **2004**, *37*, 580–591.

[92] M. B. Schmid, K. Zeitler, R. M. Gschwind, *Angew. Chem.* **2010**, *122*, 5117–5123; *Angew. Chem. Int. Ed.* **2010**, *49*, 4997–5003.

[93] P. Dinér, A. Kjærsgaard, M. A. Lie, K. A. Jørgensen, *Chem. Eur. J.* **2008**, *14*, 122–127.

[94] N. Zotova, A. Franzke, A. Armstrong, D. G. Blackmond, *J. Am. Chem. Soc.* **2007**, *129*, 15100–15101.

[95] S. P. Mathew, M. Klussmann, H. Iwamura, D. H. Wells, A. Armstrong, D. G. Blackmond, *Chem. Commun.* **2006**, 4291–4293.

[96] H. Iwamura, D. H. Wells, S. P. Mathew, M. Klussmann, A. Armstrong, D. G. Blackmond, *J. Am. Chem. Soc.* **2004**, *126*, 16312–16313.

[97] L. Hoang, S. Bahmanyar, K. N. Houk, B. List, *J. Am. Chem. Soc.* **2003**, *125*, 16–17.

[98] F. Bächle, J. Duschmalé, C. Ebner, A. Pfaltz, H. Wennemers, *Angew. Chem.* **2013**, *125*, 12851–12855; *Angew. Chem. Int. Ed.* **2013**, *52*, 12619–12623.

[99] T. Regiani, V. G. Santos, M. N. Godoi, B. G. Vaz, M. N. Eberlin, F. Coelho, *Chem. Commun.* **2011**, *47*, 6593–6595.

[100] R. Beel, S. Kobialka, M. L. Schmidt, M. Engeser, *Chem. Commun.* **2011**, *47*, 3293–3295.

[101] M. W. Alachraf, P. P. Handayani, M. R. M. Hüttl, C. Grondal, D. Enders, W. Schrader, *Org. Biomol. Chem.* **2011**, *9*, 1047–1053.

[102] O. V. Maltsev, A. O. Chizhov, S. G. Zlotin, *Chem. Eur. J.* **2011**, *17*, 6109–6117.

[103] G. W. Amarante, M. Benassi, H. M. S. Milagre, A. A. C. Braga, F. Maseras, M. N. Eberlin, F. Coelho, *Chem. Eur. J.* **2009**, *15*, 12460–12469.

[104] W. Schrader, P. P. Handayani, J. Zhou, B. List, *Angew. Chem.* **2009**, *121*, 1491–1494; *Angew. Chem. Int. Ed.* **2009**, *48*, 1463–1466.

[105] W. Schrader, P. P. Handayani, C. Burstein, F. Glorius, *Chem. Commun.* **2007**, 716–718.

[106] C. D. F. Milagre, H. M. S. Milagre, L. S. Santos, M. L. A. Lopes, P. J. S. Moran, M. N. Eberlin, J. A. R. Rodrigues, *J. Mass Spectrom.* **2007**, *42*, 1287–1293.

[107] C. A. Marquez, F. Fabbretti, J. O. Metzger, *Angew. Chem.* **2007**, *119*, 7040–7042; *Angew. Chem. Int. Ed.* **2007**, *46*, 6915–6917.

[108] L. S. Santos, C. H. Pavam, W. P. Almeida, F. Coelho, M. N. Eberlin, *Angew. Chem.* **2004**, *116*, 4430–4433; *Angew. Chem. Int. Ed.* **2004**, *43*, 4330–4333.

[109] T. D. Machajewski, C.-H. Wong, *Angew. Chem.* **2000**, *112*, 1406–1430; *Angew. Chem. Int. Ed.* **2000**, *39*, 1352–1375.

[110] D. Seebach, A. K. Beck, D. M. Badine, M. Limbach, A. Eschenmoser, A. M. Treasurywala, R. Hobi, W. Prikoszovich, B. Linder, *Helv. Chim. Acta* **2007**, *90*, 425–471.

[111] A. Bottoni, M. Lombardo, G. P. Miscione, E. Montroni, A. Quintavalla, C. Trombini, *ChemCatChem* **2013**, *5*, 2913–2924.

[112] A. Bøgevig, N. Kumaragurubaran, K. A. Jørgensen, *Chem. Commun.* **2002**, 620–621.

[113] V. Diemer, H. Chaumeil, A. Defoin, A. Fort, A. Boeglin, C. Carré, *Eur. J. Org. Chem.* **2006**, 2727–2738.

[114] W. Gu, X. She, X. Pan, T.-K. Yang, *Tetrahedron: Asymmetry* **1998**, *9*, 1377–1380.

[115] P. Chabaud, G. Pèpe, J. Courcambeck, M. Camplo, *Tetrahedron* **2005**, *61*, 3725–3731.

[116] K.-i. Tanaka, H. Sawanishi, *Tetrahedron: Asymmetry* **1998**, *9*, 71–77.

[117] R. Cotton, A. N. C. Johnstone, M. North, *Tetrahedron Lett.* **1994**, *35*, 8859–8862.

[118] J. Pícha, V. Vaněk, M. Buděšínský, J. Mládková, T. A. Garrow, J. Jiráček, *Eur. J. Med. Chem.* **2013**, *65*, 256–275.

[119] R. H. Blessing, *Acta Crystallogr., Sect. A* **1995**, *51*, 33–38.

[120] G. M. Sheldrick SHELXS97 and SHELXL97, *University of Göttingen, Germany,* **1997**.

[121] B. List, *Chem. Rev.* **2007**, *107*, 5413–5415.

[122] G. Guillena, C. Nájera, D. J. Ramón, *Tetrahedron: Asymmetry* **2007**, *18*, 2249–2293.

[123] V. Bisai, A. Bisai, V. K. Singh, *Tetrahedron* **2012**, *68*, 4541–4580.

[124] J. M. M. Verkade, L. J. C. van Hemert, P. J. L. M. Quaedflieg, F. P. J. T. Rutjes, *Chem. Soc. Rev.* **2008**, *37*, 29–41.

[125] J. L. Vicario, D. Badia, L. Carrillo, *Synthesis* **2007**, 2065–2092.

[126] G. Guillena, D. J. Ramón, M. Yus, *Tetrahedron: Asymmetry* **2007**, *18*, 693–700.

[127] D. Enders, C. Grondal, M. R. M. Hüttl, *Angew. Chem.* **2007**, *119*, 1590–1601; *Angew. Chem. Int. Ed.* **2007**, *46*, 1570–1581.

[128] C. M. R. Volla, I. Atodiresei, M. Rueping, *Chem. Rev.* **2014**, *114*, 2390–2431.

[129] A. E. Allen, D. W. C. MacMillan, *Chem. Sci.* **2012**, *3*, 633–658.

[130] M. Neumann, S. Füldner, B. König, K. Zeitler, *Angew. Chem.* **2011**, *123*, 981–985; *Angew. Chem. Int. Ed.* **2011**, *50*, 951–954.

[131] C. C. J. Loh, D. Enders, *Chem. Eur. J.* **2012**, *18*, 10212–10225.

[132] Y. Deng, S. Kumar, H. Wang, *Chem. Commun.* **2014**, *50*, 4272–4284.

[133] A. Gualandi, L. Mengozzi, C. M. Wilson, P. G. Cozzi, *Chem. Asian J.* **2014**, *9*, 984–995.

[134] G. Lelais, D. W. C. MacMillan, *Aldrichimica Acta* **2006**, *39*, 79–87.

[135] K. L. Jensen, G. Dickmeiss, H. Jiang, L. Albrecht, K. A. Jørgensen, *Acc. Chem. Res.* **2012**, *45*, 248–264.

[136] M. Gruttadauria, F. Giacalone, R. Noto, *Chem. Soc. Rev.* **2008**, *37*, 1666–1688.

[137] S. Bahmanyar, K. N. Houk, H. J. Martin, B. List, *J. Am. Chem. Soc.* **2003**, *125*, 2475–2479.

[138] A. K. Sharma, R. B. Sunoj, *Angew. Chem.* **2010**, *122*, 6517–6521; *Angew. Chem. Int. Ed.* **2010**, *49*, 6373–6377.

[139] D. A. Bock, C. W. Lehmann, B. List, *Proc. Natl. Acad. Sci. U.S.A.* **2010**, *107*, 20636–20641.

[140] T. Kanzian, S. Lakhdar, H. Mayr, *Angew. Chem.* **2010**, *122*, 9717–9720; *Angew. Chem. Int. Ed.* **2010**, *49*, 9526-9529.

[141] J. E. Hein, J. Burés, Y. Lam, M. Hughes, K. N. Houk, A. Armstrong, D. G. Blackmond, *Org. Lett.* **2011**, *13*, 5644–5647.

[142] J. Burés, A. Armstrong, D. G. Blackmond, *Chem. Sci.* **2012**, *3*, 1273-177.

[143] A. Fu, C. Tian, H. Li, P. Li, T. Chu, Z. Wang, J. Liu, *Chemical Physics* **2015**, *455*, 65–72.

[144] M. Orlandi, M. Ceotto, M. Benaglia, *Chem. Sci.* **2016**, *7*, 5421–5427.

[145] D. Sánchez, H. Carneros, A. Castro-Alvarez, E. Llàcer, F. Planas, J. Vilarrasa, *Tetrahedron Lett.* **2016**, *57*, 5254–5258.

[146] L. S. Santos, *Eur. J. Org. Chem.* **2008**, 235–253.

[147] S. Banerjee, S. Mazumdar, *Int. J. Anal. Chem.* **2012**, *2012*, 282574.

[148] P. G. Isenegger, A. Pfaltz, *Chem. Rec.* **2016**, *16*, 2534–2543.

[149] V. G. Santos, M. N. Godoi, T. Regiani, F. H. S. Gama, M. B. Coelho, R. O. M. A. de Souza, M. N. Eberlin, S. J. Garden, *Chem. Eur. J.* **2014**, *20*, 12808–12816.

[150] C. Iacobucci, S. Reale, F. De Angelis, *Angew. Chem.* **2016**, *128*, 3032–3045; *Angew. Chem. Int. Ed.* **2016**, *55*, 2980–2993.

[151] R. Galaverna, N. S. Camilo, M. N. Godoi, F. Coelho, M. N. Eberlin, *J. Org. Chem.* **2016**, *81*, 1089–1098.

[152] J. Luo, A. G. Oliver, J. S. McIndoe, *Dalton Trans.* **2013**, *42*, 11312–11318.

[153] J.-M. Basset, D. Bouchu, G. Godard, I. Karamé, E. Kuntz, F. Lefebvre, N. Legagneux, C. Lucas, D. Michelet, J. B. Tommasino, *Organometallics* **2008**, *27*, 4300–4309.

[154] P. Kumar, I. Cisarova, *J. Organomet. Chem.* **2013**, *735*, 32–37.

[155] H. Zeng, K. Wang, Y. Tian, Y. Niu, L. Greene, Z. Hu, J. K. Lee, *Int. J. Mass Spectrom.* **2014**, *369*, 92–97.

[156] L. Jašíková, M. Anania, S. Hybelbauerová, J. Roithová, *J. Am. Chem. Soc.* **2015**, *137*, 13647–13657.

[157] D. Schröder, H. Schwarz, *Top. Organomet. Chem.* **2007**, *22*, 1–15.

[158] M. Schlangen, H. Schwarz, *Dalton Trans.* **2009**, 10155–10165.

[159] D. K. Böhme, H. Schwarz, *Angew. Chem.* **2005**, *117*, 2388–2406; *Angew. Chem. Int. Ed.* **2005**, *44*, 2336–2354.

[160] S. Shaik, M. Filatov, D. Schröder, H. Schwarz, *Chem. Eur. J.* **1998**, *4*, 193–199.

[161] F. Ogliaro, N. Harris, S. Cohen, M. Filatov, S. P. de Visser, S. Shaik, *J. Am. Chem. Soc.* **2000**, *122*, 8977–8989.

[162] M. C. Holland, G. Berden, J. Oomens, A. J. H. M. Meijer, M. Schäfer, R. Gilmour, *Eur. J. Org. Chem.* **2014**, *2014*, 5675–5680.

[163] J. M. Bakker, T. Besson, J. Lemaire, D. Scuderi, P. Maître, *J. Phys. Chem. A* **2007**, *111*, 13415–13424.

[164] J. M. Bakker, R. K. Sinha, T. Besson, M. Brugnara, P. Tosi, J.-Y. Salpin, P. Maître, *J. Phys. Chem. A* **2008**, *112*, 12393–12400.

[165] F. Lanucara, B. Chiavarino, D. Scuderi, P. Maître, S. Fornarini, M. E. Crestoni, *Chem. Commun.* **2014**, *50*, 3845–3848.

[166] S. Goedecker, *J. Chem. Phys.* **2004**, *120*, 9911–9917.

[167] J. Enkovaara, C. Rostgaard, J. J. Mortensen, J. Chen, M. Dułak, L. Ferrighi, J. Gavnholt, C. Glinsvad, V. Haikola, H. A. Hansen, H. H. Kristoffersen, M. Kuisma, A. H. Larsen, L. Lehtovaara, M. Ljungberg, O. Lopez-Acevedo, P. G. Moses, J. Ojanen, T. Olsen, V. Petzold, N. A. Romero, J. Stausholm-Møller, M. Strange, G. A. Tritsaris, M. Vanin, M. Walter, B. Hammer, H. Häkkinen, G. K. H. Madsen, R. M. Nieminen, J. K. Nørskov, M. Puska, T. T. Rantala, J. Schiøtz, K. S. Thygesen, K. W. Jacobsen, *J. Phys.: Condens. Matter* **2010**, *22*, 253202.

[168] A. H. Larsen, J. J. Mortensen, J. Blomqvist, I. E. Castelli, R. Christensen, M. Dułak, J. Friis, M. N. Groves, B. Hammer, C. Hargus, E. D. Hermes, P. C. Jennings, P. B. Jensen, J. Kermode, J. R. Kitchin, E. L. Kolsbjerg, J. Kubal, K. Kaasbjerg, S. Lysgaard, J. B. Maronsson, T. Maxson, T. Olsen, L. Pastewka, A. Peterson, C. Rostgaard, J. Schiøtz, O. Schütt, M. Strange, K. S. Thygesen, T. Vegge, L. Vilhelmsen, M. Walter, Z. Zeng, K. W. Jacobsen, *J. Phys.: Condens. Matter* **2017**, *29*, 273002.

[169] P. J. Stephens, F. J. Devlin, C. F. Chabalowski, M. J. Frisch, *J. Phys. Chem.* **1994**, *98*, 11623–11627.

[170] S. Grimme, S. Ehrlich, L Goerigk, *J. Comput. Chem.* **2011**, *32*, 1456–1465.

[171] F. Weigend, R. Ahlrichs, *Phys. Chem. Chem. Phys.* **2005**, *7*, 3297–3305.

[172] M. J. Frisch, G. W. Trucks, H. B. Schlegel, G. E. Scuseria, M. A. Robb, J. R. Cheeseman, G. Scalmani, V. Barone, B. Mennucci, G. A. Petersson, H. Nakatsuji, M. Caricato, X. Li, H. P. Hratchian, A. F. Izmaylov, J. Bloino, G. Zheng, J. L. Sonnenberg, M. Hada, M. Ehara, K. Toyota, R. Fukuda, J. Hasegawa, M. Ishida, T. Nakajima, Y. Honda, O. Kitao, H. Nakai, T. Vreven, J. A. Montgomery, Jr., J. E. Peralta, F. Ogliaro, M. Bearpark, J. J. Heyd, E. Brothers, K. N. Kudin, V. N. Staroverov, T. Keith, R. Kobayashi, J. Normand, K. Raghavachari, A. Rendell, J. C. Burant, S. S. Iyengar, J. Tomasi, M. Cossi, N. Rega, J. M. Millam, M. Klene, J. E. Knox, J.B. Cross, V. Bakken, C. Adamo, J. Jaramillo, R. Gomperts, R. E. Stratmann, O. Yazyev, A. J. Austin, R. Cammi, C. Pomelli, J. W. Ochterski, R.L. Martin, K. Morokuma, V. G. Zakrzewski, G. A. Voth, P. Salvador, J. J. Dannenberg, S. Dapprich, A.D. Daniels, O. Farkas, J. B. Foresman, J. V. Ortiz, J. Cioslowski, D. J. Fox; Gaussian 09, revision D. 01; Gaussian, Inc.: Wallingford, CT, 2009.

[173] K. K. Irikura, R. D. Johnson, R. N. Kacker, *J. Phys. Chem. A* **2005**, *109*, 8430–8437.

[174] NIST Mass Spec Data Center, S. E. Stein, director, "Infrared Spectra" in NIST Chemistry WebBook, NIST Standard Reference Database Number 69; P. J. Linstrom, W. G. Mallard, Eds.; National Institute of Standards and Technology: Gaithersburg, MD, 2017 (http://webbook.nist.gov).

[175] W. Pyckhout, C. van Alsenoy, H. J. Geise, *J. Mol. Struct.* **1986**, *144*, 265–279.

[176] J. P. Perdew, K. Burke, M. Ernzerhof, *Phys. Rev. Lett.* **1997**, *78*, 1396.

[177] F. A. Hamprecht, A. J. Cohen, D. J. Tozer, N. C. Handy, *J. Chem. Phys.* **1998**, *109*, 6264–6271.

[178] A. D. Boese, N. C. Handy, *J. Chem. Phys.* **2001**, *114*, 5497–5503.

[179] M. L. Laury, M. J. Carlson, A. K. Wilson, *J. Comput. Chem.* **2012**, *33*, 2380–2387.

[180] B. Chiavarino, M. E. Crestoni, S. Fornarini, J. Lemaire, P. Maître, L. MacAleese, *J. Am. Chem. Soc.* **2006**, *128*, 12553–12561.

[181] I. M. Alecu, J. Zheng, Y. Zhao, D. G. Truhlar, *J. Chem. Theory Comput.* **2010**, *6*, 2872–2887.

[182] M. H. Haindl, J. Hioe, R. M. Gschwind, *J. Am. Chem. Soc.* **2015**, *137*, 12835–12842.

[183] K. N. Rankin, J. W. Gauld, R. J. Boyd, *J. Phys. Chem. A* **2002**, *106*, 5155–5159.

[184] I. A. Konstantinov, L. J. Broadbelt, *Top. Catal.* **2010**, *53*, 1031–1038.

[185] L. Mac Aleese, A. Simon, T. B. McMahon, J.-M. Ortega, D. Scuderi, J. Lemaire, P. Maître, *Int. J. Mass Spectrom.* **2006**, *249–250*, 14–20.

[186] M. A. Ashley, J. S. Hirschi, J. A. Izzo, M. J. Vetticatt, *J. Am. Chem. Soc.* **2016**, *138*, 1756–1759.

[187] J. Oomens, J. D. Steill, B. Redlich, *J. Am. Chem. Soc.* **2009**, *131*, 4310–4319.

[188] D. Scuderi, C. F. Correia, O. P. Balaj, G. Ohanessian, J. Lemaire, P. Maître, *ChemPhysChem* **2009**, *10*, 1630–1641.

[189] R. K. Sinha, E. Nicol, V. Steinmetz, P. Maître, *J. Am. Soc. Mass Spectrom.* **2010**, *21*, 758–772.

[190] U. Mazurek, M. Engeser, C. Lifshitz, *Int. J. Mass Spectrom.* **2006**, *249-250*, 473–476.

[191] G. von Helden, I. Holleman, G. Meijer, B. Sartakov, *Opt. Express* **1999**, *4*, 46–52.

[192] J. Oomens, A. G. G. M. Tielens, B. G. Sartakov, G. von Helden, G. Meijer, *Astrophys. J.* **2003**, *591*, 968–985.

[193] J. Xie., C. Zhu (Eds.), *Sustainable C(sp^3)-H Bond Functionalization*; Springer: Berlin, Heidelberg, 2016.

[194] C.-J. Li, *Acc. Chem. Res.* **2009**, *42*, 335–344.

[195] For a review, see: a) S. A. Girard, T. Knauber, C.-J. Li, *Angew. Chem.* **2014**, *126*, 76–103; *Angew. Chem. Int. Ed.* **2014**, *53*, 74–100; b) For more recent examples, see: Y. Pan, C. W. Kee, L. Chen, C.-H. Tan, *Green Chem.* **2011**, *13*, 2682–2685; M. Rueping, C. Vila, R. M. Koenigs, K. Poscharny, D. C. Fabry, *Chem. Commun.* **2011**, *47*, 2360–2362; G. Bergonzini, C. S. Schindler, C.-J. Wallentin, E. N. Jacobsen, C. R. J. Stephenson, *Chem. Sci.* **2014**, *5*, 112–116; W. Muramatsu, K. Nakano, C.-L. Li, *Org. Biomol. Chem.* **2014**, *12*, 2189–2192; C. Min, A. Sanchawala, D. Seidel, *Org. Lett.* **2014**, *16*, 2756–2759; K. N. Singh, S. V. Kessar, P. Singh, P.; Singh, M. Kaur, A. Batra, *Synthesis* **2014**, *46*, 2644–2650; J. P. Barham, M. P. John, J. A. Murphy, *Beilstein J. Org. Chem.* **2014**, *10*, 2981–2988; C. Yan, Y. Liu, Q. Wang, *Org. Lett.* **2015**, *17*, 5714-5717; G. Wei, C. Zhang, F. Bureš, X. Ye, C.-H. Tan, Z. Jiang, *ACS Catal.* **2016**, *6*, 3708–3712; Z. Peng, Z. Yu, D.-H. Chen, S. Liang, L. Zhang, D. Zhao, L. Song, C. Jiang, *Synlett* **2017**, *28*, 1835–1839.

[196] S.-I. Murahashi, N. Komiya, H. Terai, T. Nakae, *J. Am. Chem. Soc.* **2003**, *125*, 15312–15313.

[197] Z. Li, C.-J. Li, *J. Am. Chem. Soc.* **2004**, *126*, 11810–11811.

[198] J. D. Scott, R. M. Williams, *Chem. Rev.* **2002**, *102*, 1669–1730.

[199] A. S.-K. Tsang, A. S. K. Hashmi, P. Comba, M. Kerscher, B. Chan, M. H. Todd, *Chem. Eur. J.* **2017**, *23*, 9313–9318.

[200] N. Girard, C. Gautier, R. Malassene, J.-P. Hurvois, C. Moinet, L. Toupet, *Synlett* **2004**, *11*, 2005–2009.

[201] N. Girard, J.-P. Hurvois, *Tetrahedron Lett.* **2007**, *48*, 4097–4099.

[202] A. S.-K. Tsang, K. Ingram, J. Keiser, D. B. Hibbert, M. H. Todd, *Org. Biomol. Chem.* **2013**, *11*, 4921–4924.

[203] B. Schweitzer-Chaput, M. Klussmann, *Eur. J. Org. Chem.* **2013**, 666–671.

[204] H. Richter, R. Fröhlich, C.-G. Daniliuc, O. García Mancheño, *Angew. Chem.* **2012**, *124*, 8784–8788; *Angew. Chem. Int. Ed.* **2012**, *51*, 8656–8660.

[205] Z. Xie, L. Liu, W. Chen, H. Zheng, Q. Xu, H. Yuan, H. Lou, *Angew. Chem.* **2014**, *126*, 3985–3989; *Angew. Chem. Int. Ed.* **2014**, *53*, 3904–3908.

[206] X. Liu, S. Sun, Z. Meng, H. Lou, L. Liu, *Org. Lett.* **2015**, *17*, 2396–2399.

[207] M. Odachowski, M. F. Greaney, N. J. Turner, *ACS Catal.* **2018**, *8*, 10032–10035.

[208] T. Wang, M. Schrempp, A. Berndhäuser, O. Schiemann, D. Menche, *Org. Lett.* **2015**, *17*, 3982–3985.

[209] M. C. S. Regino, A. Brajter-Toth, *Anal. Chem.* **1997**, *69*, 5067–5072.

[210] A. Baumann, U. Karst, *Expert Opin. Drug Metab. Toxicol.* **2010**, *6*, 715–731.

[211] M. Klussmann, D. Sureshkumar, *Synthesis* **2011**, 353–369.

[212] C. Zheng, S.-L. You, *RSC Adv.* **2014**, *4*, 6173–6214.

[213] Z. Xie, X. Liu, L. Liu, *Org Lett* **2016**, *18*, 2982–2985.

[214] S. D. McCann, S. S. Stahl, *Acc. Chem. Res.* **2015**, *48*, 1756–1766.

[215] N. Gulzar, B. Schweitzer-Chaput, M. Klussmann, *Catal. Sci. Technol.* **2014**, *4*, 2778–2796.

[216] Z. Shi, C. Zhang, C. Tang, N. Jiao, *Chem. Soc. Rev.* **2012**, *41*, 3381–3430.

[217] A. N. Campbell, S. S. Stahl, *Acc. Chem. Res.* **2012**, *45*, 851–863.

[218] A. E. Wendlandt, A. M. Suess, S. S. Stahl, *Angew. Chem.* **2011**, *123*, 11256–11283; *Angew. Chem. Int. Ed.* **2011**, *50*, 11062–11087.

[219] A. S.-K. Tsang, P. Jensen, J. M. Hook, A. S. K. Hashmi, M. H. Todd, *Pure Appl. Chem.* **2011**, *83*, 655–665.

[220] G.-J. Cheng, L.-J. Song, Y.-F. Yang, X. Zhang, O. Wiest, Y.-D. Wu, *ChemPlusChem* **2013**, *78*, 943–951.

[221] E. Boess, D. Sureshkumar, A. Sud, C. Wirtz, C. Farès, M. Klussmann, *J. Am. Chem. Soc.* **2011**, *133*, 8106–8109.

[222] A. Tanoue, W.-J. Yoo, S. Kobayashi, *Adv. Synth. Catal.* **2013**, *355*, 269-273.

[223] M. Scott, A. Sud, E. Boess, M. Klussmann, *J. Org. Chem.* **2014**, *79*, 12033–12040.

[224] E. Boess, L. M. Wolf, S. Malakar, M. Salamone, M. Bietti, W. Thiel, M. Klussmann, *ACS Catal.* **2016**, *6*, 3253–3261.

[225] E. Boess, C. Schmitz, M. Klussmann, *J. Am. Chem. Soc.* **2012**, *134*, 5317–5325.

[226] H. Bartling, A. Eisenhofer, B. König, R. M. Gschwind, *J. Am. Chem. Soc.* **2016**, *138*, 11860–11871.

[227] M. O. Ratnikov, M. P. Doyle, *J. Am. Chem. Soc.* **2013**, *135*, 1549–1557.

[228] P. Kebarle, U. H. Verkerk, *Mass Spectrom. Rev.* **2009**, *28*, 898–917.

[229] Z. Li, D. S. Bohle, C.-J. Li, *Proc. Natl. Acad. Sci. U.S.A.* **2006**, *103*, 8928–8933.

[230] A. Baumann, W. Lohmann, S. Jahn, U. Karst, *Electroanalysis* **2010**, *22*, 286–292.

[231] L. Gianelli, V. Amendola, L. Fabbrizzi, P. Pallavicini, G. G. Mellerio, *Rapid Commun. Mass Spectrom.* **2001**, *15*, 2347–2353.

[232] A. R. Ross, M. G. Ikonomou, J. A. Thompson, K. J. Orians, *Anal. Chem.* **1998**, *70*, 2225–2235.

[233] K. J. Jobst, J. K. Terlouw, T. Luider, N. A. van Huizen, P. C. Burgers, *Eur. J. Mass Spectrom.* **2015**, *21*, 579–587.

[234] R. J. Herold, S. L. Aggarwal, V. Neff, *Can. J. Chem.* **1963**, *41*, 1368–1380.

[235] N. Fu, L. Li, Q. Yang, S. Luo, *Org. Lett.* **2017**, *19*, 2122–2125.

[236] Q. Yang, L. Zhang, C. Ye, S. Luo, L.-Z. Wu, C.-H. Tung, *Angew. Chem.* **2017**, *129*, 3748–3752; *Angew. Chem. Int. Ed.* **2017**, *56*, 3694–3698.

[237] O. Baslé, N. Borduas, P. Dubois, J. M. Chapuzet, T.-H. Chan, J. Lessard, C.-J. Li, *Chem. Eur. J.* **2010**, *16*, 8162–8166.

[238] M. Ghobrial, M. Schnürch, M. D. Mihovilovic, *J. Org. Chem.* **2011**, *76*, 8781–8793.

[239] J.-B. Yu, G. Peng, Z.-J. Jiang, Z.-K. Hong, W.-K. Su, *Eur. J. Org. Chem.* **2016**, 5340–5344.

[240] J. Cossy, H. Rakotoarisoa, *Tetrahedron Lett.* **2000**, *41*, 2097–2099.

[241] G. R. Fulmer, A. J. M. Miller, N. H. Sherden, H. E. Gottlieb, A. Nudelman, B. M. Stoltz, J. E. Bercaw, K. I. Goldberg, *Organometallics* **2010**, *29*, 2176–2179.

[242] A. Püschl, T. Tedeschi, P. E. Nielsen, *Org. Lett.* **2000**, *2*, 4161–4163.

[243] X.-L. Qiu, F.-L. Qing, *J. Org. Chem.* **2005**, *70*, 3826–3837.

[244] A. Nudelman, Y. Bechor, E. Falb, B. Fischer, B. A. Wexler, A. Nudelman, *Synth. Commun.* **1998**, *28*, 471–474.

[245] F. Y. Kwong, A. Klapars, S. L. Buchwald, *Org. Lett.* **2002**, *4*, 581–584.

[246] Z. Li, C.-J. Li, *J. Am. Chem. Soc.* **2005**, *127*, 6968–6969.

[247] G. M. Coppola, *J. Heterocyclic Chem.* **1991**, *28*, 1769−1772.

[248] E. Alonso, D. J. Ramón, M. Yus, *Tetrahedron* **1997**, *53*, 14355–14368.

[249] M. Ludwig, C. E. Hoesl, G. Höfner, K. T. Wanner, *Eur. J. Med. Chem.* **2006**, *41*, 1003–1010.

[250] S. O'Sullivan, E. Doni, T. Tuttle, J. A. Murphy, *Angew. Chem.* **2014**, *126*, 484–488; *Angew. Chem. Int. Ed.* **2014**, *53*, 474–478.

Appendix

S3 Supporting information to Chapter 3

Probing the gas-phase structure of charge-tagged intermediates of a proline catalyzed aldol reaction – Vibrational spectroscopy distinguishes oxazolidinone from enamine species

J. A. Willms, J. Vidic, J. Barthelmes, V. Steinmetz, T. Bredow, P. Maître, M. Engeser

Contents

S3.1 Mixing tee setup

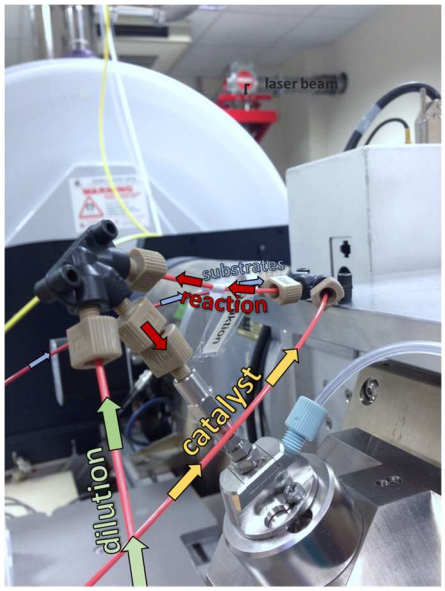

Figure S3.1 – Continuous flow mixing tee setup for the ongoing detection of intermediates ^{1}**A**, ^{1}**B** and ^{1}**A**$_{(acetone)}$.

S3.2 Mass spectra

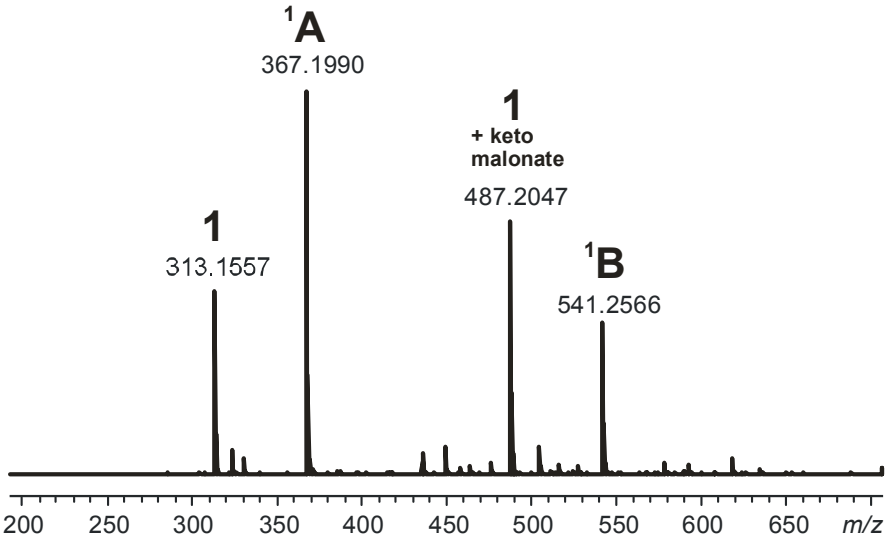

Figure S3.2 – ESI(+) mass spectrum of acetonitrile solutions of diethyl ketomalonate and butyraldehyde [2 mM] as well as catalyst **1** [1 mM] recorded with the continuous-flow setup shown in Figure S3.1.

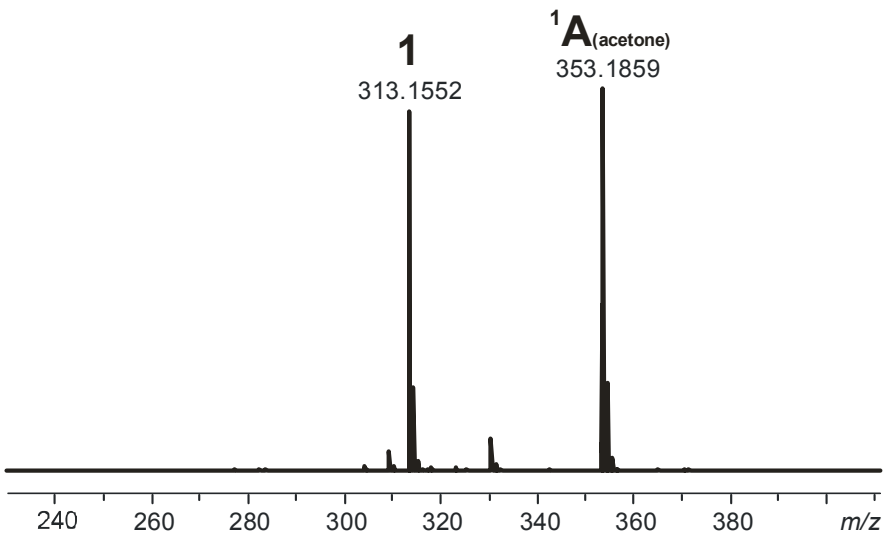

Figure S3.3 – ESI(+) mass spectrum of acetonitrile solutions of acetone [10 % v/v] as well as catalyst **1** [1 mM] recorded with the continuous-flow setup shown in Figure S3.1.

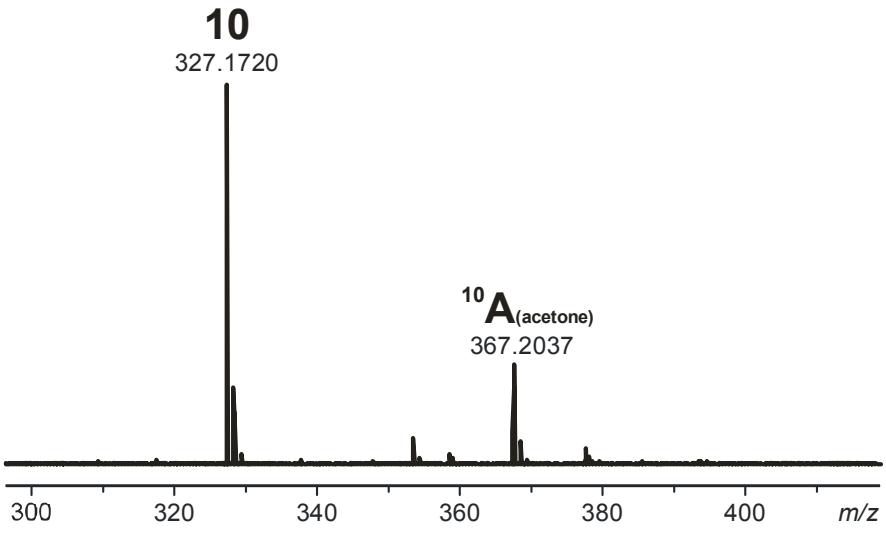

Figure S3.4 – ESI(+) mass spectrum of catalyst **10** [1 mM] and acetone [50 % v/v] in acetonitrile.

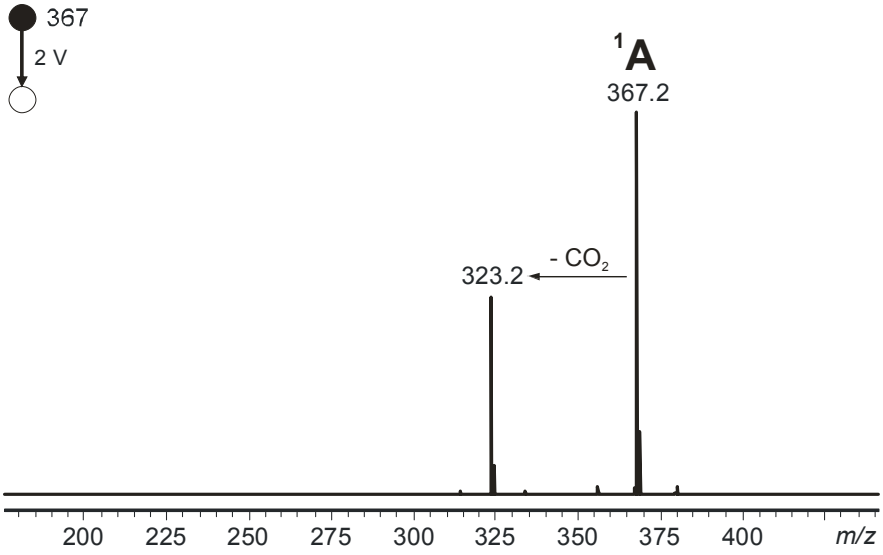

Figure S3.5 – ESI(+) CID MS/MS spectrum of mass-selected **[1]A**.

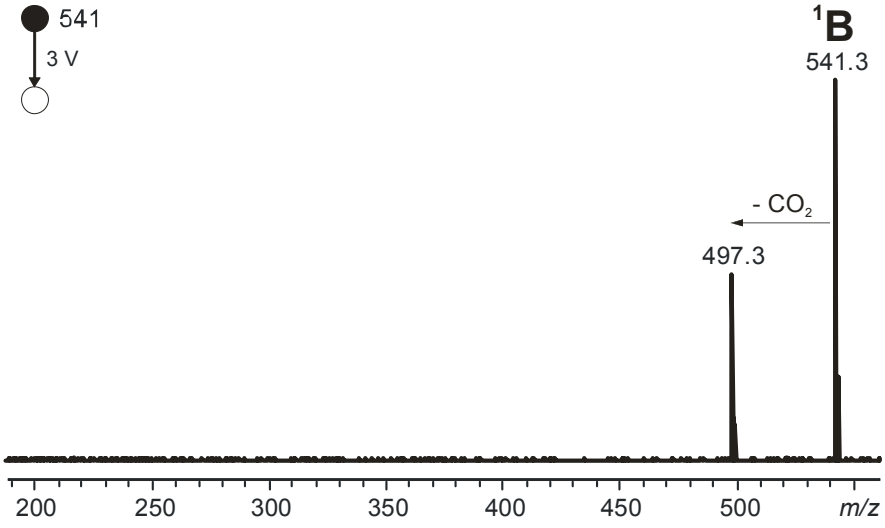

Figure S3.6 – ESI(+) CID MS/MS spectrum of mass-selected **[1]B**.

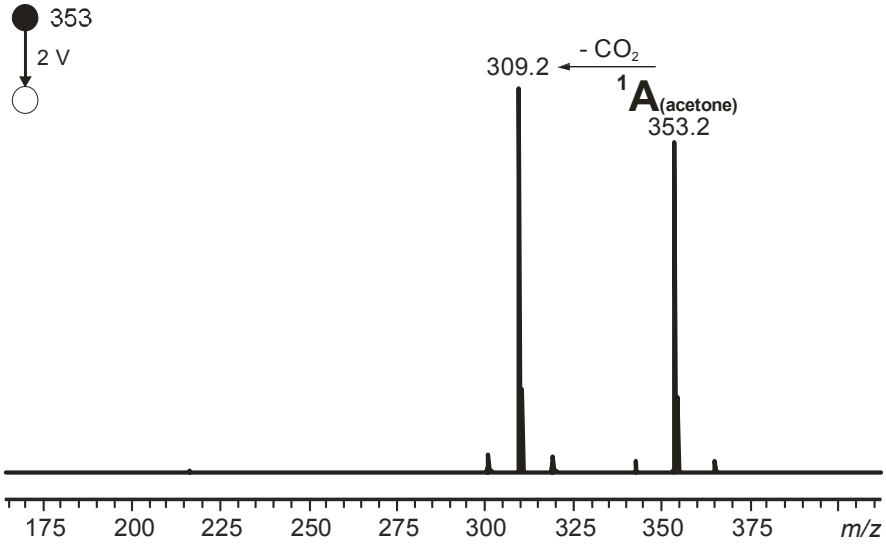

Figure S3.7 – ESI(+) CID MS/MS spectrum of mass-selected $^{1}\mathbf{A}_{(acetone)}$.

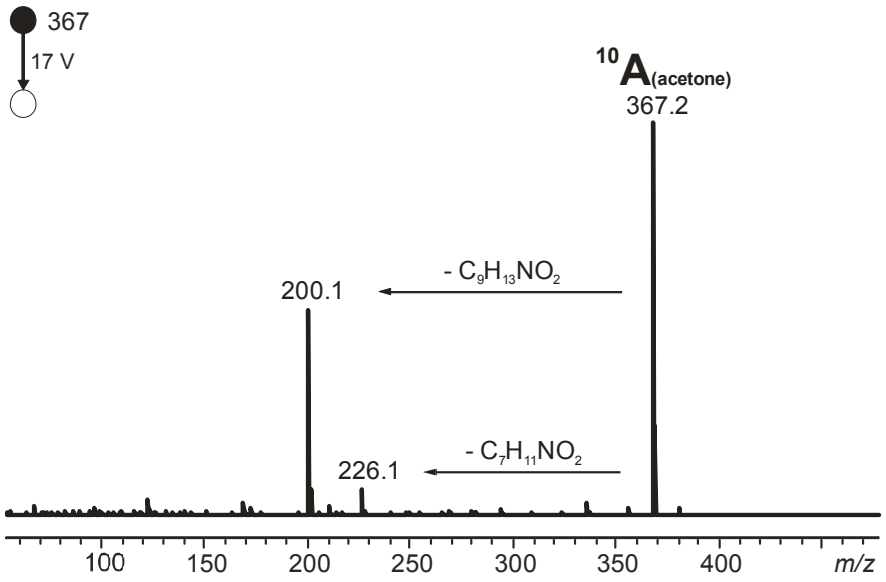

Figure S3.8 – ESI(+) CID MS/MS spectrum of mass-selected $^{10}\mathbf{A}_{(acetone)}$.

S3.3 Additional IRMPD spectra

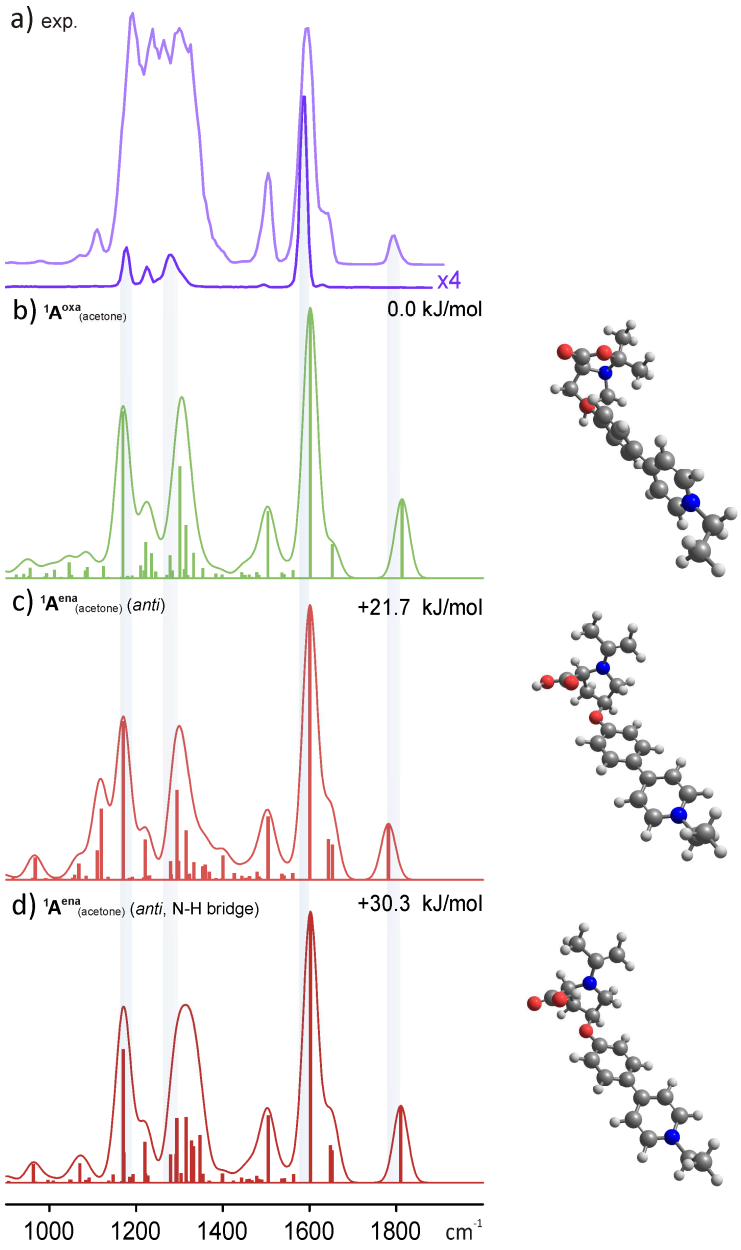

Figure S3.9 – a: IRMPD spectra of $^1A_{(acetone)}$ (*m/z* = 353) with 3 dB (light purple) and 12 dB (deep purple) attenuation; b: Calculated* spectrum of $^1A^{oxa}_{(acetone)}$; c: Calculated* spectrum of $^1A^{ena}_{(acetone)}$ (*anti*); d: Calculated* spectrum of $^1A^{ena}_{(acetone)}$ (*anti*, with N-H bridge); *B3LYP-D3/def2-TZVP (scaling: 0.979).

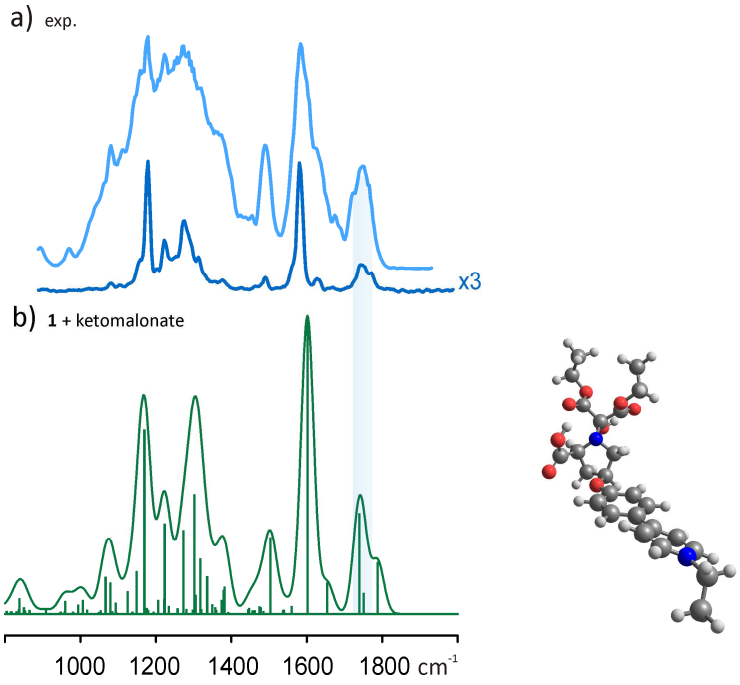

Figure S3.10 – a: IRMPD spectra of the adduct of **1** and diethyl ketomalonate (m/z = 487) with 6 dB (light blue) and 15 dB (deep blue) attenuation; b: Calculated* spectrum of the amine derived from catalyst 1 and diethyl ketomalonate; region of C=O stretching vibrations highlighted; *B3LYP-D3/def2-TZVP (scaling: 0.979).

S3.4 Boltzmann-weighted calculated frequencies of $^{1}A_{oxa}$ (*exo*)

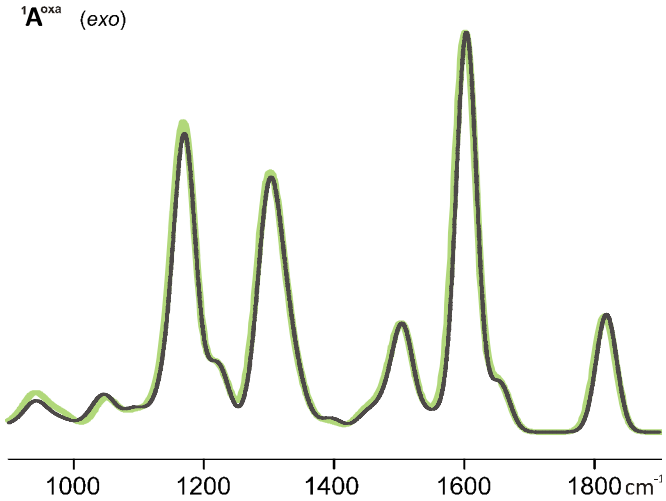

Figure S3.11 – Calculated* spectra of $^{1}A^{oxa}$ (*exo*); bright green line: Calculated* spectrum of the found minimum for $^{1}A^{oxa}$ (*exo*)**; dark grey line: Boltzmann-weighted calculated* spectra of the 32 most stable rotamers observed during the Minima Hopping procedure; *B3LYP-D3/def2-TZVP (scaling: 0.979); **also shown in Figure 3.5.

S3.5 Optimized geometries of the presented structures

S3.5.1 $^{10}A^{ena}_{(acetone)}$ (*anti*) – *anti* enamine derived from acetone and catalyst 10

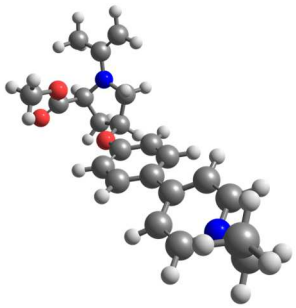

Figure S3.12 – ball-and-stick model of the optimized geometry of $^{10}A^{ena}_{(acetone)}$ (*anti*).

C	-4.66764	-0.19947	-0.59339	H	-4.52173	0.16815	-2.70938
C	-3.96740	-0.37706	-1.94640	H	-3.86965	-1.41604	-2.24972
C	-2.61962	0.29500	-1.72737	H	-2.17161	0.65748	-2.65202
C	-2.89959	1.40680	-0.70731	H	-2.87622	2.39900	-1.16979
N	-4.22248	1.11654	-0.19316	H	-2.14533	1.39720	0.08833
C	-4.31377	-1.35661	0.35054	H	-0.34198	1.53233	-1.76072
O	-4.63042	-2.49622	0.13060	H	2.03329	1.75516	-1.39206
O	-3.63192	-0.95448	1.43061	H	2.16464	-2.22362	0.25150
O	-1.75237	-0.72363	-1.17128	H	-0.23921	-2.44350	-0.14626
C	-0.45603	-0.48494	-0.98329	H	3.80662	2.09877	-0.33457
C	0.19847	0.70894	-1.32048	H	6.22929	2.23642	-0.00054
C	1.55357	0.83325	-1.09424	H	6.59964	-1.88062	0.11812
C	2.31155	-0.21140	-0.54047	H	4.19795	-2.19646	-0.24623
C	1.63286	-1.40234	-0.20819	H	8.29003	1.21607	-0.18631
C	0.28290	-1.53556	-0.41371	H	8.44377	-0.53293	-0.11483
C	3.73772	-0.07385	-0.32651	H	7.74910	1.27556	2.27737
C	4.37406	1.18464	-0.25876	H	9.31372	0.51164	1.98379
C	5.72374	1.28411	-0.06455	H	7.90374	-0.48681	2.34891
N	6.50089	0.18589	0.06706	H	-3.12870	3.21608	1.08770
C	5.93115	-1.03865	0.01437	H	-4.58081	3.46105	2.19146
C	4.58633	-1.19254	-0.17812	H	-6.83846	1.45699	0.52149
C	7.95065	0.32499	0.33902	H	-6.44967	2.08819	2.12329
C	8.23962	0.41097	1.82915	H	-6.10104	0.40592	1.73140
C	-4.74663	1.84462	0.86280	C	-3.29187	-1.98453	2.37331
C	-4.10696	2.89100	1.40781	H	-2.76925	-1.47986	3.18016
C	-6.10872	1.42323	1.33398	H	-2.65353	-2.73141	1.90262
H	-5.74979	-0.23895	-0.71234	H	-4.19254	-2.47183	2.74298

S3.5.2 $^{1}A^{oxa}$ (*exo*) – *exo*-oxazolidinone derived from butyraldehyde and catalyst 1

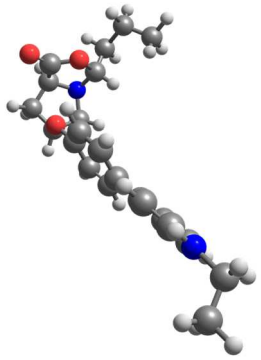

Figure S3.13 – ball-and-stick model of the optimized geometry of $^{1}A^{oxa}$ (*exo*).

C	-4.61055	-1.15871	-0.01542	H	-5.69959	-1.22728	-0.01368
C	-3.95242	-2.52568	-0.21736	H	-4.52266	-3.12353	-0.92797
C	-2.60615	-2.15887	-0.82398	H	-3.85759	-3.07666	0.71576
C	-2.96341	-0.97889	-1.72933	H	-2.11446	-2.98578	-1.33680
N	-4.09199	-0.29145	-1.08491	H	-3.26669	-1.36347	-2.70704
C	-4.16003	-0.47321	1.27765	H	-2.12925	-0.29611	-1.89015
O	-3.65232	0.73858	0.96435	H	-0.19688	-1.96173	-1.89738
O	-4.21492	-0.90382	2.39079	H	2.11368	-1.24414	-1.94158
O	-1.79925	-1.72734	0.29408	H	1.77537	0.12410	2.12866
C	-0.53226	-1.34164	0.14803	H	-0.56105	-0.61705	2.16047
C	0.22745	-1.49997	-1.01906	H	3.85856	-0.10050	2.20824
C	1.54167	-1.07872	-1.03916	H	6.19432	0.62963	2.07927
C	2.14961	-0.50036	0.08699	H	6.07232	0.79653	-2.05048
C	1.36405	-0.35075	1.24902	H	3.72079	0.10804	-2.09813
C	0.05218	-0.75150	1.28025	H	7.84768	1.69261	0.88246
C	3.53580	-0.07877	0.05929	H	7.79609	1.76182	-0.87274
C	4.28938	0.09879	1.23968	H	8.39938	-0.76716	0.77558
C	5.59636	0.49763	1.18958	H	9.58840	0.19464	-0.10706
N	6.21519	0.74079	0.01304	H	8.34806	-0.69685	-0.99290
C	5.53076	0.58025	-1.14138	H	-2.87367	1.39465	-0.81726
C	4.22227	0.18354	-1.14609	H	-5.88297	1.51332	-0.34746
C	7.65050	1.10805	-0.01446	H	-5.03385	2.16260	-1.73721
C	8.54486	-0.11915	-0.08924	H	-4.72621	3.12455	1.15395
C	-3.82209	0.99303	-0.46239	H	-5.65506	3.92437	-0.09362
C	-4.94994	1.98991	-0.66059	H	-2.60365	3.57903	-0.08730
C	-4.76512	3.31526	0.07967	H	-3.49624	5.07415	0.14039
C	-3.52692	4.10029	-0.34963	H	-3.52113	4.27243	-1.42912

S3.5.3 $^{1}A^{oxa}$ (*endo*) – *endo*-oxazolidinone derived from butyraldehyde and catalyst 1

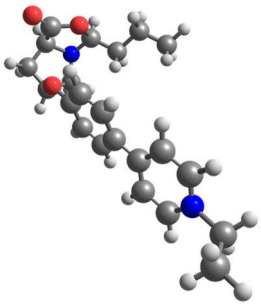

Figure S3.14 – ball-and-stick model of the optimized geometry of $^{1}A^{oxa}$ (*endo*).

H	8.03958	-1.39090	0.38876	O	-2.21891	-1.63054	0.31543
C	8.16004	-0.36489	0.73777	H	-1.83993	1.44021	-0.64319
H	9.22054	-0.11609	0.70298	H	-2.40739	-0.16541	-1.87892
H	7.83216	-0.31090	1.77635	H	-2.70387	-2.81878	-1.32747
H	7.50727	1.63554	0.20382	C	-1.26922	4.12132	-0.67019
H	7.71170	0.56291	-1.17311	C	-3.08798	-1.94818	-0.79523
C	7.38475	0.60842	-0.13576	H	-2.51645	3.30729	0.89101
N	5.93172	0.31806	-0.12531	C	-2.72334	2.05340	-0.84124
H	5.61109	1.54125	1.51271	C	-3.31708	-0.72185	-1.67719
H	6.08453	-0.95003	-1.75351	C	-2.53982	3.42494	-0.19408
C	5.13649	0.85571	0.82608	H	-2.81220	2.16421	-1.92570
C	5.40127	-0.54065	-1.02409	H	-3.71475	-1.05562	-2.63989
C	3.80454	0.55493	0.89687	O	-3.76367	1.02123	1.08558
C	4.07546	-0.87400	-0.99683	H	-4.41776	-2.73977	0.75064
H	3.21721	1.04205	1.65920	C	-3.95229	1.33544	-0.33363
H	3.71883	-1.58259	-1.72774	H	-3.40932	4.04842	-0.42015
C	3.20790	-0.33542	-0.02236	C	-4.45919	-2.16230	-0.17020
C	1.79942	-0.67320	0.03422	N	-4.32485	0.09454	-0.98511
H	1.65934	-1.35279	-2.01261	O	-4.46266	-0.60158	2.47337
H	1.52220	-0.09114	2.10406	C	-4.38919	-0.13938	1.37375
C	1.13301	-1.21064	-1.07907	H	-5.10919	-2.67130	-0.88144
C	1.04878	-0.47630	1.21204	C	-4.93751	-0.72899	0.07063
C	-0.20897	-1.53025	-1.03797	H	-4.81309	2.01012	-0.36412
C	-0.28198	-0.80522	1.27407	H	-6.02717	-0.65364	0.08479
H	-0.68882	-1.92843	-1.91876	H	-0.38345	3.52845	-0.42634
H	-0.85868	-0.66660	2.17799	H	-1.15478	5.09874	-0.20021
C	-0.93068	-1.33594	0.14757	H	-1.28014	4.27205	-1.75228

S3.5.4 $^{1}A^{ena}$ (*E*, *anti*) – *anti*-enamine derived from butyraldehyde and catalyst 1

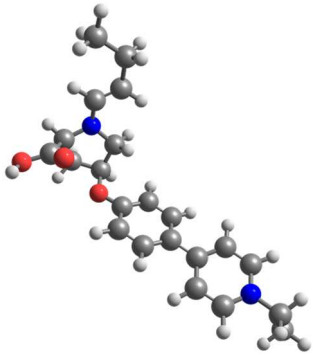

Figure S3.15 – ball-and-stick model of the optimized geometry of $^{1}A^{ena}$ (*E*, *anti*).

C	-0.39698	-1.70603	-0.66266
C	-1.70114	-1.31491	-0.83048
C	-2.35145	-0.50069	0.12014
C	-1.61674	-0.11239	1.25282
C	-0.30973	-0.50970	1.44205
C	0.31871	-1.31366	0.47990
H	0.11309	-2.29962	-1.40774
H	-2.21041	-1.60702	-1.73806
H	-2.08215	0.48398	2.02525
H	0.21432	-0.20191	2.33379
C	-3.72330	-0.07740	-0.06779
C	-4.26850	1.03876	0.60409
C	-4.60468	-0.75018	-0.94226
C	-5.56546	1.42048	0.40211
H	-3.66346	1.63673	1.26722
C	-5.89369	-0.32674	-1.10937
H	-4.28735	-1.62840	-1.48202
H	-5.99902	2.27722	0.89659
H	-6.58646	-0.83101	-1.76689
C	-7.79317	1.14746	-0.60119
H	-7.83670	2.22907	-0.48470
H	-8.08204	0.91473	-1.62474
C	-8.68786	0.44184	0.40544
H	-8.39991	0.68547	1.42856
H	-9.71968	0.76022	0.25779
H	-8.64508	-0.64069	0.28135
N	-6.37432	0.75038	-0.44907
O	1.56997	-1.76315	0.56310
C	2.47411	-1.26580	1.57632
C	3.79219	-1.99632	1.34653
C	2.80718	0.21603	1.35468
H	2.04485	-1.47172	2.55681
C	4.50629	-1.11247	0.31062
H	3.63987	-3.02323	1.02410
H	4.37137	-1.99792	2.26903
H	2.84602	0.76609	2.30181
H	2.04712	0.69672	0.72782
H	5.59008	-1.23088	0.37432
C	4.09526	-1.47503	-1.12032
O	3.34571	-0.84753	-1.81670
C	4.63885	1.35144	0.14735
H	5.55809	1.16855	-0.39433
C	4.14542	2.58839	0.25310
H	3.22245	2.74759	0.80062
C	4.77727	3.82190	-0.32682
H	4.04488	4.32031	-0.97281
H	4.97290	4.53456	0.48335
C	6.06326	3.59997	-1.11505
N	4.10077	0.20801	0.70957
O	4.69961	-2.61737	-1.51107
H	4.41806	-2.80747	-2.42011
H	5.89926	2.93791	-1.96805
H	6.84404	3.15964	-0.49109
H	6.44350	4.54695	-1.49913

S3.5.5 $^{1}A^{ena}$ (*E, anti*, with N-H bridge*) – *anti*-enamine with N-H bond derived from butyraldehyde and catalyst 1

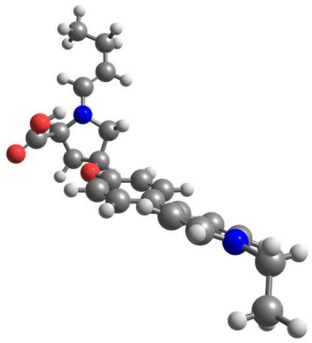

Figure S3.16 – ball-and-stick model of the optimized geometry of $^{1}A^{ena}$ (*E*, *anti*, with N-H bridge*).

C	-0.51327	-1.57099	-0.44475	O	1.49150	-1.45178	0.70440
C	-1.82099	-1.19975	-0.63147	C	2.43208	-0.88159	1.63872
C	-2.44784	-0.26786	0.22135	C	3.68070	-1.74261	1.52878
C	-1.68150	0.27807	1.26345	C	2.91755	0.48364	1.16486
C	-0.35909	-0.07038	1.45255	H	1.99673	-0.86737	2.63741
C	0.23673	-1.01078	0.60164	C	4.32525	-1.23485	0.23220
H	-0.03417	-2.29697	-1.08683	H	3.46277	-2.80685	1.49921
H	-2.37691	-1.66868	-1.43104	H	4.33090	-1.53631	2.37880
H	-2.10912	1.02161	1.92156	H	3.37416	1.02222	2.00561
H	0.20172	0.38793	2.25235	H	2.11578	1.10791	0.76706
C	-3.83290	0.11352	0.02548	H	5.41134	-1.32587	0.27104
C	-4.61068	0.68647	1.05431	C	3.86252	-2.06314	-0.98149
C	-4.49299	-0.06446	-1.20963	O	4.03942	-3.24570	-1.05215
C	-5.91541	1.03657	0.84147	C	4.85362	1.14301	-0.21644
H	-4.20172	0.83779	2.04094	H	5.65474	0.74816	-0.82793
C	-5.80023	0.30300	-1.37048	C	4.80467	2.43997	0.08976
H	-3.97239	-0.46590	-2.06478	H	3.98221	2.81769	0.68802
H	-6.53218	1.46620	1.61707	C	5.80885	3.46727	-0.34973
H	-6.32215	0.18580	-2.30883	H	5.28357	4.25217	-0.90638
C	-7.94182	1.17922	-0.54382	H	6.20433	3.96853	0.54087
H	-8.16140	2.02674	0.10306	C	6.96859	2.94602	-1.19011
H	-8.06290	1.51031	-1.57391	N	3.90778	0.17216	0.13861
C	-8.83650	-0.00939	-0.23052	O	3.25981	-1.35543	-1.94738
H	-9.87844	0.27423	-0.37781	H	3.20804	-0.43699	-1.61464
H	-8.61820	-0.85257	-0.88662	H	7.64160	3.76108	-1.45625
H	-8.71503	-0.33358	0.80348	H	6.61768	2.49076	-2.11856
N	-6.50826	0.85211	-0.35879	H	7.55244	2.19957	-0.64745

* between the proton of the carboxylic acid function and the pyrrolidine nitrogen

S3.5.6 $^{1}B^{oxa}$ (*exo*) – *exo*-oxazolidinone derived from butyraldehyde, diethyl ketomalonate and catalyst 1

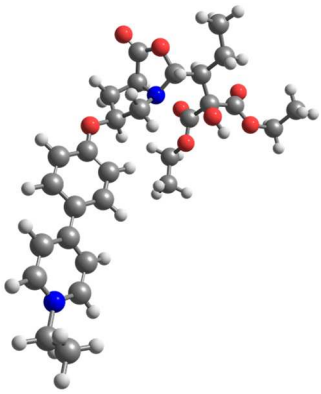

Figure S3.17 – ball-and-stick model of the optimized geometry of $^{1}B^{oxa}$ (*exo*).

N	2.20340	-1.33499	-0.05615	O	4.35742	3.26929	-0.22832
C	2.53156	-2.51121	0.75988	C	6.18606	4.56459	-1.20990
C	1.19479	-3.12055	1.20156	C	5.27380	4.38018	-0.01749
C	0.17000	-2.07889	0.75494	H	3.16146	-2.22280	1.60479
C	0.81377	-1.44750	-0.47799	H	1.15523	-3.31424	2.27021
C	3.19932	-1.27540	-1.11099	H	1.00476	-4.06017	0.68266
C	4.34526	-0.29697	-0.81304	H	0.00972	-1.33284	1.53547
C	3.35761	-3.38170	-0.17809	H	0.42289	-0.46591	-0.74112
O	3.70842	-2.62601	-1.24932	H	0.67111	-2.12531	-1.33253
O	3.65856	-4.52952	-0.05281	H	2.72856	-1.01485	-2.05732
C	5.16903	0.01230	-2.07195	H	4.99128	-0.72908	-0.04790
C	3.72760	0.97974	-0.20861	H	5.89389	0.78602	-1.81953
O	2.73585	1.44251	-1.09684	H	4.50376	0.44015	-2.82657
N	-8.47390	1.15648	-0.30643	H	2.56389	2.37119	-0.90203
C	-8.28587	-0.09015	-0.79319	H	-9.13388	-0.54323	-1.28525
C	-7.08330	-0.72967	-0.67222	H	-6.99015	-1.71543	-1.10011
C	-5.98727	-0.10736	-0.03680	H	-5.46160	1.73679	0.98616
C	-6.22755	1.19403	0.45477	H	-7.65944	2.77909	0.68645
C	-7.44987	1.78914	0.30872	H	-5.46270	-2.77972	-0.13067
C	-4.70312	-0.76360	0.10380	H	-3.28352	-3.86602	0.09623
C	-4.58439	-2.16551	0.01012	H	-1.41623	-0.03328	0.58464
C	-3.36974	-2.78960	0.14509	H	-3.56334	1.05254	0.37153
C	-2.20506	-2.03554	0.36314	H	-9.92590	2.49034	0.35699
C	-2.29775	-0.63889	0.44719	H	-10.54316	1.09062	-0.50782
C	-3.52889	-0.02735	0.32998	H	-8.99813	3.41976	-1.79758
O	-1.07455	-2.73591	0.47685	H	-10.73922	3.14993	-1.91400
C	-9.76590	1.85266	-0.51086	H	-9.62148	2.00978	-2.66854
C	-9.77491	2.65451	-1.80262	H	5.26622	-1.95155	-3.03605
C	5.92967	-1.17748	-2.65467	H	6.57166	-1.63868	-1.90202
C	3.16142	0.68105	1.20331	H	6.56488	-0.84343	-3.47624
O	3.74176	0.03585	2.03651	H	-0.23253	1.96530	3.81444
O	2.02461	1.36150	1.43269	H	-0.52128	1.68567	2.09124
C	0.20952	2.04173	2.81993	H	0.41274	3.09302	2.61438
C	1.47860	1.22547	2.76021	H	2.21957	1.56674	3.48361
C	4.81941	2.04152	0.05250	H	1.29632	0.16706	2.95608
O	5.90660	1.79738	0.49361	H	5.60826	4.71249	-2.12290

H	6.83826	3.70156	-1.33685	H	5.83686	4.18856	0.89419
H	6.81285	5.44449	-1.05475	H	4.61965	5.23707	0.12951

S3.5.7 $^{1}B^{oxa}$ (*endo*) – *endo*-oxazolidinone derived from butyraldehyde, diethyl ketomalonate and catalyst 1

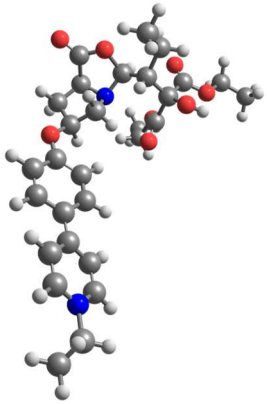

Figure S3.18 – ball-and-stick model of the optimized geometry of $^{1}B^{oxa}$ (*endo*).

N	-2.27573	1.49421	0.53353	C	-2.58787	-1.07839	2.96670
C	-2.54211	2.88100	0.95902	C	-4.63857	-1.70578	-0.43307
C	-1.19530	3.47453	1.38935	O	-5.54442	-0.94760	-0.22114
C	-0.20614	2.34832	1.07675	O	-4.74759	-3.04042	-0.43428
C	-0.91049	1.54173	-0.00765	C	-5.96274	-5.08966	-0.22616
C	-3.34258	1.22948	-0.40817	C	-6.06240	-3.58703	-0.14245
C	-3.09226	0.09876	-1.39590	H	-3.29861	2.91018	1.74632
C	-3.14592	3.50952	-0.30491	H	-1.17947	3.75889	2.43846
O	-3.55706	2.50193	-1.10943	H	-0.95865	4.35724	0.79611
O	-3.23588	4.66742	-0.58394	H	-0.03165	1.72924	1.95875
C	-4.01280	0.17257	-2.63221	H	-0.51706	0.54181	-0.14628
C	-3.17879	-1.29849	-0.71989	H	-0.83657	2.09257	-0.95575
O	-2.56870	-2.18357	-1.63209	H	-4.97591	0.59425	-2.34632
N	8.04187	-1.57258	-0.55717	H	-4.20125	-0.84584	-2.97360
C	7.87597	-0.36141	-1.13415	H	-2.83349	-3.08400	-1.40587
C	6.74193	0.37505	-0.93408	H	8.68146	-0.02137	-1.76829
C	5.69785	-0.10119	-0.11101	H	6.65430	1.31755	-1.45103
C	5.91485	-1.36850	0.47309	H	5.18477	-1.80704	1.13499
C	7.06801	-2.06481	0.24104	H	7.25894	-3.03064	0.68520
C	4.48500	0.65783	0.11172	H	5.32158	2.57739	-0.44970
C	4.43534	2.04596	-0.13234	H	3.25045	3.83082	-0.10452
C	3.28329	2.76406	0.06720	H	1.25330	0.21070	1.06846
C	2.11346	2.12153	0.50457	H	3.28498	-1.03042	0.73294
C	2.13841	0.74132	0.75435	H	9.67313	-2.09080	-1.73787
C	3.30933	0.03723	0.56536	H	9.06170	-3.37898	-0.71080
O	1.04207	2.90791	0.64892	H	10.58160	-0.89597	0.28952
C	9.30850	-2.31896	-0.73779	H	11.24696	-2.52633	0.15634
C	10.33311	-1.95710	0.32563	H	9.96543	-2.19333	1.32467
C	-3.40389	0.96587	-3.78506	H	-3.21369	2.00038	-3.50324
C	-2.39169	-1.33514	0.61848	H	-4.07942	0.97110	-4.64168
O	-1.19626	-1.46716	0.68267	H	-2.46188	0.51600	-4.10780
O	-3.20396	-1.22046	1.66608	H	-3.26944	-0.79259	4.97443
C	-3.69590	-0.91208	3.97738	H	-4.35006	-1.78416	3.98732

H	-4.29840	-0.03206	3.75150	H	-5.66344	-5.40781	-1.22539
H	-1.93428	-0.20605	2.92412	H	-6.76733	-3.17654	-0.86485
H	-1.97654	-1.96023	3.15975	H	-6.35554	-3.24339	0.84967
H	-6.93577	-5.53087	-0.00595	H	-4.25920	1.03678	0.14898
H	-5.24171	-5.47629	0.49495	H	-2.06145	0.15666	-1.74724

S3.5.8 $^{1}B^{ena}$ (*E*, *anti,* with N-H bridge*) – *anti*-enamine derived from butyraldehyde, diethyl ketomalonate and catalyst 1

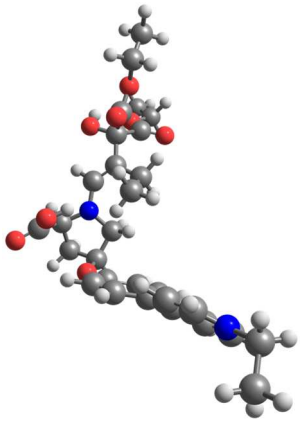

Figure S3.19 – ball-and-stick model of the optimized geometry of $^{1}B^{ena}$ (*E*, *anti*, with N-H bridge*).

N	-1.43413	2.19673	-0.00441	C	3.53325	0.87173	1.50232
C	-1.52234	3.56598	-0.52015	O	1.20620	3.40409	0.26195
C	-0.87914	4.43742	0.56838	C	8.35560	-3.40097	0.18208
C	0.11169	3.47638	1.20610	C	9.70027	-2.73442	-0.06090
C	-0.66457	2.16850	1.23859	C	-0.12922	-0.76151	-0.47331
C	-2.50136	1.32105	-0.22243	C	-3.62122	-1.96570	-1.15882
C	-2.51636	0.00350	0.01064	O	-2.68562	-2.13467	-1.89220
C	-0.79558	3.73850	-1.86763	O	-4.68376	-2.76908	-1.07406
O	-0.67111	4.80832	-2.39142	C	-5.98661	-4.67345	-1.68601
O	-0.32159	2.60804	-2.41445	C	-4.71052	-3.91660	-1.96051
C	-1.33156	-0.81427	0.47621	C	-4.38406	-1.23266	1.11001
C	-3.82472	-0.73254	-0.23920	O	-3.78187	-1.95772	1.85654
O	-4.74463	0.09421	-0.92503	O	-5.61442	-0.76193	1.33650
N	7.25282	-2.41240	0.22614	C	-7.64652	-0.58647	2.58330
C	6.62118	-2.04635	-0.91135	C	-6.26887	-1.19997	2.55798
C	5.64212	-1.09188	-0.90826	H	-2.56071	3.85414	-0.69771
C	5.25574	-0.44891	0.28743	H	-1.62201	4.73119	1.30972
C	5.94232	-0.85983	1.44987	H	-0.40887	5.32944	0.16390
C	6.91548	-1.81884	1.39248	H	0.48015	3.79364	2.18152
C	4.21769	0.56286	0.31539	H	-1.32159	2.14982	2.11645
C	3.85509	1.26402	-0.85195	H	-0.01582	1.29883	1.29448
C	2.86222	2.21217	-0.83529	H	-1.63798	-1.85039	0.58916
C	2.16969	2.48275	0.35375	H	-1.03186	-0.50658	1.48153
C	2.51994	1.80768	1.52980	H	-5.61972	-0.05633	-0.54568

* between the proton of the carboxylic acid function and the pyrrolidine nitrogen

H	6.92510	-2.55944	-1.81188
H	5.15075	-0.86790	-1.84202
H	5.73294	-0.40821	2.40687
H	7.46207	-2.14069	2.26664
H	4.37523	1.08306	-1.78204
H	2.57650	2.74918	-1.72897
H	2.00157	2.00777	2.45548
H	3.76421	0.34485	2.41764
H	8.11426	-4.11290	-0.60540
H	8.34077	-3.93858	1.12862
H	9.71206	-2.20496	-1.01409
H	10.48141	-3.49405	-0.08440
H	9.93868	-2.02570	0.73277
H	-0.42254	-1.10417	-1.46390
H	-0.51738	1.88263	-1.79291
H	-3.37820	1.78237	-0.65672
H	0.66974	-1.40882	-0.10501
H	0.28647	0.24302	-0.56605
H	-6.04237	-5.54541	-2.33927
H	-6.85968	-4.04827	-1.87559
H	-6.02152	-5.01740	-0.65179
H	-3.82243	-4.51832	-1.76577
H	-4.65591	-3.55435	-2.98740
H	-8.16493	-0.89402	3.49256
H	-8.23738	-0.91431	1.72740
H	-7.59157	0.50254	2.57324
H	-5.65605	-0.88176	3.40130
H	-6.29721	-2.28935	2.55139
H	-0.51738	1.88263	-1.79291
H	-3.37820	1.78237	-0.65672

S3.5.9 $^{1}A^{oxa}_{(acetone)}$ – oxazolidinone derived from acetone and catalyst 1

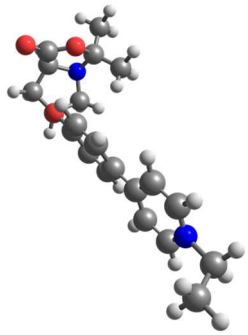

Figure S3 20 – ball-and-stick model of the optimized geometry of $^{1}A^{oxa}_{(acetone)}$.

H	-9.30560	-0.25817	0.58484
C	-8.24574	-0.02746	0.69080
H	-7.92794	-0.33773	1.68666
H	-8.12311	1.05293	0.60831
H	-7.58443	-1.83408	-0.31447
H	-7.77893	-0.45504	-1.38608
C	-7.46093	-0.75504	-0.38906
N	-6.00847	-0.47760	-0.29405
H	-5.69147	-2.09871	0.95244
H	-6.15778	1.18430	-1.51812
C	-5.21554	-1.25304	0.47817
C	-5.47618	0.59287	-0.92464
C	-3.88387	-0.98319	0.63118
C	-4.15064	0.90616	-0.80447
H	-3.29816	-1.65906	1.23413
H	-3.79208	1.78597	-1.31522
C	-3.28520	0.12284	-0.01052
C	-1.87635	0.42965	0.13778
H	-1.73007	1.63896	-1.64738
H	-1.60587	-0.69247	1.97272
C	-1.20562	1.24592	-0.78762
C	-1.12855	-0.08320	1.21836
C	0.13840	1.53422	-0.66195
C	0.20389	0.20807	1.36661
H	0.62231	2.15402	-1.40091
H	0.77866	-0.17384	2.19888
C	0.85778	1.01921	0.42494
O	2.14836	1.24372	0.66377
H	1.75148	-1.36053	-1.00609
H	2.36686	0.45994	-1.86682
H	2.62927	2.84532	-0.58140
C	3.01932	1.86422	-0.30871
C	2.60932	-1.90807	-1.39322
C	3.26937	0.93444	-1.49561
H	2.47174	-2.96109	-1.15386
H	2.64767	-1.80631	-2.47776
H	3.68198	1.52912	-2.31602
O	3.72467	-1.50706	0.69240
H	4.33344	2.20057	1.40667
C	3.90375	-1.43067	-0.76836

C	4.38429	1.90519	0.36107	C	5.06632	-2.34885	-1.12266
N	4.27053	-0.04210	-1.04641	H	5.96683	0.40861	0.19214
O	4.42154	-0.32387	2.46980	H	5.99104	-1.98922	-0.67227
C	4.34171	-0.46671	1.28536	H	5.20031	-2.36983	-2.20387
H	5.03271	2.59836	-0.17420	H	4.87607	-3.35949	-0.76268
C	4.87684	0.46560	0.19520				

S3.5.10 $^{1}A^{ena}_{(acetone)}$ (*anti*) – *anti* enamine derived from acetone and catalyst 1

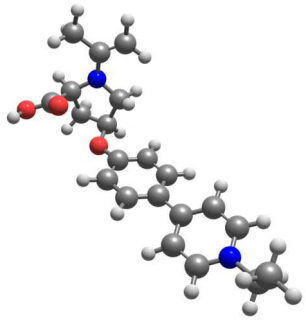

Figure S3.21 – ball-and-stick model of the optimized geometry of $^{1}A^{ena}_{(acetone)}$ (*anti*).

C	-4.74900	-0.32216	-0.11551	H	-5.83787	-0.30094	-0.08098
C	-4.26250	-1.08310	-1.36018	H	-4.91013	-0.83592	-2.20053
C	-2.87651	-0.50129	-1.60202	H	-4.24076	-2.16290	-1.23731
C	-2.98337	0.94895	-1.12051	H	-2.55517	-0.59054	-2.63970
N	-4.18996	0.99015	-0.32000	H	-3.05264	1.64650	-1.96246
C	-4.27198	-0.99447	1.17563	H	-2.10480	1.23245	-0.53220
O	-3.40028	-0.59407	1.89707	H	-4.65215	-2.51022	2.23669
O	-4.97852	-2.12032	1.41018	H	-0.54238	0.38375	-2.38263
O	-1.97932	-1.27311	-0.77025	H	1.83259	0.75899	-2.13826
C	-0.67795	-0.98937	-0.71564	H	1.91706	-1.91423	1.23719
C	-0.01127	-0.11716	-1.58799	H	-0.48794	-2.28658	0.97506
C	1.34192	0.10089	-1.43477	H	3.56129	1.62018	-1.29621
C	2.08486	-0.54087	-0.43018	H	5.96906	1.95398	-0.98595
C	1.39659	-1.42557	0.42546	H	6.35429	-1.61936	1.05930
C	0.04756	-1.63996	0.29484	H	3.96901	-2.12343	0.80766
C	3.50320	-0.29533	-0.27105	H	8.04082	1.01859	-0.59459
C	4.13070	0.86102	-0.78339	H	8.19976	-0.49031	0.29171
C	5.47092	1.07083	-0.61391	H	7.38678	2.20663	1.53341
N	6.24710	0.18062	0.04371	H	8.96790	1.43618	1.69017
C	5.68611	-0.93969	0.55119	H	7.54848	0.68629	2.42595
C	4.35070	-1.19632	0.40982	H	-2.89728	3.34887	-0.23243
C	7.68228	0.46730	0.27299	H	-4.10345	4.11081	0.93024
C	7.90265	1.24630	1.55995	H	-6.62436	1.76961	0.66152
C	-4.50966	2.11572	0.42343	H	-5.93496	2.96256	1.76320
C	-3.78901	3.24625	0.36716	H	-5.64784	1.24694	2.03758
C	-5.74794	2.01414	1.26661				

S3.5.11 $^{1}A^{ena}_{(acetone)}$ (*anti*, with N-H bridge*) – *anti* enamine derived from acetone and catalyst 1

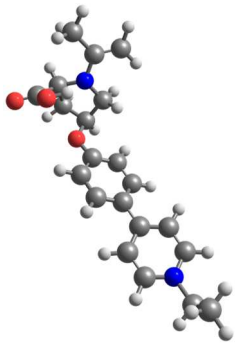

Figure S3.22 – ball-and-stick model of the optimized geometry of $^{1}A^{ena}_{(acetone)}$ (*anti*, with N-H bridge*).

C	-4.71566	-0.45108	-0.19160	H	-5.80269	-0.41519	-0.19398
C	-4.18326	-0.80600	-1.58675	H	-4.82799	-0.37629	-2.35329
C	-2.83563	-0.10601	-1.62361	H	-4.11165	-1.87863	-1.74603
C	-3.11301	1.20488	-0.89984	H	-2.44222	0.02796	-2.63060
N	-4.11641	0.85849	0.10433	H	-3.50360	1.94261	-1.61190
C	-4.32380	-1.53028	0.83590	H	-2.22176	1.63203	-0.43755
O	-4.69402	-2.66479	0.73877	H	-3.36214	-0.16005	1.66353
O	-3.54510	-1.10292	1.84182	H	-0.48399	0.93958	-2.18708
O	-1.94348	-0.94425	-0.85919	H	1.90045	1.22201	-1.90414
C	-0.63937	-0.67810	-0.75778	H	1.93861	-1.94052	1.01930
C	0.03861	0.31039	-1.48307	H	-0.47568	-2.22419	0.71226
C	1.39810	0.47363	-1.30700	H	3.67560	1.88257	-0.97956
C	2.13058	-0.33362	-0.42234	H	6.10382	2.06941	-0.69941
C	1.42569	-1.31961	0.29816	H	6.38389	-1.78793	0.76311
C	0.07189	-1.48490	0.14434	H	3.97269	-2.15345	0.51214
C	3.56151	-0.16468	-0.26027	H	8.13489	1.02123	-0.51512
C	4.22421	1.03203	-0.60639	H	8.25829	-0.62803	0.07874
C	5.57689	1.16021	-0.45008	H	7.61301	1.82975	1.81710
N	6.32924	0.14910	0.03729	H	9.16036	0.98070	1.76566
C	5.73325	-1.01239	0.38653	H	7.73433	0.16769	2.41548
C	4.38442	-1.19159	0.24978	H	-3.65250	3.51592	0.01317
C	7.78353	0.33592	0.25420	H	-5.02178	3.93160	1.16746
C	8.08344	0.86041	1.64916	H	-6.81130	1.07261	0.99986
C	-4.82936	1.89055	0.73585	H	-6.35708	2.31298	2.16132
C	-4.47703	3.17723	0.62156	H	-5.69637	0.68184	2.30450
C	-5.98404	1.46241	1.59701				

* between the proton of the carboxylic acid function and the pyrrolidine nitrogen

S3.5.12 Amine derived from diethyl ketomalonate and catalyst 1

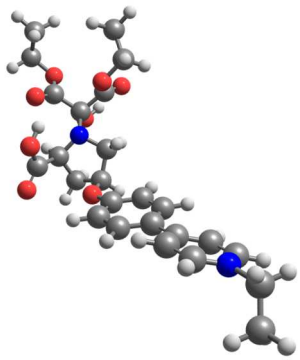

Figure S3.23 – ball-and-stick model of the optimized geometry of the amine derived from diethyl ketomalonate and catalyst **1**.

C	2.70900	-2.14142	0.26851	O	4.51121	-0.42586	-1.56566
C	1.92577	-2.70105	1.45624	O	2.98848	2.10150	-0.12815
C	0.79243	-1.69903	1.59603	C	2.78370	3.54498	-0.09047
C	1.46801	-0.36262	1.30190	C	4.05352	4.27720	-0.46195
N	2.59210	-0.66808	0.39415	C	6.91257	1.75944	-1.91656
C	2.14359	-2.67849	-1.06625	O	4.39771	-0.47789	1.90055
O	1.68179	-3.78442	-1.15612	H	3.75448	-2.44608	0.30943
O	2.21303	-1.85358	-2.10829	H	2.54225	-2.66626	2.35373
O	-0.16107	-2.03265	0.56476	H	1.57176	-3.71336	1.28505
C	-1.35439	-1.45472	0.48672	H	0.29873	-1.72945	2.56692
C	-1.86921	-0.52730	1.40494	H	1.82642	0.05593	2.24660
C	-3.14313	-0.02782	1.22743	H	0.78360	0.35108	0.84181
C	-3.94059	-0.40280	0.13311	H	2.77502	-1.08480	-1.88009
C	-3.39333	-1.32340	-0.78671	H	-1.28142	-0.19561	2.24697
C	-2.13731	-1.84423	-0.61426	H	-3.50513	0.69990	1.94045
C	-5.27366	0.13083	-0.04598	H	-3.97703	-1.66657	-1.62925
C	-6.00571	0.71226	1.01292	H	-1.72108	-2.56501	-1.30440
C	-7.26651	1.20162	0.81558	H	-5.59711	0.75812	2.01011
N	-7.86058	1.15472	-0.39805	H	-7.84831	1.63784	1.61414
C	-7.19546	0.60584	-1.43955	H	-7.71421	0.60148	-2.38691
C	-5.93324	0.10218	-1.29518	H	-5.44393	-0.29211	-2.17169
C	-9.25367	1.62724	-0.56915	H	-9.33024	2.03954	-1.57400
C	-10.25973	0.50904	-0.34697	H	-9.40274	2.44434	0.13452
C	3.80296	0.02537	0.72844	H	-10.11129	-0.30292	-1.05955
C	4.80085	-0.04431	-0.45811	H	-11.26904	0.89792	-0.48062
O	5.98286	0.41936	-0.09358	H	-10.18178	0.10323	0.66212
C	7.02487	0.48425	-1.11144	H	6.94475	-0.40045	-1.73988
C	3.52678	1.53843	0.93910	H	7.94825	0.44387	-0.53892
O	3.81766	2.09132	1.96954	H	2.43554	3.81664	0.90454

H	1.99127	3.71232	-0.81618	H	5.98294	1.78228	-2.48438
H	4.83757	4.09663	0.27255	H	7.74304	1.81518	-2.62219
H	3.85708	5.35020	-0.49218	H	6.95842	2.63360	-1.26649
H	4.40588	3.96604	-1.44531	H	4.64378	0.27863	2.45622

S3.6 Syntheses

Commercially purchased chemicals were used as received without further purification. Reactions under inert gas atmosphere were performed using dry argon, standard Schlenk techniques and oven-dried glassware. For thin-layer chromatography silica gel plates from Merck were used and spots were visualized under UV light (254/366 nm). Column chromatography was performed on silica gel from Merck (pore size 60 Å, 40-63 µm). ^{1}H NMR spectra were recorded at 400 MHz and 500 MHz and ^{13}C NMR spectra were recorded at 100 MHz and 125 MHz. Chemical shifts are reported relative to the solvent residual peak (^{1}H) or the solvent peak (^{13}C) respectively.[241] The abbreviation "s" indicades singlet, "d" doublet, "pd" pseudo-doublet, "t" triplet, "q" quartet and "m" multiplet.

S3.6.1 Catalyst 1

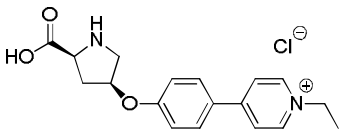

Figure S3.24 – Structural formula of compound **1**.

Preparation of the charge-tagged catalyst **1** has been described previously (cf. Subchapter 2.5.1).[1]

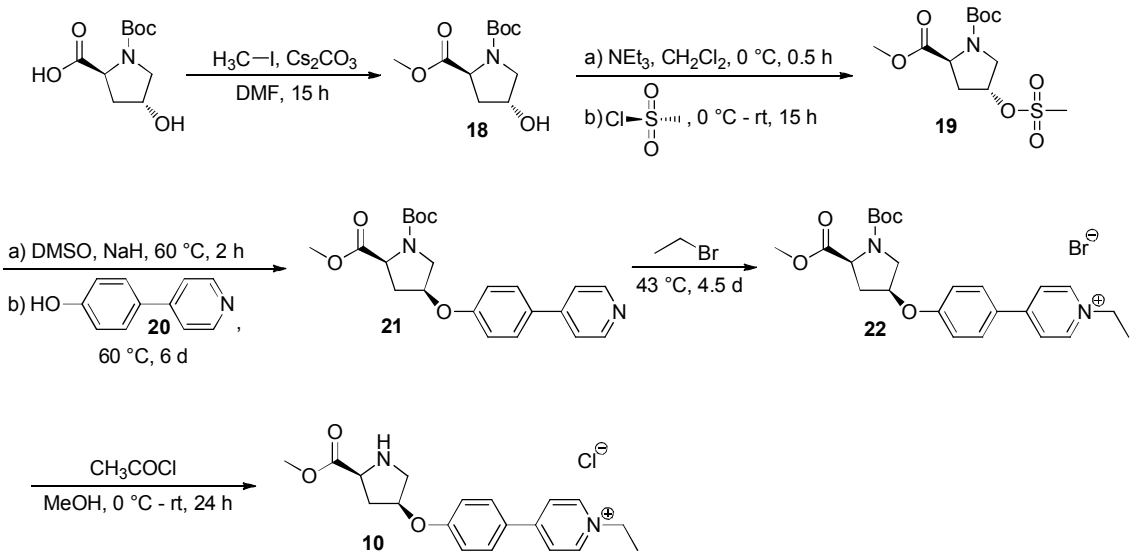

Figure S3.25 – Synthetic route to catalyst **10**.

S3.6.2 (4*R*)-*N*-(*tert*-Butoxycarbonyl)-4-hydroxy-L-proline methyl ester (18)

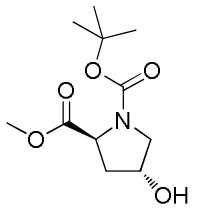

Figure S3.26 – Structural formula of compound **18**.

Compound **18** was prepared according to a literature protocol.[242]

Yield = 95 %; ^{1}H-NMR (500 MHz, DMSO-d_6) δ [ppm]: 5.09 (d, 1H, J = 3.7 Hz), 4.25 (s, 1H), 4.23-4.18 (m, 1H), 3.65/3.62 (s, 3H), 3.43-3.35 (m, 1H), 3.29-3.23 (m, 1H), 2.15-2.07 (m, 1H), 1.93-1.84 (m, 1H), 1.39/1.32 (s, 9H); ^{13}C-{^{1}H}-NMR (125 MHz, DMSO-d_6) δ [ppm]: 173.3/172.9, 153.7/153.0, 79.0/78.9, 68.5/67.8, 57.7/57.4, 54.7/54.4, 51.8/51.7, 38.7, 28.1/27.8. HR-ESI-MS(+) [*m/z*]: 268.1160 $[M+Na]^+$, calc. for $C_{11}H_{19}NO_5Na^+$: 268.1155.

S3.6.3 (4*R*)-*N*-*tert*-Butoxycarbonyl-4-methylsulfonyloxy-L-proline methyl ester (19)

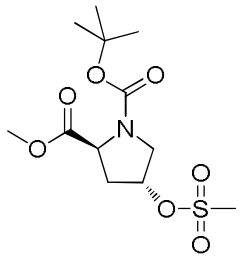

Figure S3.27 – Structural formula of compound **19**.

Compound **19** was prepared according to a literature protocol (cf. Subchapter 2.5.1).[1] The spectroscopic data are in agreement with those previously published.[243]

S.3.6.4 4-(Pyridine-4'-yl)phenol (20)

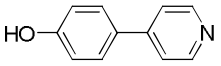

Figure S3.28 – Structural formula of compound **20**.

Compound **20** was prepared according to a literature protocol and the spectroscopic data are in agreement with those published.[113]

S.3.6.5 (2*S*,4*S*)-1-*tert*-Butyl-2-methyl 4-(4-(pyridin-4´-yl)phenoxy)pyrrolidine-1,2-dicarboxylate (21)

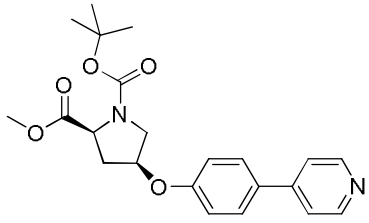

Figure S3.29 – Structural formula of compound **21**.

Compound **21** was prepared according to a reported procedure which was slightly modified (cf. Subchapter 2.5.1):[1]

4-(Pyridine-4'-yl)phenol (**20**, 0.34 g, 2.00 mmol) and NaH (60% dispersion in mineral oil, 0.12 g, 3.00 mmol) were dissolved in dry DMSO (20 mL) under inert gas

atmosphere. The suspension was heated to 60 °C and stirred for 2.0 h. (4*R*)-*N*-*tert*-Butoxycarbonyl-4-methylsulfonyloxy-L-proline methyl ester (**19**, 0.65 g, 2.00 mmol) was added and the mixture was stirred for 6 d at 60 °C. The reaction was quenched by the addition of H_2O (30 mL) and the aqueous phase was extracted with CH_2Cl_2 (3 × 25 mL) and with Et_2O (2 × 25 mL). The combined organic extracts were dried with $MgSO_4$ and the solvents were removed in vacuo. Remaining DMSO was removed by vacuum distillation. The crude product was purified by column chromatography on silica gel using cyclohexane/ethyl acetate (1:2) with 5% triethylamine as eluent (R_f = 0.50). Compound **21** was obtained as yellowish solid.

Yield = 51 %; ^{1}H-NMR (500 MHz, Methanol-d_4) δ [ppm]: 8.55-8.49 (m, 2H), 7.72 (pd, 2H, *J* = 8.7 Hz), 7.69-7.64 (m, 2H), 7.02-6.97 (m, 2H), 5.14-5.06 (m, 1H), 4.54-4.45 (m, 1H), 3.83-3.75 (m, 1H), 3.73/3,71 (s, 3H) 3.69-3.60 (m, 1H), 2.65-2.50 (m, 1H), 2.48-2.40 (m, 1H), 1.51-1.40 (m, 9H); ^{13}C-{^{1}H}-NMR (125 MHz, Methanol-d_4) δ [ppm]: 174.1/173.9, 159.3, 156.1/155.9, 150.4, 150.1, 131.6, 129.5, 122.5, 117.4/117.3, 81.7, 77.0/76.1, 59.3/58.9, 53.4, 52.9/52.8/52.7, 36.9/36.2, 28.7/28.5; HR-ESI-MS(+) [*m/z*]: 399.1900 $[M+H]^+$, calc. for $C_{22}H_{26}N_2O_5H^+$: 399.1914.

S.3.6.6 4-(4-(((3*S*,5*S*)-1-(*tert*-Butoxycarbonyl)-5-(methoxycarbonyl)pyrrolidin-3-yl)oxy)phenyl)-1-ethylpyridinium bromide (22)

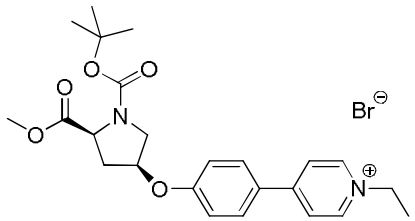

Figure S3.30 – Structural formula of compound **22**.

Compound **22** was prepared according to a reported procedure (cf. Subchapter 2.5.1).[1] (2*S*,4*S*)-1-*tert*-Butyl-2-methyl 4-(4-(pyridin-4′-yl)phenoxy)pyrrolidine-1,2-dicarboxylate (**21**, 0.20 g, 0.50 mmol) was dissolved in bromoethane (99 %, 17 mL, 225.50 mmol) and stirred for 4.5 d at 43 °C. Excessive bromoethane was removed in vacuo. Compound **22** was obtained as brownish-yellow, highly viscous oil.

Yield = quant.; ^{1}H-NMR (400 MHz, Methanol-d_4) δ [ppm]: 8.91 (pd, 2H, *J* = 6.8 Hz), 8.37-8.32 (m, 2H), 8.05-7.99 (m, 2H), 7.11 (pd, 2H, *J* = 8.9 Hz), 5.23-5.17 (m, 1H), 4.64 (q, 2H, *J* = 7.3 Hz), 4.55-4.49 (m, 1H), 3.88-3.77 (m, 1H), 3.73/3.71 (s, 3H), 3.69-

3.61 (m, 1H), 2.72-2.56 (m, 1H), 2.48-2.41 (m, 1H), 1.67 (t, 3H, *J* = 7.3 Hz), 1.50-1.40 (m, 9H); ^{13}C-{^{1}H}-NMR (100 MHz, Methanol-*d*$_4$) δ [ppm]: 174.0/173.8, 161.8, 156.9, 156.0/155.8, 145.2, 131.2, 127.7, 124.9, 117.8, 81.8, 77.4, 76.5, 59.2/58.9, 57.2, 53.4/52.8/52.8, 36.9, 36.2, 28.7/28.5, 16.7; HR-ESI-MS(+) [*m/z*]: 427.2198 $[M]^+$, calc. for $C_{24}H_{31}N_2O_5^+$: 427.2227.

S3.6.7 1-Ethyl-4-(4-(((3*S*,5*S*)-5-(methoxycarbonyl)pyrrolidin-3-yl)oxy)phenyl)-pyridinium chloride (10)

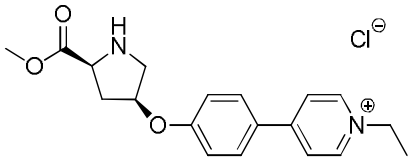

Figure S3.31 – Structural formula of compound **10**.

Compound **10** was prepared according to a literature protocol.[244]

4-(4-(((3*S*,5*S*)-1-(*tert*-Butoxycarbonyl)-5-(methoxycarbonyl)pyrrolidin-3-yl)oxy)phenyl)-1-ethylpyridinium bromide (**22**, 0.13 g, 0.26 mmol) was dissolved in MeOH (18 mL) and cooled to 0 °C with an ice bath. After dropwise addition of acetyl chloride (98 %, 1.0 mL, 13.73 mmol) the solution was stirred for 24 h without further cooling. The solvent was removed *in vacuo*. Compound **10** was obtained as brown, highly viscous oil.

Yield = quant.; ^{1}H-NMR (500 MHz, Methanol-*d*$_4$) δ [ppm]: 8.90 (pd, 2H, *J* = 6.3 Hz), 8.35 (pd, 2H, *J* = 6.3 Hz), 8.05 (pd, 2H, *J* = 8.4 Hz), 7.20-7.15 (m, 2H), 5.42-5.36 (m, 1H), 4.78-4.71 (m, 1H), 4.63 (q, 2H, *J* = 7.3 Hz), 3.83 (s, 3H), 3.76-3.70 (m, 2H), 2.82-2.73 (m, 1H), 2.72-2.65 (m, 1H), 1.67 (t, 3H, *J* = 7.3 Hz); ^{13}C-{^{1}H}-NMR (125 MHz, Methanol-*d*$_4$) δ [ppm]: 170.1, 160.6, 156.5, 145.3, 131.3, 128.3, 125.1, 117.9, 76.6, 59.8, 57.3, 54.3, 52.5, 35.6, 16.8; ESI-MS(+) [*m/z*]: 327.1711 $[M]^+$, calc. for $C_{19}H_{22}N_2O_3^+$: 327.1703.

S4 Supporting information to Chapter 4

Investigations of the copper-catalyzed oxidative cross-coupling of Tetrahydroisoquinolines with diethylzinc by a combination of mass spectrometric and electrochemical methods

J. A. Willms, H. Gleich, M. Schrempp, D. Menche, M. Engeser

Contents

S4.1 MS analysis of reaction mixtures

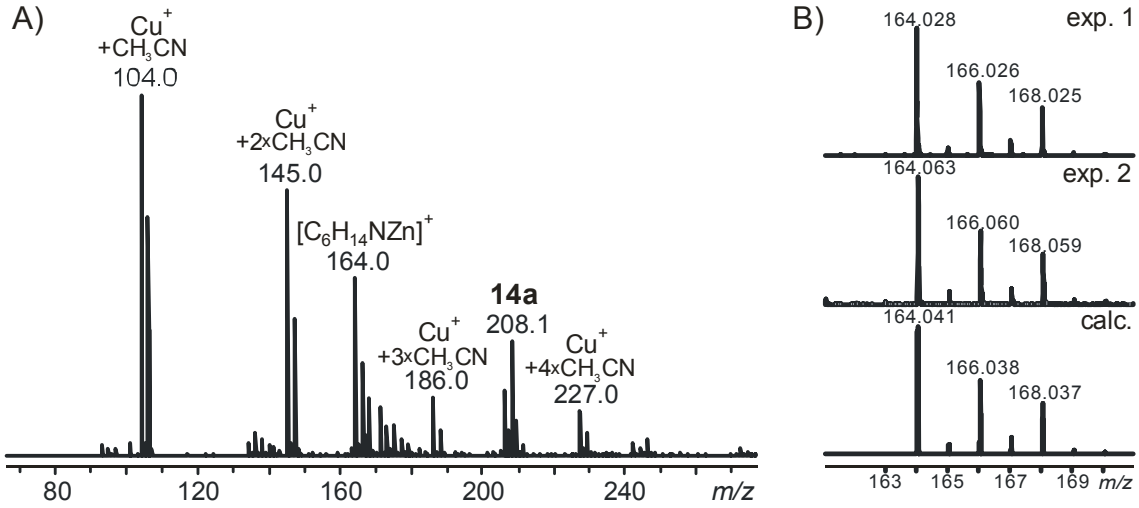

Figure S4.1 – A) ESI(+) mass spectrum of *N*-Ph-THIQ **11a** [134.0 µM], $CuCl_2$ [66.8 µM] and $ZnEt_2$ [50.8 mM] in acetonitrile after a reaction time of 0.5 h – diluted 1:1 with acetonitrile; B) Extrema of experimental *m/z* values for the detected zinc species with *m/z* 164 (top, center) and calculated isotope pattern for $[C_6H_{14}NZn]^+$ (bottom).

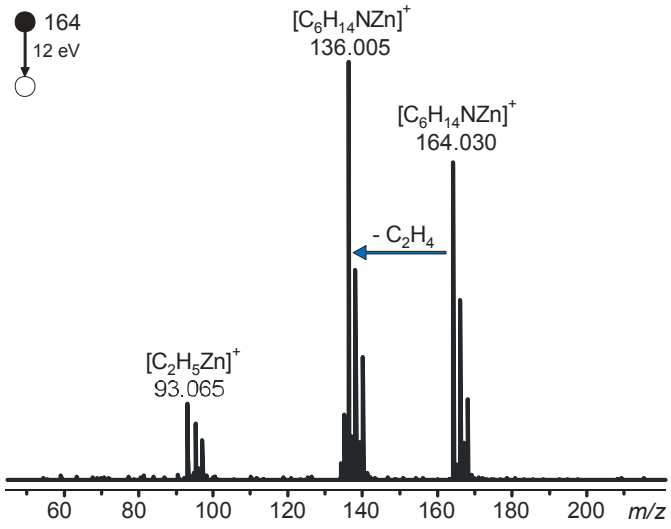

Figure S4.2 – ESI(+) collision induced dissociation (CID) spectrum of the mass-selected ion at *m/z* 164. Formally the detected species can be described as $[ZnEt_2 + CH_3CN + H]^+$. Since $ZnEt_2$ is a highly reactive compound, we refrain from a distinct structural assignment.

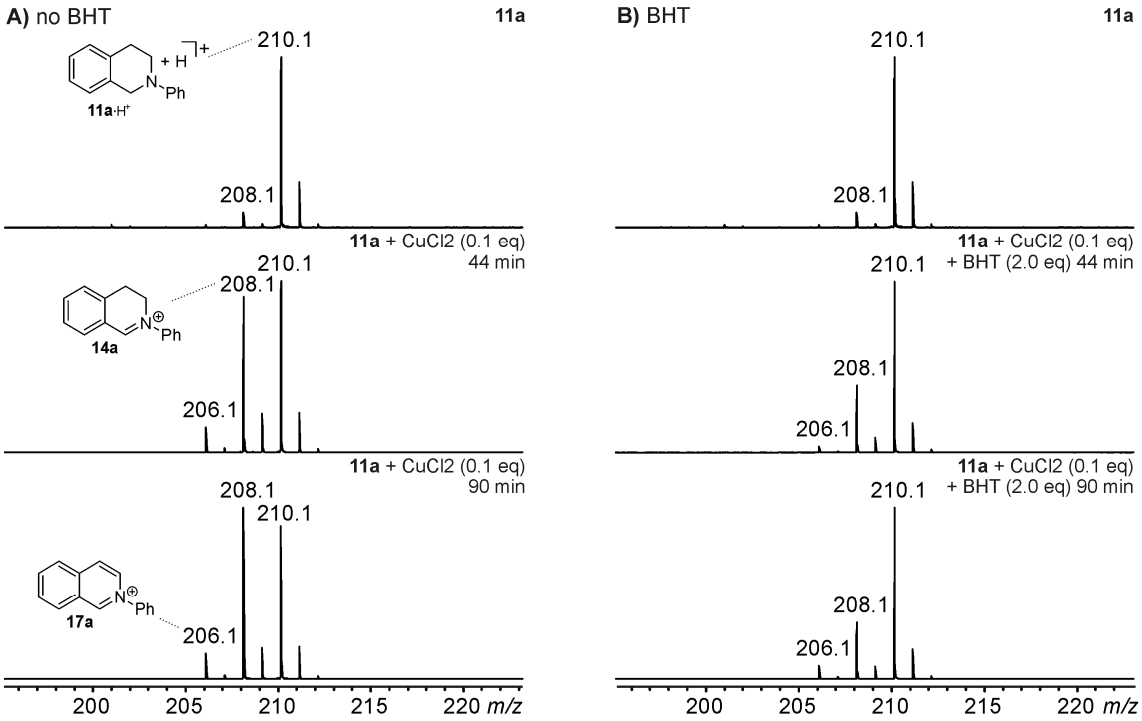

Figure S4.3 – ESI(+) mass spectra of samples from acetonitrile solutions of A) *N*-Ph-THIQ **11a** [0.64 mM] and $CuCl_2$ [64.0 µM] and B) *N*-Ph-THIQ **11a** [0.64 mM], $CuCl_2$ [64.0 µM] and BHT [1.28 mM] at different reaction times – samples diluted 1:99 with CH_2Cl_2/MeOH (1:1).

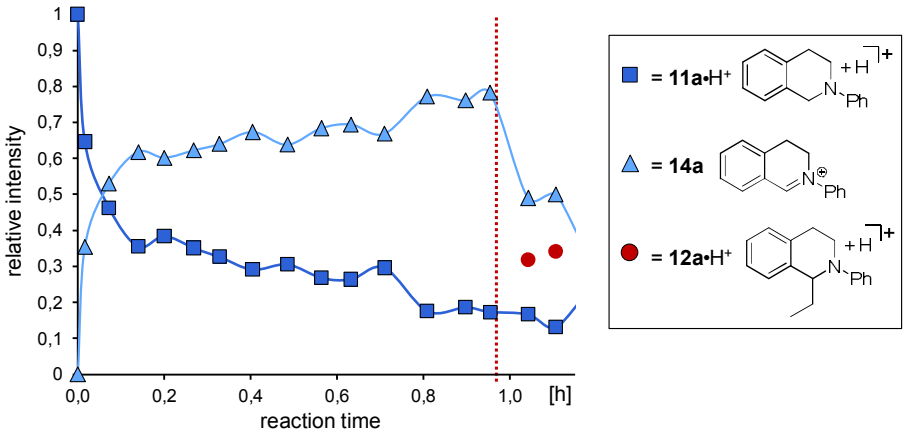

Figure S4.4 – Plot of normalized relative intensities in ESI(+) spectra of acetonitrile solutions of **11a** [50.0 mM] and $CuCl_2$ [5.0 mM] at different reaction times; $ZnEt_2$ [0.2 M] was added after 1 h (red dotted line) – samples diluted 1:400 with CH_2Cl_2/MeOH (1:1).

---

* Note that:

- The ESI conditions are a bit too harsh to completely suppress unintended oxidation of **11a** to **14a** during the ionization.
- No O_2 was applied to reoxidize the copper(I) to copper(II).
- Similar to the results of *Klussmann* and coworkers[225] for another CDC reaction, the inhibiting effect of BHT is too slow to fully suppress the reaction.

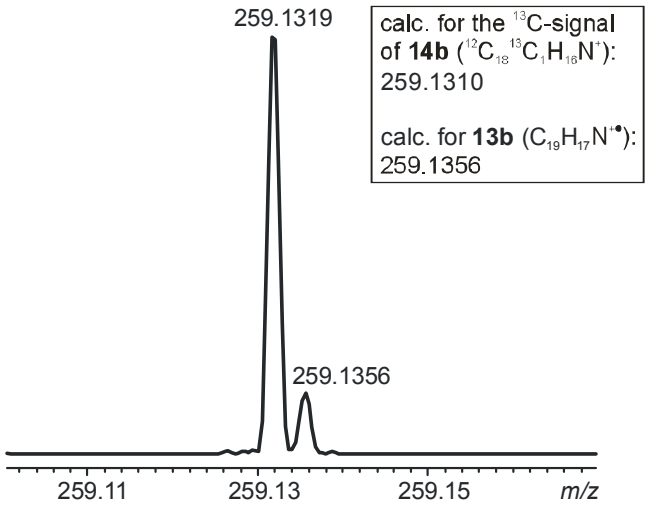

Figure S4.5 – A zoom into the ESI(+) mass spectrum of *N*-naphthyl-THIQ **11b** [0.313 mM] and $CuCl_2$ [0.125 mM] in acetonitrile 2.5 minutes after mixing – sample diluted 1:10 with CH_2Cl_2/MeOH (1:1) and analyzed with an Orbitrap XL mass spectrometer with resolution set to R = 100000.

S4.2 Details of EC-MS experiments

The voltage-dependent ion-intensity curves were obtained with a commercial electrochemical flow cell (Antec Scientific ROXY potentiostat and thin-layer ReactorCell) arranged between a manually controlled syringe pump (Cole Parmer) and the ESI source of a Q/TOF mass spectrometer (Figure S4.6). Analyte solutions were continuously pumped from a 250 µL glass syringe (Hamilton) in and out of the EC cell into the ESI ion source through PEEK tubing (1/16" OD x 0.13 mm ID) with a flowrate of 300 µL/h. We used a magic diamond (MD) working electrode (Ø: 8 mm), a 50 µm spacer, and a HyREF reference electrode (E_{HyREF} [mV] = $E_{Ag/AgCl}$ [mV] – 328 [mV] + 29.9 • pH-value). The resulting cell volume was 0.7 µL. At the beginning of every experiment analyte solutions were pumped through the whole setup while the EC cell remained switched off until a stable MS signal was adjusted. The different EC cell events (see Table S4.1–Table S4.3) were programmed beforehand using the software Dialogue (Antec Scientific) on a computer which was connected to the EC cell for controlling. We programmed a delayed switch-on time for the flow cell within the voltage climax EC programs with the aim to record a chromatogram of mass spectra unaffected by an applied voltage before recording the actual voltage-dependent ion-intensity curve. This should check and monitor preferably stable ion abundances. The

climax-like voltage variation of the EC cell curves had the purpose to proof reproducibility. Due to the continuous analyte flow the initial MS spectra should approximately be recovered at the end of the experiment when the EC cell is switched off again. Moreover, we recalibrated the voltage trace of every measurement to erase the time lag between oxidative penetration and MS analysis. This time lag was determined by manually switching on the EC cell at 2-3.5 Volt and measurement of the time between this switch-on and the detection of oxidized species (usually 0.2–0.4 min.). Since the used programs (for MS and EC cell) were operated separately it was also very important to note the time lag between MS acquisition and the start of the EC cell event.

S4.2.1. Experimental setup

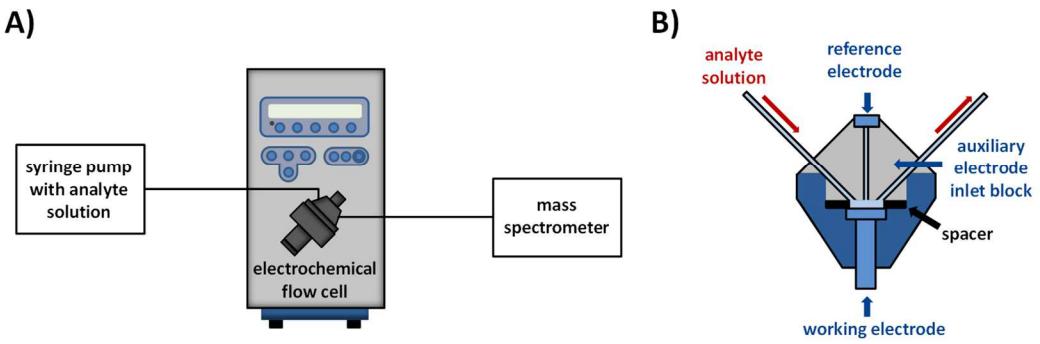

Figure S4.6 – A) Schematic experimental assembly of the EC-MS setup – All parts of the EC cell were purchased from Antec Scientific; B) Depiction of the EC cell parts.

S4.2.2. CDC reaction between $ZnEt_2$ and electrochemically formed iminium 14a

For the electrochemically induced coupling reaction, a solution of *N*-Ph-THIQ **11a** [9.5 µM] in dry acetonitrile was pumped continuously through the EC flow cell similar to the setup of Figure S4.6, where it was perpetually oxidized with applying the EC program from Table S4.3. However, the oxidized solution was not pumped into the ESI source of a mass spectrometer, but into a septum sealed Schlenk flask with an acetonitrile solution of $ZnEt_2$ [0.1 M]. This solution was prepared under argon with dry acetonitrile (0.54 mL) and a solution of $ZnEt_2$ in *n*-hexane [1 M] (60 µL, 60 µmol). The

solution of *N*-Ph-THIQ **11a** was oxidized and led into the $ZnEt_2$ solution with a flow rate of 500 µL/h for 105 min. Afterwards a 100 µL sample of the reaction solution was drawn, diluted 1:10 with CH_2Cl_2/MeOH (1:1) and analyzed by ESI-MS. The resulting MS spectrum is shown in Figure 4.5 and Figure S4.7.

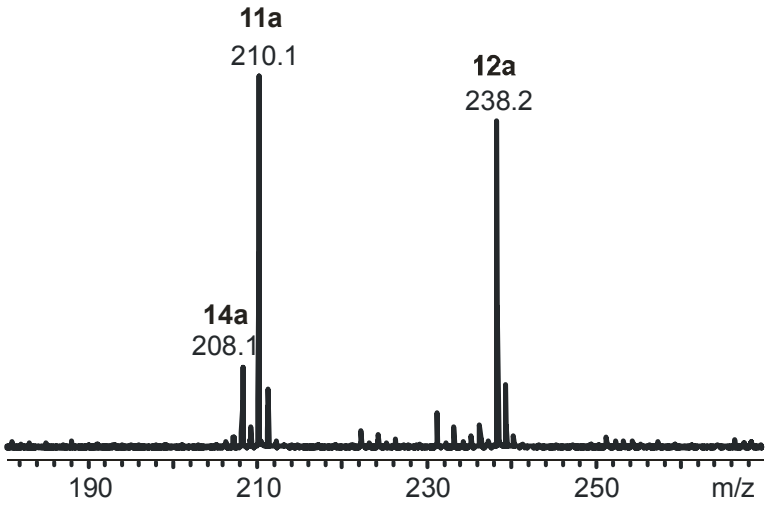

Figure S4.7 – ESI(+) mass spectrum of reaction solution of the electrochemically induced CDC reaction between *N*-Ph-THIQ **11a** and $ZnEt_2$ in acetonitrile after a reaction time of 105 min – diluted 1:10 with CH_2Cl_2/MeOH (1:1).

S4.2.3. EC cell progamms

Table S4.1 – EC cell program for the voltage/ion-intensity curve experiments with a voltage climax of 2.0 V.

time [min]	command	applied voltage [V]
0.00	start event	-
2.95	set DC	0.1
3.00	Cell on	-
3.20	set DC	0.2
3.40	set DC	0.3
3.60	set DC	0.4
3.80	set DC	0.5
4.00	set DC	0.6
4.20	set DC	0.7
4.40	set DC	0.8
4.60	set DC	0.9
4.80	set DC	1.0
5.00	set DC	1.1
5.20	set DC	1.2
5.40	set DC	1.3
5.60	set DC	1.4
5.80	set DC	1.5
6.00	set DC	1.6
6.20	set DC	1.7
6.40	set DC	1.8
6.60	set DC	1.9
6.80	set DC	2.0
7.00	set DC	1.9
7.20	set DC	1.8
7.40	set DC	1.7
7.60	set DC	1.6
7.80	set DC	1.5
8.00	set DC	1.4
8.20	set DC	1.3
8.40	set DC	1.2
8.60	set DC	1.1
8.80	set DC	1.0
9.00	set DC	0.9
9.20	set DC	0.8
9.40	set DC	0.7
9.60	set DC	0.6
9.80	set DC	0.5
10.00	set DC	0.4
10.20	set DC	0.3
10.40	set DC	0.2
10.60	set DC	0.1
10.80	set DC	0.0
11.00	Cell off	-
15.00	end event	-

Table S4.2 – EC cell program for the voltage/ion-intensity curve experiments with a voltage climax of 3.5 V.

time [min]	command	applied voltage [V]
0.00	start event	-
4.95	set DC	0.1
5.00	Cell on	-
5.20	set DC	0.2
5.40	set DC	0.3
5.60	set DC	0.4
5.80	set DC	0.5
6.00	set DC	0.6
6.20	set DC	0.7
6.40	set DC	0.8
6.60	set DC	0.9
6.80	set DC	1.0
7.00	set DC	1.1
7.20	set DC	1.2
7.40	set DC	1.3
7.60	set DC	1.4
7.80	set DC	1.5
8.00	set DC	1.6
8.20	set DC	1.7
8.40	set DC	1.8
8.60	set DC	1.9
8.80	set DC	2.0
9.00	set DC	2.1
9.20	set DC	2.2
9.40	set DC	2.3
9.60	set DC	2.4
9.80	set DC	2.5
10.00	set DC	2.6
10.20	set DC	2.7
10.40	set DC	2.8
10.60	set DC	2.9
10.80	set DC	3.0
11.00	set DC	3.1
11.20	set DC	3.2
11.40	set DC	3.3
11.60	set DC	3.4
11.80	set DC	3.5

time [min]	command	applied voltage [V]
12.00	set DC	3.4
12.20	set DC	3.3
12.40	set DC	3.2
12.60	set DC	3.1
12.80	set DC	3.0
13.00	set DC	2.9
13.20	set DC	2.8
13.40	set DC	2.7
13.60	set DC	2.6
13.80	set DC	2.5
14.00	set DC	2.4
14.20	set DC	2.3
14.40	set DC	2.2
14.60	set DC	2.1
14.80	set DC	2.0
15.00	set DC	1.9
15.20	set DC	1.8
15.40	set DC	1.7
15.60	set DC	1.6
15.80	set DC	1.5
16.00	set DC	1.4
16.20	set DC	1.3
16.40	set DC	1.2
16.60	set DC	1.1
16.80	set DC	1.0
17.00	set DC	0.9
17.20	set DC	0.8
17.40	set DC	0.7
17.60	set DC	0.6
17.80	set DC	0.5
18.00	set DC	0.4
18.20	set DC	0.3
18.40	set DC	0.2
18.60	set DC	0.1
18.80	set DC	0.0
20.10	Cell off	-
25.00	end event	

Table S4.3 – EC cell program for the electrochemical oxidation of *N*-Ph-THIQ **11a** for the subsequent reaction with $ZnEt_2$; The program was repeated throughout the whole experiment.

time [min]	command	applied voltage [V]
0.00	start event	-
0.00	Cell on	-
0.00	set DC	4.0
0.10	set DC	4.1
0.20	set DC	4.2
0.30	set DC	4.3
0.40	set DC	4.4
0.50	set DC	4.3
0.60	set DC	4.2
0.70	set DC	4.1
0.80	end event	

S4.3 Voltage/ion-intensity curves

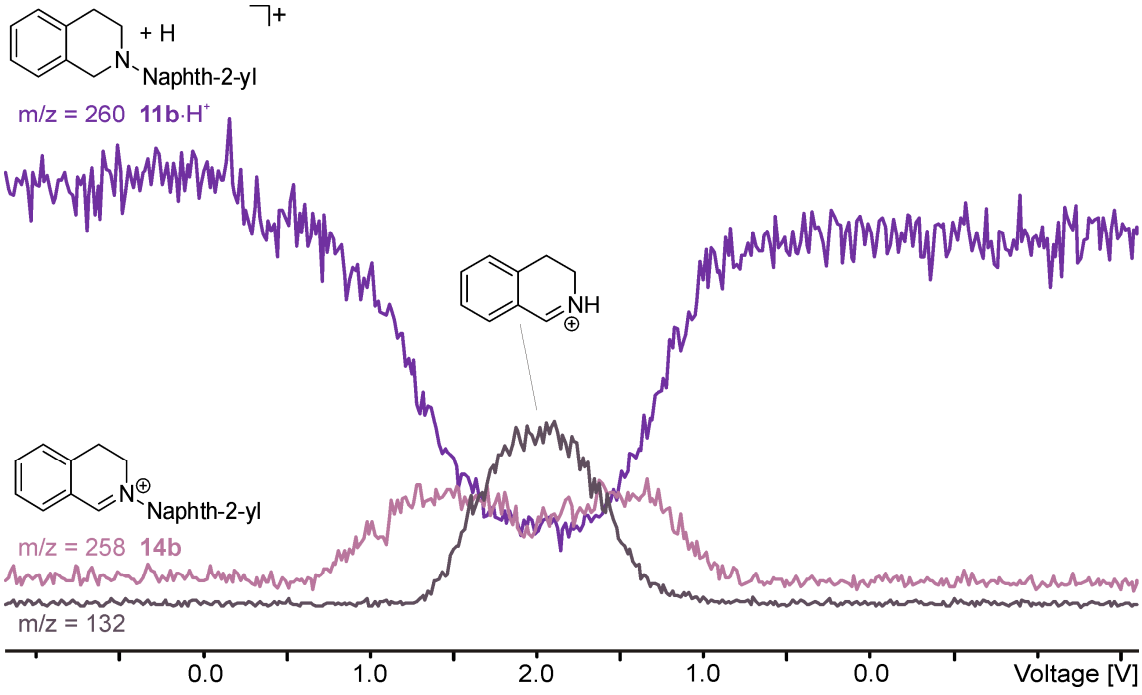

Figure S4.8 – Voltage/ion-intensity curve of **11b**; Selected-ion-chromatograms of *m/z* 260, 258 and 132 plotted against the applied voltage to a solution of *N*-naphth-2-yl-THIQ **1b** [3.2 µM] in CH_2Cl_2/MeOH (1:1) - voltage climax 2.0 V.

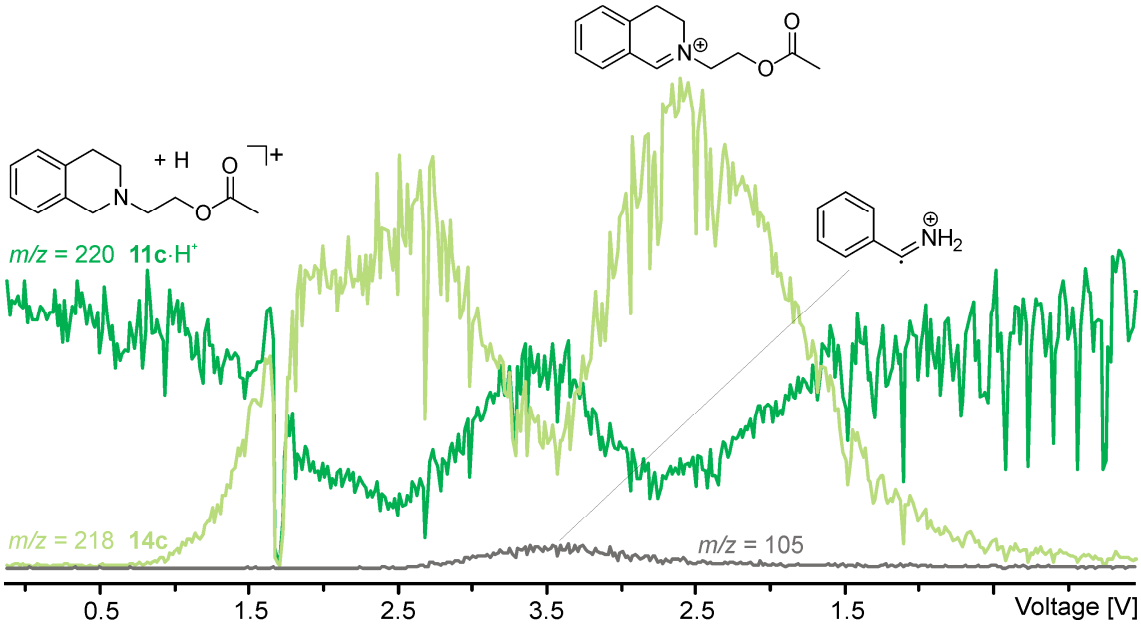

Figure S4.9 – Voltage/ion-intensity curve of **11c**; Selected-ion-chromatograms of *m/z* 220, 218 and 105 plotted against the applied voltage to a solution of *N*-(2-acetoxyethyl)-THIQ **11c** [30.5 µM] in CH_2Cl_2/MeOH (1:1) - voltage climax 3.5 V.

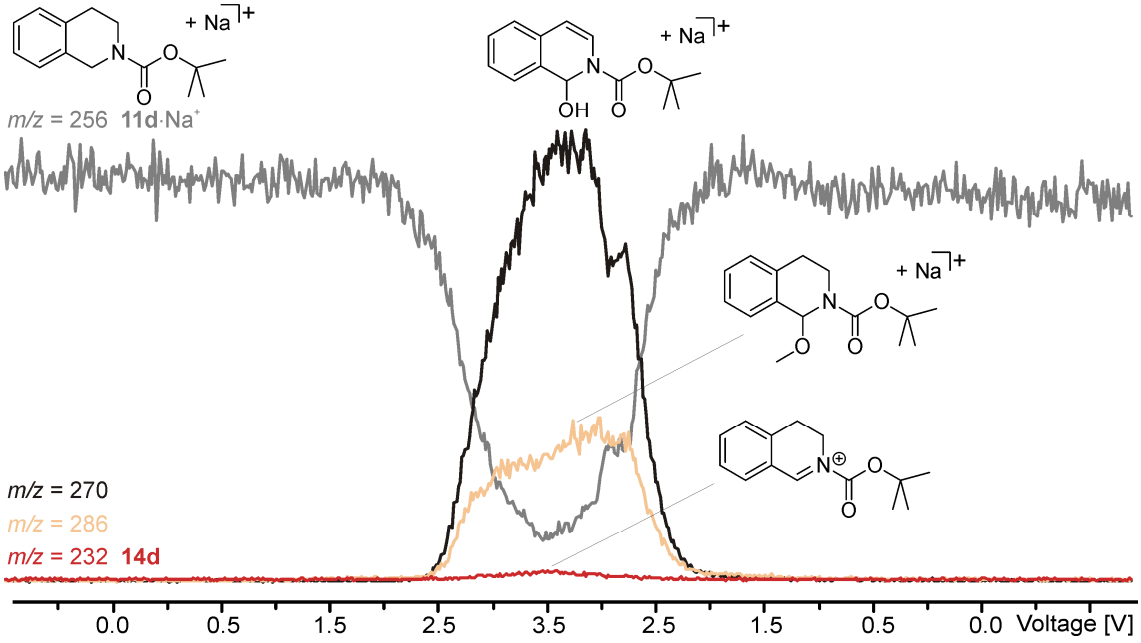

Figure S4.10 – Voltage/ion-intensity curve of **11d**; Selected-ion-chromatograms of *m/z* 286, 270, 256 and 232 plotted against the applied voltage to a solution of N-(Butoxycarbonyl)-THIQ **11d** [19.2 µM] in CH_2Cl_2/MeOH (1:1) - voltage climax 3.5 V.

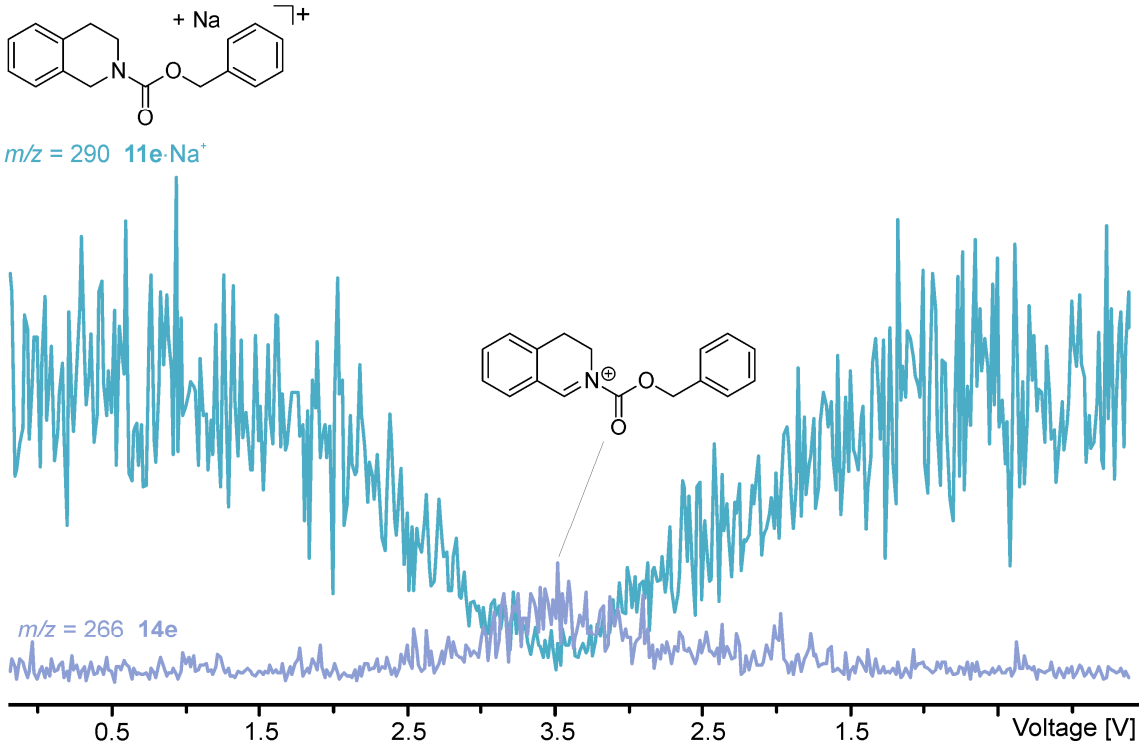

Figure S4.11 – Voltage/ion-intensity curve of **11e**; Selected-ion-chromatograms of *m/z* 290 and 266 plotted against the applied voltage to a solution of *N*-(carbobenzyloxy)-THIQ **11e** [30.5 µM] in CH_2Cl_2/MeOH (1:1) - voltage climax 3.5 V.

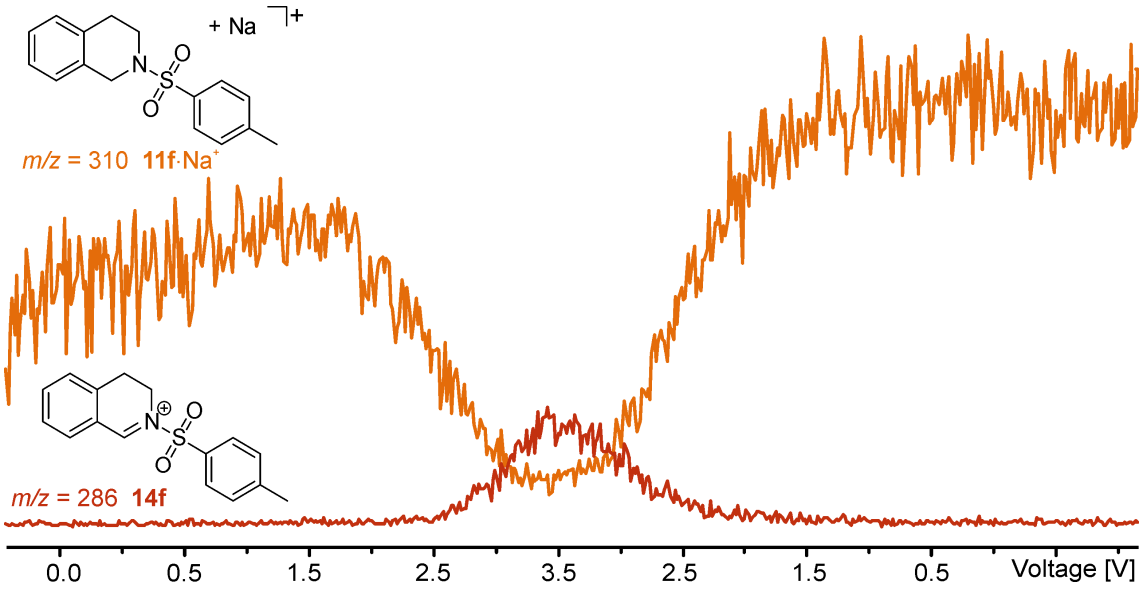

Figure S4.12 – Voltage/ion-intensity curve of **11f**; Selected-ion-chromatograms of *m/z* 310 and 286 plotted against the applied voltage to a solution of *N*-(tosyl)-THIQ **11f** [30.5 µM] in CH_2Cl_2/MeOH (1:1) - voltage climax 3.5 V.

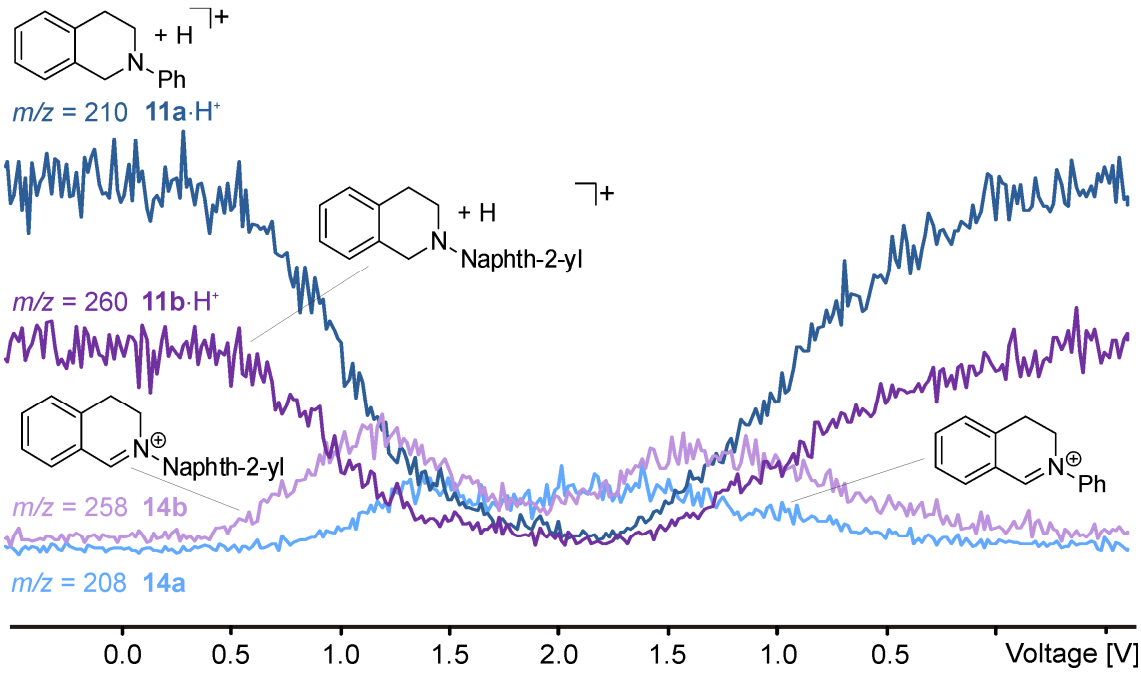

Figure S4.13 – Voltage/ion-intensity curve of **11a** and **11b** (simultaneously); Selected-ion-chromatograms of *m/z* 260, 258, 210 and 208 plotted against the applied voltage to a solution of *N*-Ph-THIQ 1b [9.5 µM] and of *N*-naphth-2-yl-THIQ **11b** [9.5 µM] in CH_2Cl_2/MeOH (1:1) - voltage climax 2.0 V.

S4.4 Cyclic voltammetry

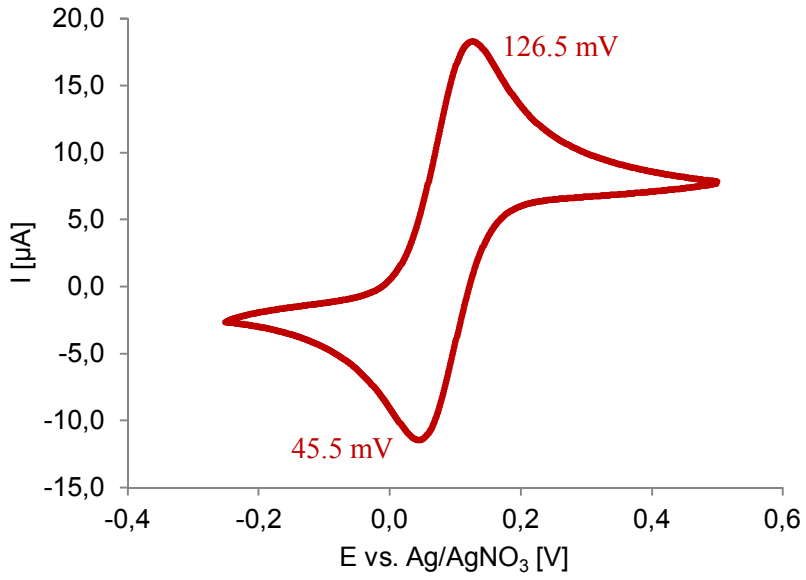

Figure S4.14 – Cyclic voltammogram of ferrocene in acetonitrile; scan rate: 50 mVs^{-1}.

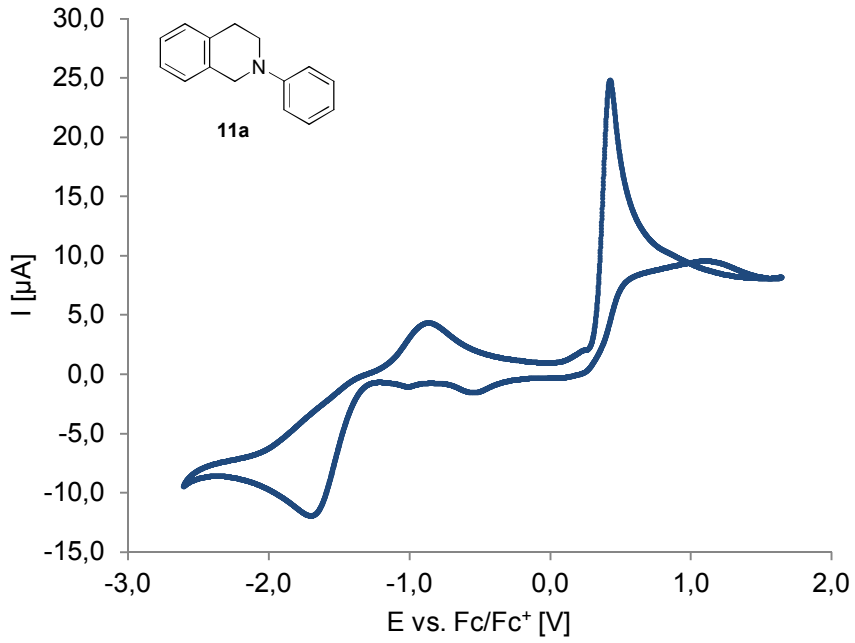

Figure S4.15 – Cyclic voltammogram of **11a** in acetonitrile [5 mM]; scan rate: 50 mVs^{-1}.

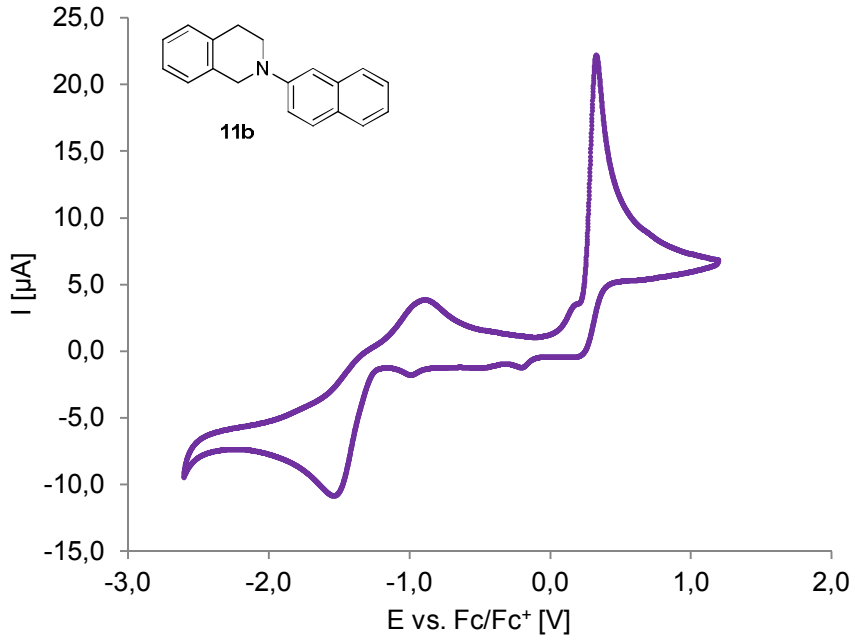

Figure S4.16 – Cyclic voltammogram of **11b** in acetonitrile [5 mM]; scan rate: 50 mVs^{-1}.

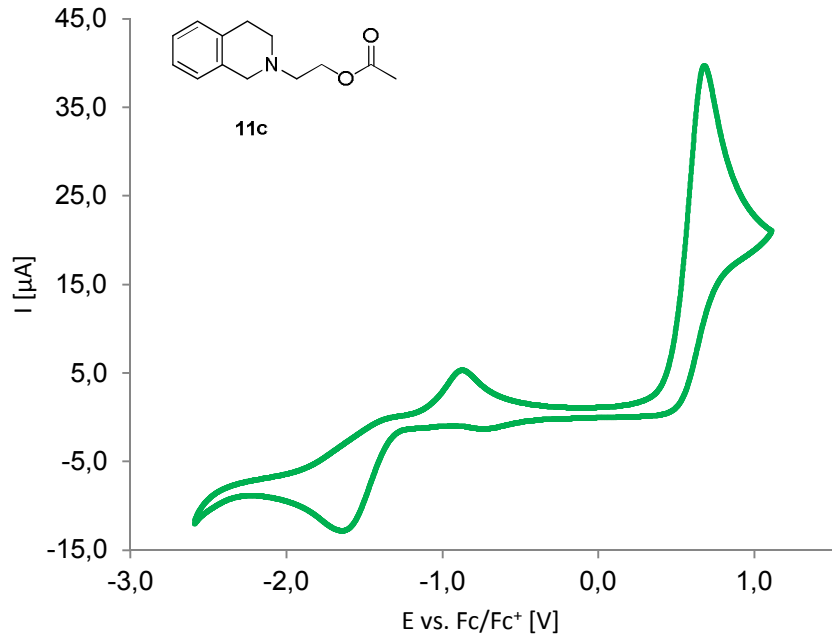

Figure S4.17 – Cyclic voltammogram of **11c** in acetonitrile [10 mM]; scan rate: 50 mVs^{-1}.

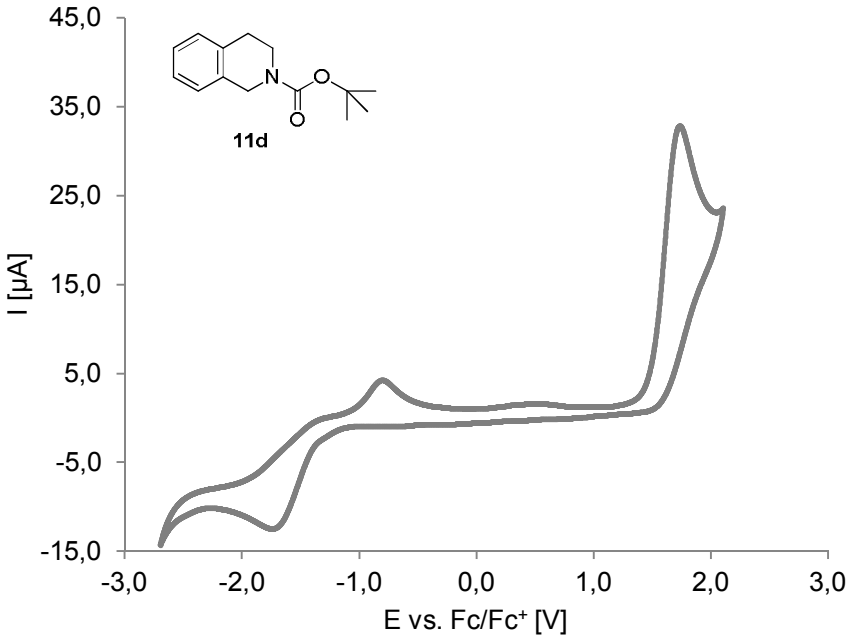

Figure S4.18 – Cyclic voltammogram of **11d** in acetonitrile [10 mM]; scan rate: 50 mVs^{-1}.

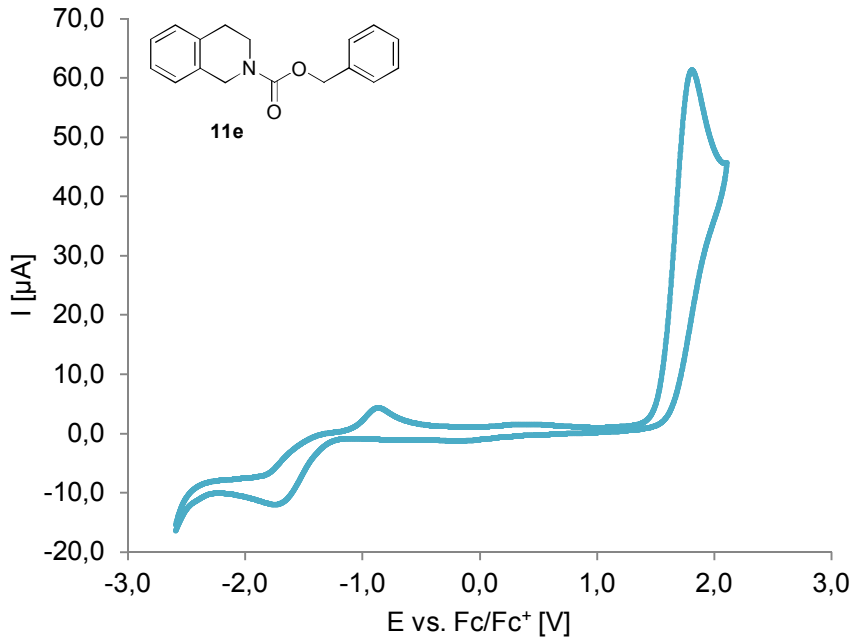

Figure S4.19 – Cyclic voltammogram of **11e** in acetonitrile [10 mM]; scan rate: 50 mVs^{-1}.

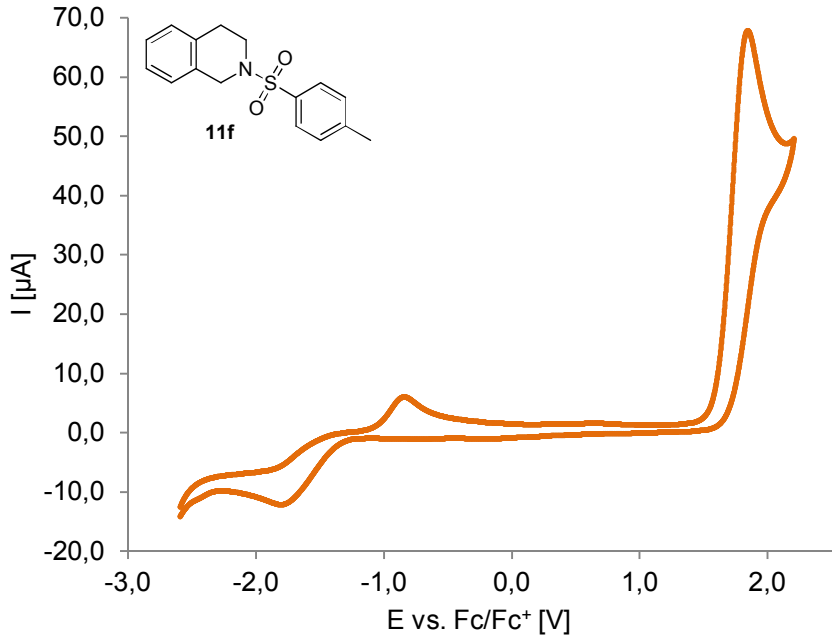

Figure S4.20 – Cyclic voltammogram of **11f** in acetonitrile [10 mM]; scan rate: 50 mVs^{-1}.

S4.5 Chemicals and syntheses

All commercially obtained chemicals were used as received without further purification. $CuCl_2$ was purchased from Alfa Aesar. Diethylzinc (1 M in *n*-hexane and 1.5 M in toluene) was purchased from Acros Organics and Sigma Aldrich. TLC was performed on silica gel plates from Macherey-Nagel and Merck and spots were visualized with a UV lamp (254/366 nm). Column chromatography was performed on silica gel from Merck (pore size 60 Å, 40-63 μm). ^{1}H NMR spectra were recorded at 400 MHz and 500 MHz and ^{13}C NMR spectra were recorded at 101 MHz and 125 MHz. Chemical shifts are reported relative to the solvent residual peak (^{1}H) or the solvent peak (^{13}C) respectively.[241]

S4.5.1. *N*-Phenyl-1,2,3,4-tetrahydroisoquinoline (11a)

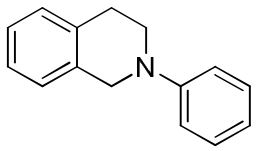

Figure S4.21 – Structural formula of compound **11a**.

11a was prepared according to a reported procedure.[245] The spectroscopic data are in agreement with those previously published.[246]

S4.5.2. *N*-naphth-2-yl-1,2,3,4-tetrahydroisoquinoline (11b)

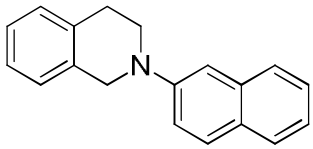

Figure S4.22 – Structural formula of compound **11b**.

11b was prepared according to a reported procedure.[245]

Yield (59 %), R_f = 0.5 (cyclohexane/ethyl acetate = 24:1). **^{1}H-NMR** (400 MHz, CD_2Cl_2) δ = 7.82-7.73 (m, 3H), 7.47-7.42 (m, 1H), 7.39 (dd, 1H, *J* = 9.0 Hz, 2.5 Hz), 7.34-7.29 (m, 1H), 7.27-7.20 (m, 5H), 4.54 (s, 2H), 3.69 (t, 2H, *J* = 5.9 Hz), 3.06 (t, 2H, *J* = 5.9 Hz) ppm. **^{13}C-NMR** (101 MHz, CD_2Cl_2) δ = 149.0, 135.5, 135.5, 135.1, 129.2, 129.1, 128.5, 127.9, 127.1, 127.0, 126.9, 126.8, 126.6, 123.4, 119.1, 109.4, 51.4, 47.5, 29.7 ppm. HR-ESI-MS(+) *m/z*: 260.1444 $[M + H]^+$, calc. for $C_{19}H_{18}N^+$: 260.1434.

S4.5.3. *N*-Acetoxyethyl-1,2,3,4-tetrahydroisoquinoline (11c)

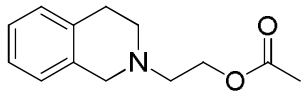

Figure S4.23 – Structural formula of compound **11c**.

1,2,3,4-Tetrahydroisoquinoline (666 mg, 5.00 mmol, 1.0 eq.) were dissolved in CH_3CN (10.0 mL). K_2CO_3 (1.35 g, 9.77 mmol, 1.9 eq.) and NaI (75.0 mg, 500 µmol, 0.1 eq.) were added and the resulting mixture was stirred for 5 min. After the addition of ethyl bromoacetate (600 µL, 5.44 mmol, 1.1 eq.) the mixture was stirred for 6 h at 60 °C. The reaction was allowed to cool down to rt before adding ethyl acetate (15.0 mL) and H_2O (10 mL). The layers were separated and the aqueous layer was extracted with ethyl acetate (2 × 10 mL). The combined organic phases were dried over anhydrous $MgSO_4$, concentrated *in vacuo* and purified by flash column chromatography to afford the **11c** as a yellowish oil.

Yield (75 %), R_f = 0.17 (cyclohexane/ethyl acetate = 3:2). **^{1}H-NMR** (500 MHz, CD_2Cl_2) δ = 2.08 (s, 3H), 2.86 – 2.86 (m, 4H), 2.91 (t, *J* = 6.0 Hz, 2H), 3.72 (s, 1H), 4.30 (t, *J* = 5.9 Hz, 2H), 7.00 – 7.14 (m, 4H) ppm. **^{13}C-NMR** (125 MHz, CD_2Cl_2) δ = 171.2, 134.4, 134.2, 126.7, 126.4, 125.8, 62.1, 56.4, 56.3, 51.2, 28.9, 21.2 ppm. HR-ESI-MS(+) *m/z*: 242.1148 $[M + Na]^+$, calc. for $C_{13}H_{17}NO_2Na^+$: 242.1151.

S4.5.4. *N*-Boc-1,2,3,4-tetrahydroisoquinoline (11d)

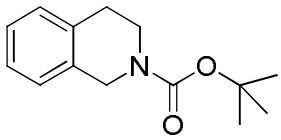

Figure S4.24 – Structural formula of compound **11d**.

11d was prepared according to a reported procedure.[247] The spectroscopic data are in agreement with those previously published.[248]

S4.5.5. *N*-Benzyloxycarbonyl-1,2,3,4-tetrahydroisoquinoline (11e)

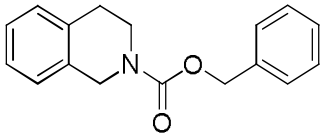

Figure S4.25 – Structural formula of compound **11e**.

11e was prepared according to a reported procedure and the spectroscopic data are in agreement with this literature.[249]

S4.5.6. *N*-Tosyl-1,2,3,4-tetrahydroisoquinoline (11f)

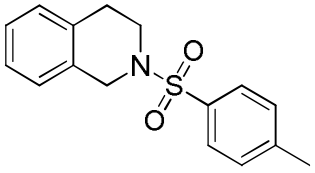

Figure S4.26 – Structural formula of compound **11f**.

11f was prepared according to a reported procedure and the spectroscopic data are in agreement with this literature.[250]